

1 **Technical note: Surface fields for global environmental modelling**

2 Margarita Choulga¹, Francesca Moschini¹, Cinzia Mazzetti¹, Stefania Grimaldi², Juliana
3 Disperati³, Hylke Beck⁴, Peter Salamon², Christel Prudhomme¹

4 ¹European Centre for Medium-Range Weather Forecasts (ECMWF), Reading, RG2 9AX, United Kingdom

5 ²Joint Research Centre (JRC), European Commission, Ispra, 21027, Italy

6 ³Fincons Group, Vimercate, 20871, Italy

7 ⁴King Abdullah University of Science and Technology (KAUST), Thuwal, Saudi Arabia

8 *Correspondence to:* Margarita Choulga (margarita.choulga@ecmwf.int) and Christel Prudhomme
9 (christel.prudhomme@ecmwf.int)

10 **Abstract.** Climate change has resulted in more frequent occurrences of extreme events, such as flooding and
11 heavy snowfall, which can have a significant impact on densely populated or industrialised areas. Numerical
12 models are used to simulate and predict these extreme events, enabling informed decision-making and planning
13 to minimise human casualties and protect costly infrastructure. LISFLOOD is an integrated hydrological model
14 underpinning the European and Global Flood Awareness Systems (EFAS and GloFAS, respectively) developed
15 by the Copernicus Emergency Management Service (CEMS). The CEMS_SurfaceFields_2022 dataset is a new
16 set of high-resolution surface fields at 1 and 3 arc min (approximately 2 and 6 km at the equator respectively)
17 covering Europe and the global land surface (excluding Antarctica) respectively, based on a wide variety of high-
18 resolution and up-to-date data sources. The dataset encompasses (i) catchment morphology and river network, (ii)
19 land use, (iii) vegetation cover type and properties, (iv) soil properties, (v) lake information, and (vi) water
20 demand. This manuscript details the complete workflow to generate CEMS_SurfaceFields_2022 fields, including
21 data sources and methodology. Whilst created together with upgrades to the open source LISFLOOD code, the
22 CEMS_SurfaceFields_2022 fields can be used independently for a wide range of applications, including as input
23 of hydrological, Earth System or environmental modelling, or for carrying out general analyses across spatial
24 scales, ranging from global and regional to local levels (especially useful for regions outside Europe), expected to
25 improve accuracy, detail, and realism of applications.

26 **1 Introduction**

27 Current numerical Earth system models are highly complex. Thanks to the availability of High Performance
28 Computers, cloud computing, and a wide range of high-resolution environmental data derived from the use of
29 ground, unconventional and satellite measurement sensors, numerical global models are even able to reach
30 kilometre-scale horizontal resolution. But increase in spatial resolution also means that the Earth system and
31 environmental models have to represent more surface and atmospheric processes and their interactions, which can
32 become challenging, for example in complex orographic areas. Model accuracy heavily depends on the quality of
33 the input surface fields (i.e. how realistic and up-to-date they are), and it is essential to minimise errors in surface
34 fields. New high-resolution (i.e. 10-100 m) surface datasets based on daily satellite observations are now
35 frequently released and continuously supported by e.g. the Copernicus program (e.g. Global Land Cover:
36 Buchhorn et al., 2021; GHSL-BUILT-S: Pesaresi and Politis, 2022; Schiavina et al., 2022), which helps in
37 achieving the goal of minimising surface field errors. It was shown, e.g. in Kimpson et al. (2023), that the use of
38 accurate and up-to-date underlying information to generate model's input surface fields can substantially reduce
39 skin temperature errors even at 30 km horizontal resolution (Kimpson et al., 2023).

40 Following the digital revolution of cloud archiving and computing, where data, software and information
41 technology (IT) infrastructure can be accessed by anyone from everywhere, the Earth systems and environmental
42 modelling community has also moved from codes developed by a single organisation and few contributors, to so-
43 called 'community models' where a reference code is open for free use and/ or development according to sharing
44 principles. Such models include Joint UK Environmental Simulator JULES, a land surface model whose
45 development is coordinated by the UK Met Office and UKCEH (Best et al., 2011; Clark et al., 2011; Matthews
46 et al., 2022), OpenIFS, a Numerical Weather Forecast model available to external users for research and training
47 (Sparrow et al., 2021; Carver, 2022; Huijnen et al., 2022; Köhler et al., 2023), the Community Land Model CLM,
48 an Earth System Model with strong climate component maintained by the National Centre for Atmospheric
49 Research but available for use by the wider research community (Lawrence et al., 2019), or LISFLOOD-OS, a
50 spatially distributed water resources model developed by the Joint Research Centre (JRC; Van Der Knijff and De
51 Roo, 2008) and available for use and development through a share code repository (available online: [https://ec-
52 jrc.github.io/lisflood/#lisflood](https://ec-jrc.github.io/lisflood/#lisflood); <https://ec-jrc.github.io/lisflood-code/>, last accessed: 21.01.2024).

53 To promote the seamless development of science, and facilitate research community efforts in working with the
54 same code and input data, providing feedback, and improving the code and the data itself, powerful web-based
55 platforms can be used. One of them is the Google Earth Engine (GEE; Gorelick et al., 2017), a free-of-charge
56 platform that provides easy, web-based access to an extensive catalogue of satellite imagery and other geospatial
57 data in an analysis-ready format. The data catalogue is embedded into Google computing platform that lets you
58 easily implement all personal workflows, which facilitates global-scale analysis and visualization (GEE: FAQ,
59 2023). GEE was chosen for the generation of a new vast surface field set due to its high resolution data catalogue
60 and powerful computation capabilities.

61 This manuscript presents the methodology used to prepare the CEMS_SurfaceFields_2022 dataset containing all
62 surface fields necessary to run the LISFLOOD-OS model at resolutions ~2 km at the equator or 1 arc min (over
63 Europe) and ~6 km at the equator or 3 arc min (globally). CEMS_SurfaceFields_2022 were used in the set-up of
64 the Early Warning Systems of the Copernicus Emergency Management Service of the European Union for the
65 European (European Flood Awareness System EFAS version 5; Smith et al., 2016; information available online:
66 <https://www.efas.eu/>, last accessed: 21.01.2024) and global (Global Flood Awareness System GloFAS version 4;
67 Hirpa et al., 2018; Alfieri et al., 2020; Harrigan et al., 2023; information available online:
68 <https://www.globalfloods.eu/>, last accessed: 21.01.2024) domains operational in December 2023 (EFASv5 and
69 GloFASv4). Details on raw data collection, scientific protocol, and technical methods aim to allow the adequate
70 understanding and interpretation of the surface field datasets, and for any interested user to generate their own
71 datasets by replicating or adapting the workflow to different fields, geographical domain, spatial resolution, or
72 content as relevant for downstream application. The manuscript is structured as follows: Section 2 provides an
73 overview of the surface fields, explains the criteria to select reference data, where and how they were processed,
74 and outlines the general methodology to produce the surface fields; Section 3 to Section 8 details the reference
75 data and specific methodology applied to each surface field category, including examples of application; Section
76 9 provides all the relevant information for data access; Section 10 discusses the challenges of creating a consistent
77 high resolution continental and global scale set of consistent surface fields and the opportunities disclosed by their
78 availability.

79 **2 Surface fields for distributed environmental modelling**

80 **2.1 General information**

81 Environmental models, especially land surface and hydrological models, simulate how water moves across
82 canopy, surface, subsurface, ground and eventually river channels using mechanistic equations that describe the
83 physics of these processes. Each model represents processes with more or less complexity, depending on the
84 model purpose and expected output (Rosbjerg and Madsen, 2006). With most represented terrestrial processes
85 depending on the landscape, information describing the spatial variation in the geophysical and vegetation
86 characteristics is needed. Such characteristics include morphological features (e.g. channel geometry, orography
87 or slope), soil hydraulic property, land and vegetation features (e.g. ecosystem cover type, leaf area index (LAI),
88 evaporation rates, crop type, planting and harvesting dates), and if relevant, human intervention information such
89 as population density or type of water usage.

90 LISFLOOD is a semi-distributed, physically based hydrological model which has been designed for the modelling
91 of rainfall-runoff processes in large and transnational catchments (Bates and De Roo, 2000; De Roo et al., 2000;
92 De Roo et al., 2001; Van Der Knijff and De Roo, 2008; Van Der Knijff et al., 2010; Burek et al., 2013). In its
93 most prominent application, LISFLOOD is used by the Copernicus Emergency Management Services' EFAS and
94 GloFAS to provide medium range and seasonal riverine flow forecasts (Alfieri et al., 2020). LISFLOOD is also
95 widely used for a variety of applications, including water resources assessment (drought forecast); analysis of the
96 impacts of land use changes, river regulation measures, water management plans; climate change analysis (e.g.
97 Vanham et al., 2021).

98 To facilitate users' uptake and enable the seamless development of science, LISFLOOD has been released as open
99 source in 2019, i.e. LISFLOOD-OS. The open-source suite includes the LISFLOOD hydrological model and a set
100 of auxiliary tools for model setup, calibration, and post-processing of the results. For instance, the pre-processor
101 LISFLOOD-LISVAP can be used to compute evapotranspiration, which is one of the three meteorological
102 variables, along with total precipitation and average temperature, strictly required as input to the hydrological
103 model.

104 The modelling of runoff processes in different climates and socio-economic contexts then requires a set of raster
105 fields (i.e. set of surface fields presented in this manuscript) to provide information of terrain morphology, surface
106 water bodies, soil properties, land cover and land use features, water demand. The total number of fields range
107 between 66, when only the essential rainfall-runoff processes are modelled, to a total 108 for a more

108 comprehensive model set-up in which, for instance, lakes, reservoirs, water demand for anthropogenic use are
109 included (available online: <https://ec-jrc.github.io/lisflood-model/>, last accessed: 21.01.2024).
110 The main model's field (i.e. in technical for model operation/ running sense) is 'mask' – a Boolean field that
111 defines model boundaries, i.e. grid cells over which the model performs calculations and grid cells which are
112 skipped (e.g. ocean grid cells). Whilst the surface fields described in this manuscript follow specific requirements
113 of the LISFLOOD-OS model, they are a source of versatile information that can be used for any environmental
114 modelling application, either directly, or following a transformation, as relevant, as a full set or as a few consistent
115 fields.

116 2.2 Reference data and methodology

117 To produce CEMS_SurfaceFields_2022 surface fields only open source, freely available, updated as recently as
118 possible, with recognised reference on their quality data sources were used (see Appendix 1 for all relevant
119 reference data details). Note that whilst the majority of surface fields contain no time element, vegetation and
120 water demand fields explicitly describe the annual cycle (vegetation, rice) or annual time evolution (water
121 demand) and therefore have more stringent requirements regarding the data source. Global single-source datasets
122 (e.g. Te Chow, 1959; Supit et al., 1994; Allen et al., 1998; Buchhorn et al., 2021) were favoured to regional and/
123 or multiple data sources that needed to be combined in order to produce the required data unless sub-set
124 information was of much better quality (e.g. Moiret-Guigand, 2021). CEMS_SurfaceFields_2022 surface fields
125 are based on 25 different data sources and consist of 140 gridded fields grouped into six following groups: (i)
126 catchment morphology and river network, (ii) land use, (iii) vegetation cover type and properties, (iv) soil
127 properties, (v) lake information, and (vi) water demand.

128 Considering the high resolution (i.e. hundreds of meters) and volume of data (i.e. GB) of most input datasets used
129 to generate the surface fields, a high performing data manipulation platform was needed. GEE (Gorelick et al.,
130 2017) was selected as it provides (embedded) a vast high resolution data catalogue (e.g. ready available MERIT
131 DEM elevation dataset, CGLS-LC100 and CLC2018 land cover datasets) and powerful computation capabilities.
132 It also allows to upload any raster and vector data (e.g. GeoTiff or shapefiles) and to conduct each surface field
133 tailored computations. All GEE scripts were written in JavaScript to produce GeoTiff files, converted to the final
134 file format (NetCDF) locally after transfer from GEE platform.

135 To ensure a consistent representation of physical processes at all scales, surface fields should be as coherent as
136 possible among each other – between variables and across scales. Coherency can be achieved by using, where
137 possible, the same input datasets to derive different field types (e.g. unique forest information input to create all
138 forest-related surface fields), and making sure spatial aggregation or disaggregation across scales results in
139 expected values. Figure 1 shows a simplified scheme that relates input datasets (e.g. CGLS-LC100) with the
140 resulting surface fields (e.g. surface cover fractions – forest, inland water, and sealed surface fraction fields), also
141 highlighting fields requiring intermediary and sequential steps (e.g. forest fraction is needed to create soil
142 parameter fields over forested and non-forested areas).

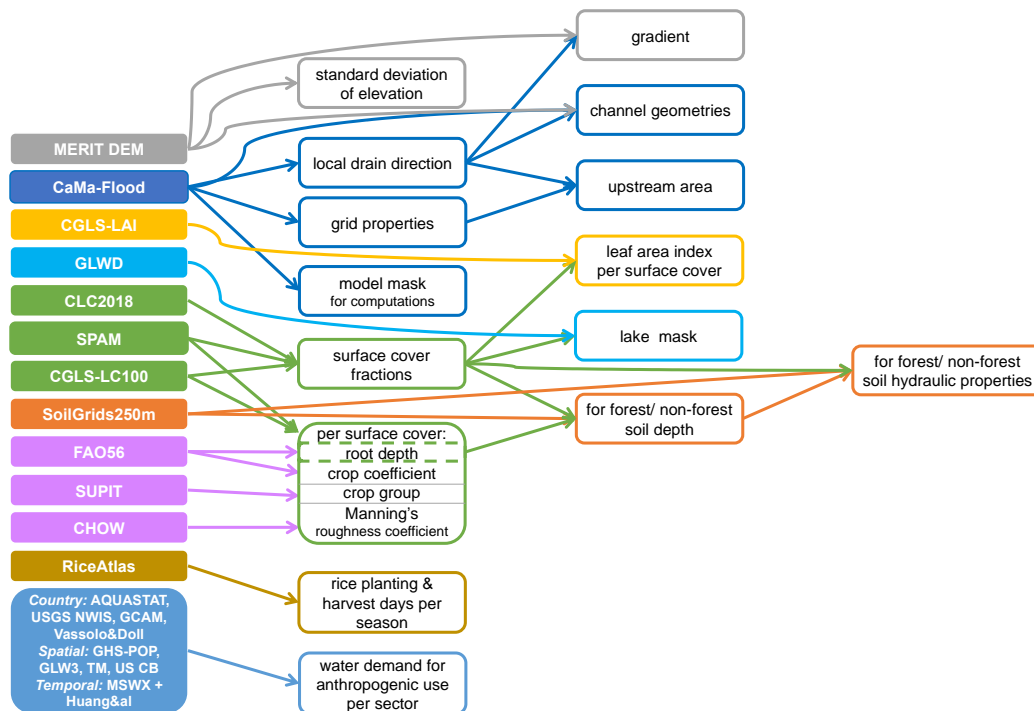
143 For processes with horizontal dependency such as river routing, the relationship between grid cells (e.g. how the
144 grid cells are connected) must be defined first so that all dependent fields can be generated on the same grid
145 coordinates, spatial resolution and using consistent input data. For example, LDD defines how water moves across
146 the model grid cells as a river drainage network (see Figure 2) and strongly depends on elevation data (see Section
147 3 for more details). Because of the complex spatial dependency of a river drainage network, LDD must be created
148 directly from elevation data at the required grid and resolution and cannot be resampled from a previous LDD
149 field of a different grid and/ or resolution. It is then used to define information on the river network, including
150 upstream drainage area and gradient. Note, Figure 1 misses an arrow from MERIT DEM to LDD only because
151 this step was mainly done by CaMa-Flood developers (see Section 3.2 for more details).

152 Four steps are involved in generating a particular surface field (see Table 1), with step 3 being the most complex
153 and varied (see Figure 2 for an example), and step 4 being necessary only for some model specifications (here as
154 required by LISFLOOD, see Table 2).

155 All techniques applied (see Table 1) to generate CEMS_SurfaceFields_2022 are reproduceable to different input
156 data and/ or for different output data specifications. Further details on specific manipulations associated with each
157 field category are given in sections below as relevant, where each section has a table with exact data source used
158 per surface field, and step-by-step description of transformations applied to the data to compute the final fields
159 included in CEMS_SurfaceFields_2022 (full technical descriptions for all fields are explained in the LISFLOOD
160 user guide, available online: https://ec-jrc.github.io/lisflood-code/4_Static-Maps-introduction/, last accessed:
161 21.01.2024). Although the specific requirements for the dataset were defined by LISFLOOD for EFAS (European
162 domain, 1 arc min resolution at mid-latitude of the domain (47.50 N) is ~1.25 km) and GloFAS (Global domain)
163 implementation, summarised in Table 2, they are consistent with requirements of any other environmental models.
164 Regional examples of a sub-set of CEMS_SurfaceFields_2022 are provided to show the level of detail available
165 at each resolution and field, and to emphasise the consistency through all the fields, a critical requirement for

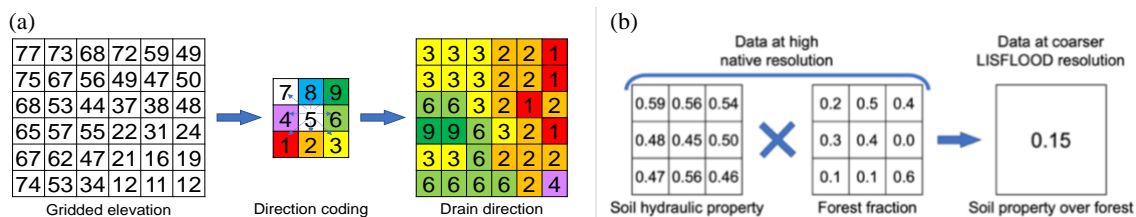
166
167
168

environment modelling and analysis, focusing on three regions of the world: the Po River (Europe), the Amazon River (South America) and the Brahmaputra River (Asia), with additional examples provided in Appendix 4).



169
170
171

Figure 1. Flow chart connecting input datasets and surface fields created. Dashed border denotes intermediate fields, that are not part of the final dataset catalogue.



172
173
174

Figure 2. Examples of data manipulation for (left column, plot a) transformation of elevation data into LDD (done within CaMa-Flood), and (right column, plot b) upscaling with weighted average for one final grid cell of soil hydraulic property over forested area.

175

Table 1. The four steps of a particular surface field generation and associated data manipulations.

Order	Description	Purpose	Function
1	Raw file preparation	Vector gridding, region merging	
		Upscaling (spatial/ temporal aggregation)	Arithmetic mean, mode, sum, standard deviation (weighted) resampling from auxiliary data
2	Unit conversion	Converting values from native to fraction per grid cell	Surface area, percentage or categorical to fractions per grid cell (see Appendix 2 for more details)
3	Value computation	Transforming	Mathematical equation/ function needed to generate the output variable
		Reprojecting	Interpolation (changing grid, preserving resolution in meters)
		Upscaling (spatial [default]/ temporal aggregation)	Arithmetic mean, mode, sum, standard deviation (weighted) resampling from auxiliary data (changing resolution, preserving grid)
		Downscaling (spatial [default]/ temporal disaggregation)	Nearest neighbour (changing resolution, preserving grid)
4	Zero/ NoData filling	Limiting	Force a minimum/ maximum value to satisfy e.g. calculation precision, physical meaning and/ or model requirement
		Replace zero/ NoData by the most appropriate values	LIGHT. Constant value, unweighted global mean, unweighted global mode DEEP. Values from next coarser resolution (up to an agreed maximum resolution); if still missing, method LIGHT

176
177

Table 2. Dataset files technical specifications.

<i>Type</i>	<i>Specification</i>
Format	NetCDF
Projection	EPSG:4326 - WGS84: World Geodetic System
Horizontal resolution	Europe: 1 arc min (~1.86 km at the equator) [file size 4530x2970 grid cells]
	Globe: 3 arc min (~5.57 km at the equator) [file size 7200x3600 grid cells]
Domain bound	Europe: [North = 72.25 N; South = 22.75 N; West = 25.25 W; East = 50.25 E]
	Globe: [North = 90.00 N; South = 90.00 S; West = 180.00 W; East = 180.00 E]
Missing value (i.e. NoData) location	Over land: none
	Over ocean: all ocean grid cells have missing value (i.e. ocean is masked based on ‘mask’ field)
Missing value (i.e. NoData) number	For Integer variable type: 0
	For Real variable type: -999999.0
Variable type	Integer: Int8
	Real: Float32

178 **3 Catchment morphology and river network**

179 **3.1 General information**

180 Morphology and channel shape information are essential for the computation of snow melting, temperature
 181 scaling, and river routing. Statistics such as standard deviation of elevation and other orographic sub-grid
 182 parameters critical for radiation parametrization, especially for shadowing effect, whilst channel geometry fields
 183 are needed to describe overbank inundation and infer inundated areas in wetland methane and soil carbon
 184 modelling, for example. Land morphology is derived from elevation and its variability within a single cell can be
 185 represented through slope, standard deviation, aspect, etc. River drainage information, derived from elevation, is
 186 used to connect the model cells according to the direction of the surface runoff, with channel geometry information
 187 used for routing processes.

188 The dataset contains 14 morphology and river network variables (name in brackets in italics correspond to the
 189 field’s name in the data repository):

- 190 • Morphologic information: local drainage direction (i.e. flow direction from one cell to another; *LDD*,
 191 dimensionless), upstream drainage area (*upArea*, m²), grid cell area (*pixarea*, m²), grid cell length
 192 (*pixleng*, m), standard deviation of elevation (*elvstd*, m), gradient (i.e. elevation gradient; *gradient*, m/m);
- 193 • Kinematic wave equation for routing: channel bottom width (*chanbw*, m), channel length (*chanlenght*,
 194 m), channel gradient (*changrad*, m/m), Manning’s roughness coefficient for channels (*chanman*, s/m^{1/3});
- 195 • River network information: channel mask (i.e. presence of river channel; *chan*, dimensionless), channel
 196 side slope (i.e. channel’s horizontal distance divided by vertical distance; *chans*, m/m);
- 197 • Open water evaporation: bankfull channel depth (*chanbnkf*, m), channel flood plain (i.e. width of the area
 198 where the surplus of water is distributed when the water level in the channel exceed the channel depth;
 199 *chanflpn*, m).

200 **3.2 Reference data and methodology**

201 Environmental models require an accurate description of terrain and hydro-morphology to represent the
 202 hydrodynamics at the spatial resolution of the model. Here all catchment morphology and river network fields are
 203 derived from (i) **The Catchment-based Macro-scale Floodplain (CaMa-Flood) Global River Hydrodynamics**
 204 **Model v4.0 maps** (further referred as CaMa-Flood) – that include information on channel length, river topography
 205 parameters, floodplain elevation profile, channel width and channel depth at 3 and 1 arc min resolutions covering
 206 land area from 90 N to 60 S, representative of the year 2017, and (ii) **The MERIT DEM: Multi-Error-Removed**
 207 **Improved-Terrain Digital Elevation Model v.1.0.3** (further referred as MERIT DEM) – a high accuracy global
 208 DEM at 3 arc second resolution (~90 m at the equator) covering land area from 90 N to 60 S, representative of
 209 the year 2018 (for reference data details see Appendix 1). All fields follow a complex sequential workflow (see
 210 Figure 3 and Table 1). Note that whilst some river network fields were already directly available from the CaMa-
 211 Flood catalogue (e.g. LDD, channel length), they had to be adapted to the specific requirements of LISFLOOD,
 212 specifically consistent with an interconnected river network described by the D8 algorithm (O’Callaghan and
 213 Mark, 1984; Figure 2a) different to that used by the CaMa-Flood algorithm.

214

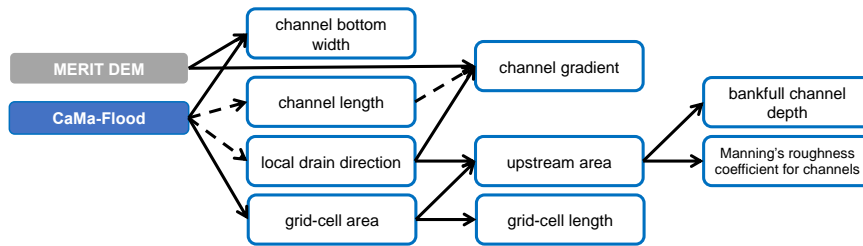


Figure 3. Workflow of complex manipulations to create some of the morphology and river network fields; solid arrows indicate a function transformation, dashed – modification of existing input data to LISFLOOD specifications.

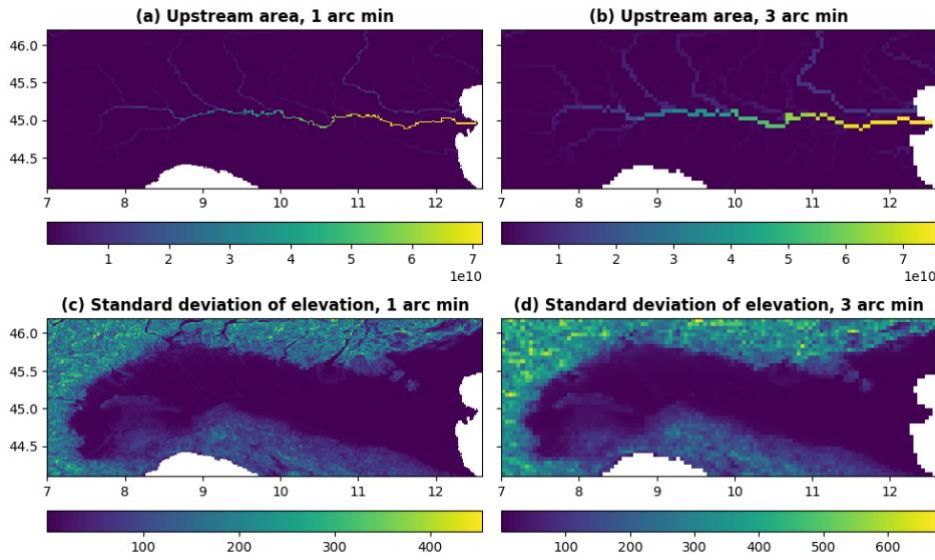
Table 1. Morphology and river network fields, their description, data source and applied transformation; * denotes transformation following Burek et al. (2014); name in brackets in italics next to each field correspond to the name in the data repository.

Field type	Description	Data source (variable)	Transformation
Local drainage direction (<i>LDD</i>)	Connects every grid cell forming a river network from springs to mouth	CaMa-Flood (flwd)	Direction coding, ensuring grid cell connectivity
Grid cell area (<i>pixarea</i>)	Area of every grid cell	CaMa-Flood (flwd)	Grid cell area based on a given coordinate reference system and resolution
Grid cell length (<i>pixlength</i>)	Length of every grid cell	<i>pixarea</i>	$pixlength = \frac{pixarea}{resolution}$, where <i>resolution</i> – 1.86 km and 5.57 km for 1 and 3 arc min respectively
Upstream drainage area (<i>upArea</i>)	Accumulated area of all connected grid cells of the LDD from springs (start; lowest values) to mouth (end; highest values)	<i>LDD</i> ; <i>pixarea</i>	PCRaster Accuflux function (Karssenberget al., 2010)
Standard deviation of elevation (<i>elvstd</i>)	Amount of elevation variation within a grid cell	MERIT DEM	Upscaling (spatial) with standard deviation
Gradient (<i>gradient</i>)	Elevation gradient between two connected grid cells	MERIT DEM; <i>LDD</i>	$gradient = \frac{abs(elv_{uc} - elv_{dc})}{D_{uc,dc}}$, where <i>elv</i> – elevation, <i>uc</i> and <i>dc</i> – upstream and downstream cell, <i>D_{uc,dc}</i> – distance between upstream and downstream cells
Channel bottom width (<i>chanbw</i>)	Width of the bottom of the channel	CaMa-Flood (width); <i>upArea</i>	Recomputing zero and negative values based on equation* $chanbw = upArea \cdot 0.0032$
Channel length (<i>chanlength</i>)	Length of river channel in each grid cell (can exceed grid-size to account for meandering river)	CaMa-Flood (rivlen)	No transformation was carried out
Channel gradient (<i>changrad</i>)	Gradient (slope) of river channel inside a grid cell	MERIT DEM; <i>LDD</i> ; <i>chanlength</i>	$changrad = \frac{abs(elv_{uc} - elv_{dc})}{chanlength_{uc}}$, where <i>elv</i> – elevation, <i>uc</i> and <i>dc</i> – upstream and downstream cell; Note: <i>LDD</i> is used to define <i>uc</i> and <i>dc</i>
Manning's roughness coefficient for channels (<i>chanman</i>)	Manning's roughness coefficient of river channel for each grid cell	MERIT DEM; <i>upArea</i>	Transformation based on equation* $chanman = 0.25 + 0.015 \cdot \min\left(\frac{50}{upArea_{km^2}}, 1\right) + 0.030 \cdot \min\left(\frac{elv_m}{2000}, 1\right)$, where <i>elv</i> – elevation, <i>km²</i> and <i>m</i> – values in <i>km²</i> and <i>m</i>
Channel mask (<i>chan</i>)	Channel presence in the grid cell indicator. Note LISFLOOD specific requirement to have channels in every 'mask' grid cell	'mask' (main model's field)	Channel mask is equal to 1 everywhere
Side slope (<i>chans</i>)	Slope of river banks (i.e. horizontal distance divided by vertical distance)		Side slope of all channels is 45°, hence side slope is equal to 1 everywhere

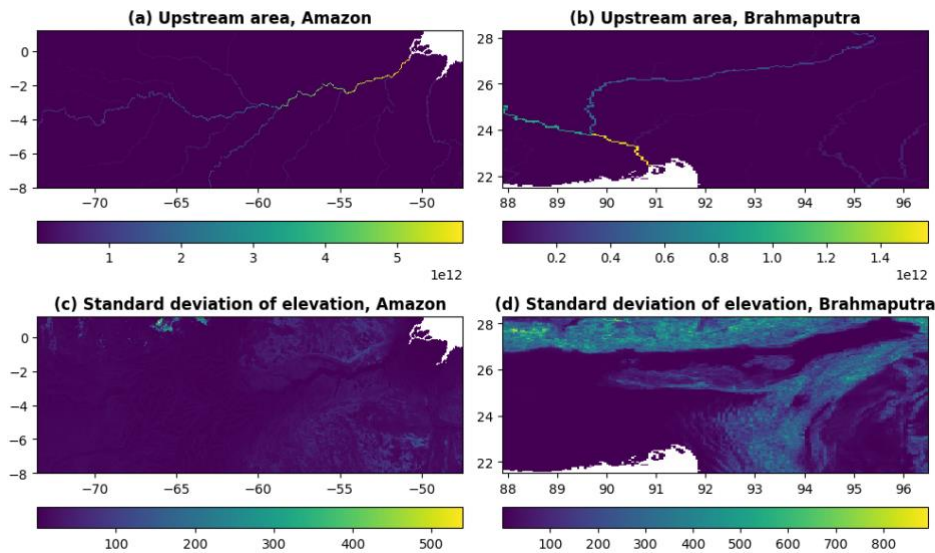
Bankfull channel depth (<i>chanbnkf</i>)	Channel depth (i.e. river bed depth)	<i>upArea</i>	Transformation based on equation* $chanbnkf = 0.27 \cdot upArea_{km^2}^{0.33}$, where <i>km</i> ² – values in km ²
--	--------------------------------------	---------------	---

221 **3.3 Regional examples**

222 Most fields in catchment morphology and river network category are quite technical and hard to interpret. The
 223 ones that can be easy digested are upstream area and standard deviation of elevation which are presented in Figure
 224 3 for Po River area in 1 arc min and 3 arc min resolution, and in Figure 4 for Amazon River and Brahmaputra
 225 River areas at 3 arc min resolution. The field of standard deviation of elevation shows high level of detail over the
 226 Brahmaputra River and the benefit of high resolution dataset is clearly seen over the Po River.
 227



228
 229 **Figure 3.** Upstream drainage area in square meters (upper row, plots a and b) and standard deviation of elevation in
 230 meters (lower row, plots c and d) at 1 arc min (~1.9 km at the equator, left column, plots a and c) and 3 arc min (~5.6
 231 km at the equator, right column, plots b and d) resolution for Po River area in Italy.



232
 233 **Figure 4.** Upstream drainage area in square meters (upper row, plots a and b) and standard deviation of elevation in
 234 meters (lower row, plots c and d) at 3 arc min (~5.6 km at the equator) resolution for Amazon River area (left column,
 235 plots a and c) and Brahmaputra River area (right column, plots b and d).

236 4 Land use fields

237 4.1 General information

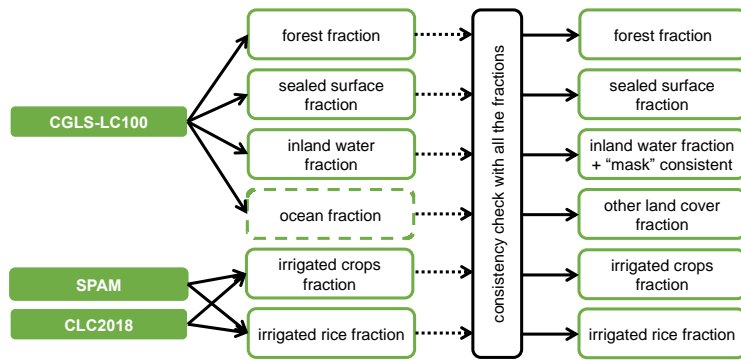
238 Land use is an essential component of environmental models. Many models use a sub-grid cell approach where a
239 single grid cell can include several different land uses with each land use being subject to different prominent
240 physical processes. This approach allows to keep a high level of accuracy when representing how different types
241 of land cover affect e.g. the hydrological cycle (e.g. evaporation is different in urban areas compared to forests)
242 while limiting the increase in computational time. Application of land surface fractions include grid cell weighted
243 average skin temperature calculations, biogenic flux calculations, urban planning, and climate mitigation plan
244 preparation. For example, sealed surface fraction is necessary for carbon budget calculations and trace gas
245 emissions in general, more explicitly for anthropogenic and residential emission calculations, and irrigated crop
246 and irrigated rice fractions (combined with rice planting and harvesting days) useful for crop yield and methane
247 emissions modelling.

248 The dataset differentiates between six different land uses (name in brackets in italics correspond to the field's
249 name in the data repository):

- 250 • Forest: areas where the main hydrological processes are canopy interception, evapotranspiration from
251 canopies, canopies drainage and evapotranspiration, root uptake and evaporation from the soil (fraction
252 of forest; *fracforest*, dimensionless fraction);
- 253 • Sealed surface: impervious areas where there is no water infiltration into the soil, i.e. water is
254 accumulated in the surface depression, yet evaporates, but once the depression is full, water is transported
255 by a surface runoff (fraction of sealed surface; *fracsealed*, dimensionless fraction);
- 256 • Inland water: open water bodies where the most prominent hydrological process is evaporation (fraction
257 of inland water; *fracwater*, dimensionless fraction);
- 258 • Irrigated crops: areas used by agriculture – water is abstracted from ground water and surface water
259 bodies to irrigate the fields. The main hydrological processes connected with the irrigated crops are
260 canopy interception, evapotranspiration from canopies, canopies drainage and evapotranspiration, root
261 uptake and evaporation from the soil (fraction of all irrigated crops, excluding rice; *fracirrigated*,
262 dimensionless fraction);
- 263 • Irrigated rice: areas used to grow rice with flooded irrigation agricultural technique, when water is
264 abstracted from the inland water bodies and delivered to the rice fields. The main hydrological processes
265 connected with rice fields are soil saturation, flooding, rice growing phase, soil drainage phase (fraction
266 of irrigated rice; *fracrice*, dimensionless fraction);
- 267 • Other land cover: used in canopy interception, evaporation from the canopies, canopy drainage, plant
268 evapotranspiration, evaporation from the soil hydrological processes. The relative importance of these
269 processes depends on the LAI (fraction of other cover types; *fracother*, dimensionless fraction).

270 4.2 Reference data and methodology

271 In models explicitly accounting for sub-grid variability, the fraction of each land use in every cell must be provided
272 so that process representation for each land use can be weighted accordingly. Here the majority of land use fields
273 are derived from **The Copernicus Global Land Service (CGLS) Land Cover (LC) 100m map** (further referred
274 as CGLS-LC100) – a set of global land cover maps at 100 m resolution covering land and ocean area from 90 N
275 to 60 S, representative of the year 2015; rest of the land use fields (i.e. irrigated crops and irrigated rice fractions)
276 are derived from (i) **The Spatial Production Allocation Model (SPAM) – Global Spatially-Disaggregated
277 Crop Production Statistics Data for 2010 v2.0** (further referred as SPAM2010) – a global dataset with crop
278 distribution and production information at 10 km (5 arc min) resolution covering land area from 90 N to 60 S,
279 representative of the year 2010, and (ii) **The Coordination of Information on the Environment (CORINE)
280 Land Cover (CLC) inventory for 2018** (further referred as CLC2018) – a set of maps describing the land cover/
281 land use status at 100 m resolution covering land area over Europe (i.e. 39 countries), representative of the time
282 period 2017-2018 (for reference data details see Appendix 1). The derivation of fractions of the five land use
283 classes used in LISFLOOD (and additional ocean fraction for consistency check) each follow specific steps (see
284 Figure 5) summarised in Table 2. Note that LISFLOOD requires all 'mask' (main model's field) grid cells to have
285 at least one non-zero fraction type, hence the extra step in the generation of the inland water fraction field was to
286 set empty grid cells (i.e. grid cells that based on the data source are fully covered with ocean) as fully covered
287 with inland water.
288



289
290
291

Figure 5. Workflow of complex manipulations to create land use fields; solid arrows indicate a function transformation, dotted – upscaling; dashed boxes indicate the intermediate fields used for other field generation.

292
293
294

Table 2. Fraction of land use fields, their description, data source and applied transformations; ‘sum’ refers to the sum of all fractions except ‘other land cover fraction’; cells with bold italic show required intermediate fields; name in brackets in *italics* next to each field correspond to the name in the data repository.

<i>Field type</i>	<i>Description</i>	<i>Data source (variable)</i>	<i>Transformation (in order)</i>
Forest fraction (<i>fracforest</i>)	Evergreen and deciduous needle leaf and broad leaf tree areas	CGLS-LC100 (tree-coverfraction)	Unit conversion % to fraction; Reprojecting and upscaling to final grid and resolution with mean; Consistency check with other fractions
Sealed surface fraction (<i>fracsealed</i>)	Urban areas, characterizing the human impact on the environment	CGLS-LC100 (urban-coverfraction)	Unit conversion % to fraction, scaled by 0.75 ¹ ; Reprojecting and upscaling to final grid and resolution with mean; Consistency check with other fractions
Inland water fraction (<i>fracwater</i>)	Rivers, freshwater and saline lakes, ponds and other permanent water bodies over the continents	CGLS-LC100 (water-permanent-coverfraction)	Force Fox Basin and Caspian Sea to be fully covered with water; Unit conversion % to fraction; Reprojecting and upscaling to final grid and resolution with mean; Consistency check with other fractions; Cross-checking with ‘mask’ and forcing empty grid cells as inland water
Irrigated crops fraction (<i>fracirrigated</i>)	Irrigated areas of all possible crops excluding rice	SPAM (spam2010v1r0_global_physical-area_CROP_i, 41 crops rice excluding)	Shapefile gridding to its native resolution (~10 km); Unit conversion ha to fractions; Reprojecting and downscaling to CLC2018 grid and resolution (~100 m) with nearest neighbour
		CLC2018 (landcover = ‘212’)	Unit conversion class to fraction
			Merging SPAM- and CLC2018-derived fractions, priority to CLC2018; Reprojecting and upscaling to final grid and resolution with mean; Consistency check with other fractions
Irrigated rice fraction (<i>fracrice</i>)	Irrigated areas of rice	SPAM (spam2010v1r0_global_physical-area_RICE_i)	Shapefile gridding to its native resolution (~10 km); Unit conversion ha to fractions; Reprojecting and downscaling to CLC2018 grid and resolution (~100 m) with nearest neighbour
		CLC2018 (landcover = ‘213’)	Unit conversion class to fraction
			Merging SPAM- and CLC2018-derived fractions, priority to CLC2018; Reprojecting and upscaling to final grid and resolution with mean; Consistency check with other fractions

¹ For the sealed surface fraction, it is assumed that water can infiltrate in roughly 25 % of urban areas at kilometre scale through e.g. trees along the road, bushes along the fence, grass or moss between concrete tiles or cobble stones.

Other land cover fraction (<i>fracother</i>)	Agricultural areas, non-forested natural area, pervious surface of urban areas	Non-negative residual from 1 subtracting 'sum' of all other fractions	$fracother = \max((1 - sum), 0)$
Ocean fraction (<i>fracocean</i>)	Oceans	CGLS-LC100 (discrete_classification = '200')	Unit conversion class to fraction; Forcing NoData to zero over 'mask' grid cells, otherwise – fully covered; Reprojecting and upscaling to final grid and resolution with mean; Consistency check with other fractions

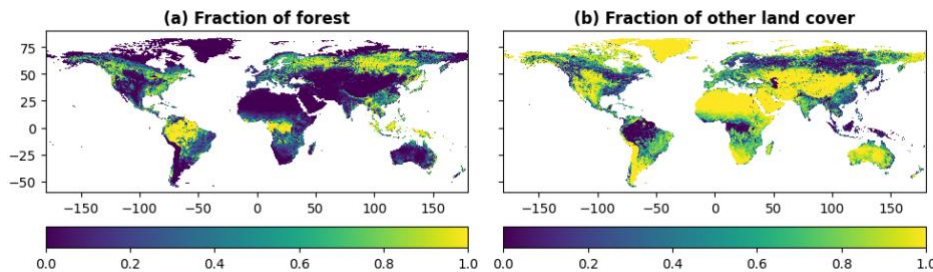
295

296 To ensure consistency between fractions, the sum of all fraction fields must be 1 at any resolution. When sum is
 297 greater than 1, the inland water fraction value is assumed correct (input data corrected prior computation over Fox
 298 Basin and Caspian Sea) and all other fractions are corrected (*fracXX*) following Eq. (1):

$$299 \quad fracXX = fracXX_{raw} \left(1 - \frac{fracwater_{raw} + fracocean_{raw} + fracforest_{raw} + fracsealed_{raw} + fracirrigated_{raw} + fracrice_{raw} - 1}{fracforest_{raw} + fracsealed_{raw} + fracirrigated_{raw} + fracrice_{raw}} \right), \quad (1)$$

300 where *raw* refers to the original (i.e. before consistency check) fraction of *XX* which can be the forest, irrigated
 301 crops, rice and sealed surfaces.

302 The generated fraction fields, e.g. forest (see Figure 6a) and other land cover (see Figure 6b), have generally good
 303 consistency with other up-to-date products like ESA CCI Land Cover time-series v2.0.7 (ESA CCI map viewer
 304 <https://maps.elie.ucl.ac.be/CCI/viewer/>; Defourny et al., 2017).
 305

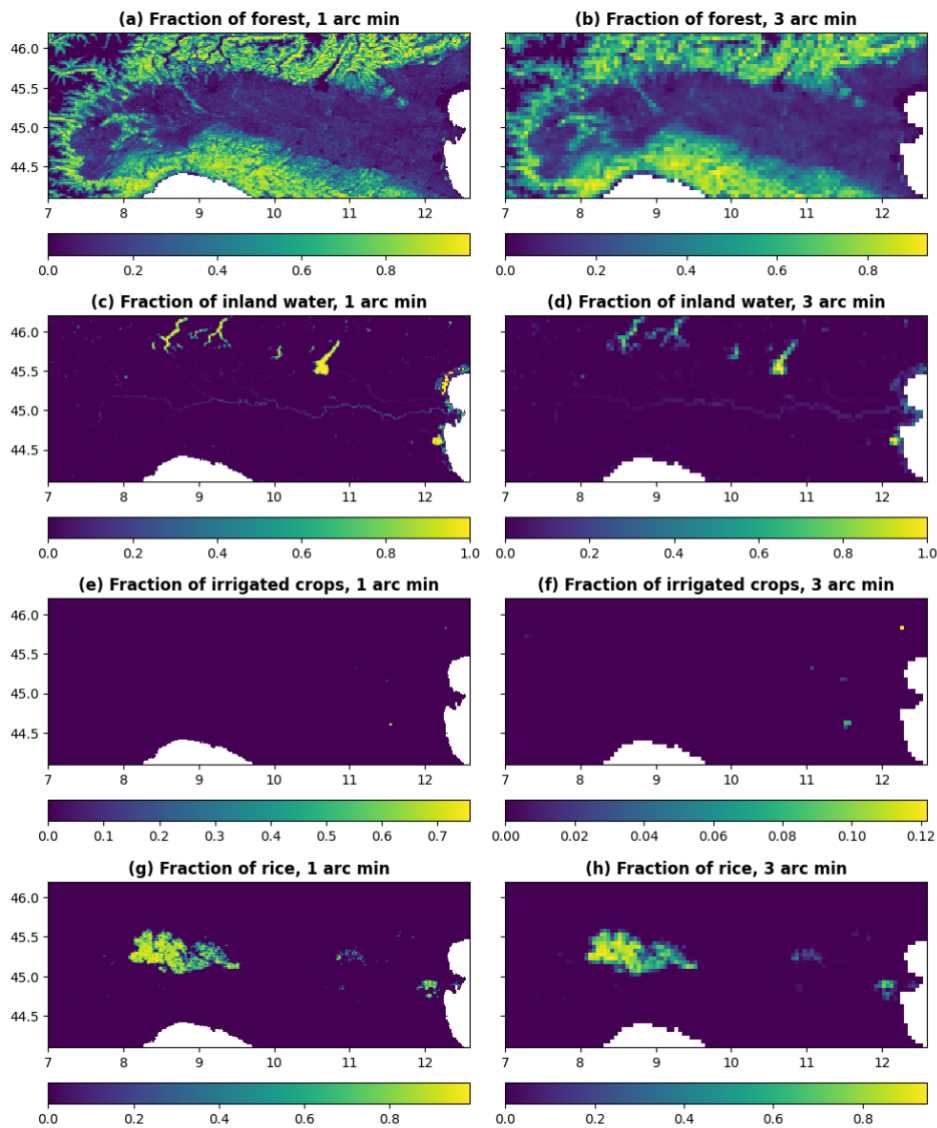


306

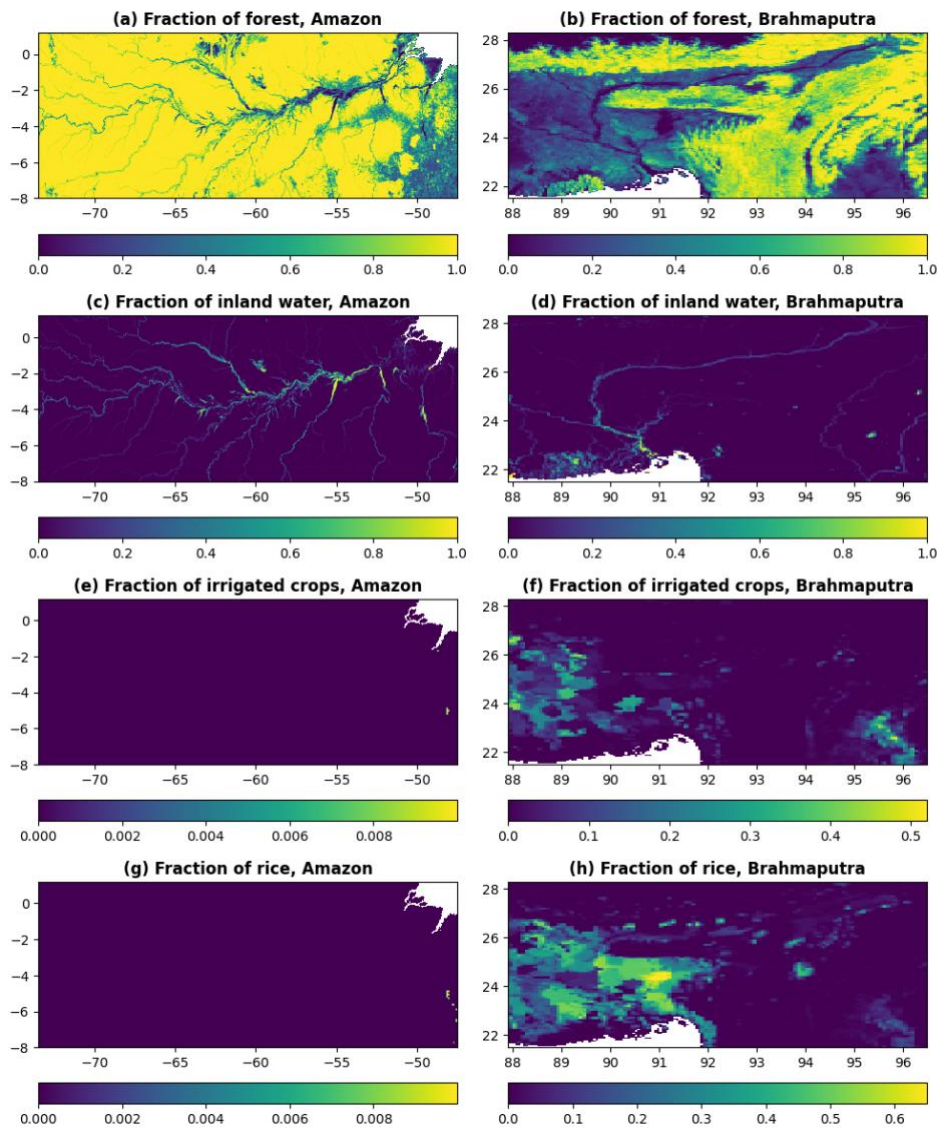
307 **Figure 6. Fraction of forest (left column, plot a) and fraction of other land cover (right column, plot b) at 3 arc min**
 308 **(~5.6 km at the equator) resolution for global region.**

309 4.3 Regional examples

310 All fields in land use category are easy to interpret as they represent the fraction of grid cell covered by one or
 311 another surface cover type. The most interesting ones are fraction of forest, fraction of inland water, fraction of
 312 irrigated crops, and fraction of rice which are presented in Figure 7 for Po River area in 1 arc min and 3 arc min
 313 resolution, and in Figure 8 for Amazon River and Brahmaputra River areas at 3 arc min resolution. With high
 314 level of detail visible for the fields of fraction of forest and fraction of inland water (e.g. Amazon River) especially
 315 at the highest spatial resolution (Po River).
 316



317
 318 **Figure 7.** Fraction of forest (upper row, plots a and b), fraction of inland water (second row, plots c and d), fraction of
 319 irrigated crops (third row, plots e and f), and fraction of rice (lower row, plots g and h) at 1 arc min (~1.9 km at the
 320 equator, left column, plots a, c, e and g) and 3 arc min (~5.6 km at the equator, right column, plots b, d, f and h)
 321 resolution for Po River area in Italy.



322
 323 **Figure 8.** Fraction of forest (upper row, plots a and b), fraction of inland water (second row, plots c and d), fraction of
 324 irrigated crops (third row, plots e and f), and fraction of rice (lower row, plots g and f) at 3 arc min (~5.6 km at the
 325 equator) resolution for Amazon River area (left column, plots a, c, e and g) and Brahmaputra River area (right column,
 326 plots b, d, f and h).

327 5 Vegetation properties

328 5.1 General information

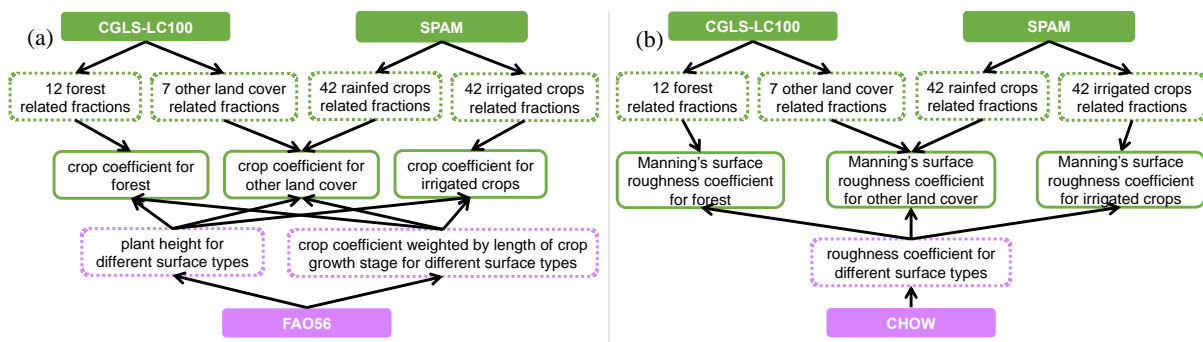
329 Vegetation-related information contributes to the computation of precipitation interception, evaporation,
 330 transpiration, and root water uptake. Depending on the model, vegetation dynamics can be represented with
 331 different degrees of complexity including in hydrology processes, vegetation growth and feedback on climate
 332 (Bonan et al., 2002). Rice being the world's most important food crop and having specific water demands, its
 333 water cycle is often considered explicitly, with planting and harvesting dates being critical information to represent
 334 the inter-annual variability in its water demand, provided the maximum three growing seasons. The variables
 335 allow to model how vegetation affects the hydrology, with a particular focus on root water uptake and transpiration
 336 depending on vegetation type and vegetation state (e.g. water stress conditions). For example, the crop group
 337 number depends on the critical amount of soil moisture below which water uptake from plants is reduced as they
 338 start closing their stomata. Alternative use of fields such as the Leaf Area Index LAI include biomass allocation,
 339 which can be used for fire danger forecasting, and carbon stock monitoring, whilst rice planting/ harvesting days
 340 are important for yearly cycle of methane modelling.

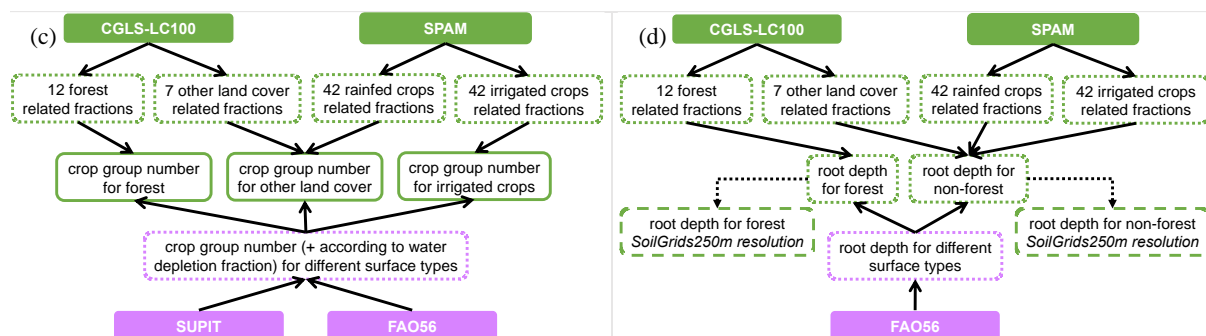
341 The dataset describes vegetation properties through four variables (note that LAI consists in total of 36 10-day
 342 average fields) for each of forest (_f), irrigated crops (_i) and other land cover types (_o), and another six (two
 343 types times three seasons) variables for rice (name in brackets in italics correspond to the field's name in the data
 344 repository):

- 345 • Transpiration rate: crop coefficient (*cropcoef_f*, *cropcoef_i*, *cropcoef_o*, dimensionless);
- 346 • Water uptake: crop group number (*cropgrpn_f*, *cropgrpn_i*, *cropgrpn_o*, dimensionless);
- 347 • Surface runoff generation and water routing: Manning's surface roughness coefficient (*manning_s_f*,
 348 *manning_s_o*, $s/m^{1/3}$), rice planting and harvesting days (*riceplantingday1*, *riceplantingday2*,
 349 *riceplantingday3*, calendar day number; *riceharvestday1*, *riceharvestday2*, *riceharvestday3*, calendar
 350 day number);
- 351 • Water interception and evaporation: leaf area index (*laif*, *laii*, *laio*, m^2/m^2).

352 5.2 Reference data and methodology

353 In complement to the land use fraction, the distribution of vegetation type and characteristics is required to capture
 354 the difference in environmental processes such as water intake of evaporation to be represented accurately. Here
 355 the vegetation properties are derived from many data sources using maps to account for the species spatial
 356 distribution (i.e. CGLS-LC100 and SPAM2010) and tables to obtain associated hydro-dynamics properties for
 357 crops (i) **The Food and Agriculture Organisation (FAO) of the United Nations Irrigation and Drainage
 358 Paper No. 56** (further referred as FAO56) – a publication covering geographically referenced statistics for crop
 359 development stages, crop coefficients, crop height, rooting depth, and soil water depletion fraction for common
 360 crops found across the world, (ii) **Burek et al. (2014)** – a publication covering summarised information for crop
 361 coefficients, rooting depth, crop group number and Manning's surface roughness coefficient for different surface
 362 types, (iii) **Intara et al. (2018)** – a publication covering oil palm roots architecture, and (iv) **The Wofost 6.0 crop
 363 simulation model description** (further referred as SUPIT) – a publication covering crop group information for
 364 several crops as examples, and relation of a crop group from water depletion fraction; for river hydraulics **The
 365 Open-Channel Hydraulics manual** (further referred as CHOW) – a publication containing information on
 366 roughness coefficient over different surfaces. Time evolution of vegetation is based on **The Copernicus Global
 367 Land Service (CGLS) Leaf Area Index (LAI) 1km Version 2 collection** (further referred as CGLS-LAI) – a
 368 set of global maps without missing data describing vegetation dynamics at 10-day intervals at 1 km resolution
 369 covering land area from 90 N to 60 S and representative of the 10-year period of 2010-2019; time evolution of
 370 crops is based on **The RiceAtlas v3** (further referred as RiceAtlas) – a spatial database of global rice calendars
 371 and production at 1 km resolution for the national production totals to match the years 2010-2012 (for reference
 372 data details see Appendix 1). This requires assumptions to be made in case different sources did not contain the
 373 same information, and transformations to be applied depending on the vegetation type. The main data sources and
 374 general transformation steps (see Figure 9) to derive the 18 vegetation properties fields are summarised in Table
 375 3 and following text. Note that 'crop group number' variable corresponds to a water depletion value and can be
 376 averaged across different crop types.
 377





378 **Figure 9. Workflow of complex manipulations to create some of the vegetation property fields, e.g. crop coefficient (left**
 379 **column, upper row, plot a), Manning’s surface roughness coefficient (right column, upper row, plot b), crop group**
 380 **number (left column, lower row, plot c), root depth (right column, lower row, plot d); solid arrows indicate a function**
 381 **transformation, dotted – upscaling; dashed boxes indicate the intermediate fields used for other field generation, dotted**
 382 **– the fields only used for the vegetation-related fields.**

383 **Table 3. Vegetation property fields, their description, data source and applied transformations; cells with bold italics**
 384 **show required intermediate fields; name in brackets in italics next to each field correspond to the name in the data**
 385 **repository.**

<i>Field type</i>	<i>Description</i>	<i>Data source</i>	<i>Transformation (in order)</i>
Crop coefficient for forest, irrigated crops and other land cover type (<i>cropcoef_f</i> , <i>cropcoef_i</i> , <i>cropcoef_o</i>)	Ratio between the potential (reference) evapotranspiration rate, in mm/day, and the potential evaporation rate of a specific crop (averaged by time and ecosystem type)	CGLS-LC100 (discrete_classification = ‘111’, ‘112’, ‘113’, ‘114’, ‘115’, ‘116’, ‘121’, ‘122’, ‘123’, ‘124’, ‘125’, ‘126’ [forest types], ‘20’, ‘30’, ‘40’, ‘60’, ‘70’, ‘90’, ‘100’ [other land cover types])	Force Fox Basin and Caspian Sea to be fully covered with water; Unit conversion class to fraction (in total 12 forest related and 7 other land cover related fraction fields); Reprojecting and upscaling to final grid and resolution with mean
		SPAM (spam2010v1r0_global_physical-area_CROP_i/r, 42 crops, ‘i’ – irrigated, ‘r’ – rainfed)	Shapefile gridding to its native resolution (~10 km); Unit conversion ha to fractions (in total 42 irrigated crop related and 42 rainfed crop related fraction fields); Reprojecting and downscaling to final grid and resolution with nearest neighbour; Limiting values to 0.0-1.0 interval
		FAO56 (Table 11, 12 – information on crop coefficient and crop height); Intara et al. (2018); Burek et al. (2014)	Average crop coefficient value across climate zones for each crop growing stage and crop/ land cover type; Weighted average of crop coefficient per different crop growth stages (weighted by stage duration in days if available, otherwise mean); Average crop height value across climate zones for each crop/ land cover type
			Weighted average of relevant crop coefficient for forest, irrigated crops and other land cover type (weighted by crop height and fraction) following Eq. (2); Note: for other land cover type computation of crop coefficient of all rainfed crops is used for CGLS-LC100 (discrete_classification = ‘40’); Zero/ NoData filling with global mean
Crop group number for forest, irrigated crops and other land cover type (<i>cropgrpn_f</i> , <i>cropgrpn_i</i> , <i>cropgrpn_o</i>)	Represents a vegetation type and is an indicator of its adaptation to dry climate (averaged by ecosystem type)	CGLS-LC100 (discrete_classification = ‘111’, ‘112’, ‘113’, ‘114’, ‘115’, ‘116’, ‘121’, ‘122’, ‘123’, ‘124’, ‘125’, ‘126’ [forest types], ‘20’, ‘30’, ‘40’, ‘60’, ‘70’, ‘90’, ‘100’ [other land cover types])	Same steps as for crop coefficient
		SPAM (spam2010v1r0_global_physical-	Same steps as for crop coefficient

		area_CROP_i/r, 42 crops, 'i' – irrigated, 'r' – rainfed)	
		FAO56 (Table 22 – information on crop depletion fraction); SUPIT (Table 6.1, 6.2 – information on crop groups); Burek et al. (2014)	Applying function (SUPIT) to water depletion fraction (FAO56) for each crop/ land cover type $cropgrpn = 10 \cdot fr_{dep} - 1.5$, where fr_{dep} – water depletion fraction; Limiting values to 1.0-5.0 interval; Note: if fr_{dep} missing – using precomputed crop group number (Burek et al., 2014)
			Same steps as for crop coefficient, but in Eq. (2) weighted by fraction only
Manning's surface roughness coefficient for forest and other land cover type (<i>mannings_f</i> , <i>mannings_o</i>)	Roughness or friction applied to the flow by the surface on which water is flowing (averaged by ecosystem type)	CGLS-LC100 (discrete_classification = '111', '112', '113', '114', '115', '116', '121', '122', '123', '124', '125', '126' [forest types], '20', '30', '40', '60', '70', '90', '100' [other land cover types])	Same steps as for crop coefficient
		SPAM (spam2010v1r0_global_physical-area_CROP_i/r, 42 crops, 'i' – irrigated, 'r' – rainfed)	Same steps as for crop coefficient
		CHOW (Table 5, 6 – information on roughness coefficient n); Burek et al. (2014)	Matching roughness coefficient for each crop/ land cover type
			Same steps as for crop coefficient, but in Eq. (2) weighted by fraction only
Leaf area index for forest, irrigated crops and other land cover type (<i>laif</i> , <i>laih</i> , <i>laio</i>)	Defined as half the total area of green elements of the canopy per unit horizontal ground area m ² /m ² (10-day average; 36 fields in total)	CGLS-LAI 10-day average for 2010-2019; <i>fracforest</i> ; <i>fracirrigated</i> ; <i>fracother</i>	Upscaling to final temporal resolution (in total 36 LAI fields); Reprojecting and upscaling to final grid and spatial resolution with unweighted mean; Filtering sparse areas of relevant fractions $fr < 0.7$, where fr – fraction; NoData filling DEEP (upsampling to 1, 3, 15 arc min, 1, 3, 15, 60 degrees spatial resolution with unweighted mean; replacing NoData at final resolution with first available precomputed less coarser resolution, if not – with zero)
Rice planting day (<i>riceplantingday1</i> , <i>riceplantingday2</i> , <i>riceplantingday3</i>)	Most probable day of the year when rice is planted for the first, second and third time	RiceAtlas (PLANT_PKn, 3 seasons)	Ordering planting seasons by increasing Julian day (in total 3 planting dates per spatial unit); Shapefile gridding to final grid and spatial resolution (in total 3 fields); Note: if less than 3 seasons – repeating last available planting/ harvesting seasons date;
Rice harvest day (<i>riceharvestday1</i> , <i>riceharvestday2</i> , <i>riceharvestday3</i>)	Most probable day of the year when rice is harvested after planting for the first, second and third time	RiceAtlas (HARV_PKn, 3 seasons)	NoData filling with global unweighted mode date of first planting/ harvesting season (i.e. 105 – 15 th April/ 227 – 15 th August)
Root depth for forest and non-forest (<i>root_depth_f</i> , <i>root_depth_o</i>)	Deepest soil depth reached by the crop roots	CGLS-LC100 (discrete_classification = '111', '112', '113', '114', '115', '116', '121', '122', '123', '124', '125', '126' [forest types], '20', '30', '40', '60', '70', '90', '100' [other land cover types])	Same steps as for crop coefficient
		SPAM (spam2010v1r0_global_physical-area_CROP_i/r, 42 crops, 'i' – irrigated, 'r' – rainfed)	Same steps as for crop coefficient

		FAO56 (Table 22 – information on crop rooting depth); Burek et al. (2014)	Matching rooting depth for each crop/ land cover type
			Same steps as for crop coefficient, but in Eq. (2) weighted by fraction only; Downscaling to native SoilGrids250m resolution with nearest neighbour (for soil depth calculations)

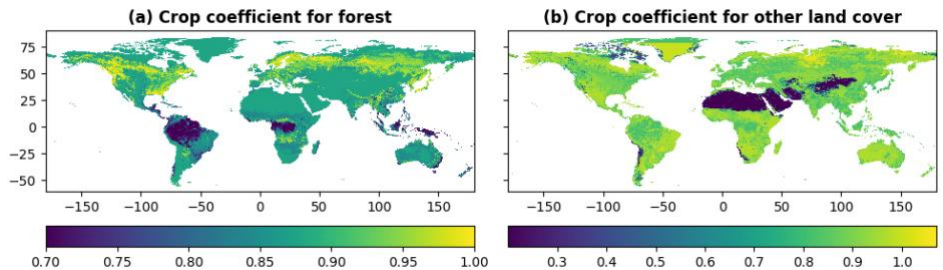
386
387
388
389
390
391
392
393
394
395
396
397
398

The final step of the crop coefficient, crop group number, Manning’s surface roughness coefficient, and additional crop height (for crop coefficient calculation) and root depth (for soil depth calculation, see Section 6.2) for forest, irrigated crops and other land cover type is to compute weighted average of their components (e.g. different forest types) following Eq. (2):

$$K = \frac{A_1 \cdot fr_1 \cdot K_1 + A_2 \cdot fr_2 \cdot K_2 + \dots + A_N \cdot fr_N \cdot K_N}{A_1 \cdot fr_1 + A_2 \cdot fr_2 + \dots + A_N \cdot fr_N} \quad (2)$$

where A is a scaling parameter (equals 1, except for crop coefficient where it equals to crop height), fr refers to the fraction of crop or land cover type, K – default (i.e. source table based) variable in question values, $1..N$ – number of crop or land cover types included in the field (i.e. for forest $N=12$, irrigated crops $N=41$, other land cover type $N=7$ and for CGLS-LC100 type ‘40’ (cropland) default values are based on 42 rainfed crops).

The generated vegetation property fields, e.g. crop coefficient for forest (see Figure 10a) and other land cover (see Figure 10b), follow main features of e.g. generated forest fraction.

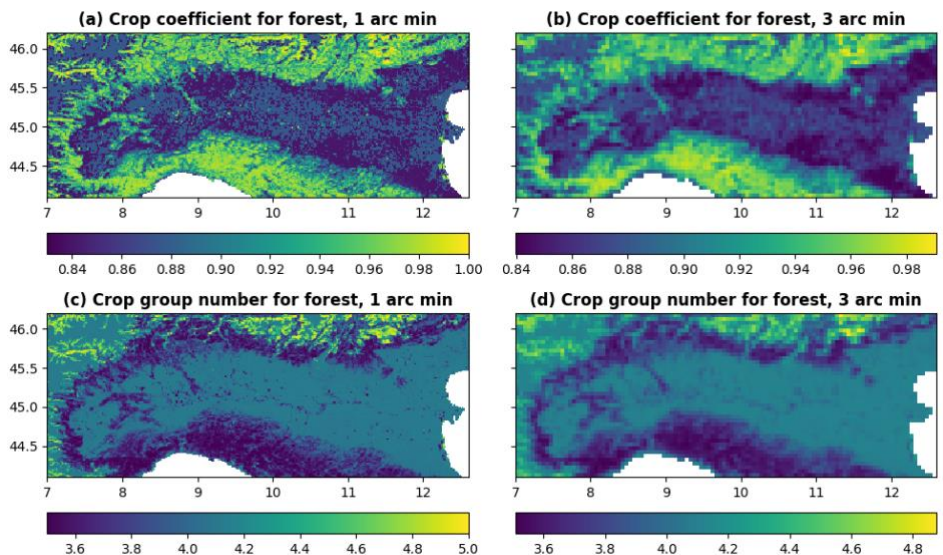


399
400
401

Figure 10. Crop coefficient for forest (left column, plot a) and crop coefficient for other land cover type (right column, plot b) at 3 arc min (~5.6 km at the equator) resolution for global region.

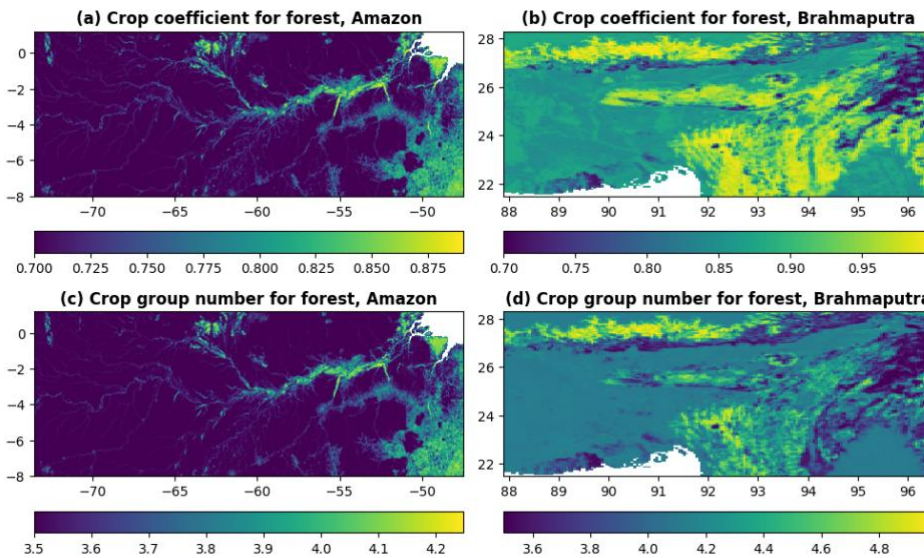
402 5.3 Regional examples

403 All fields in the vegetation properties category are complementary to the land use fractions, and help to understand
404 for example the difference in evaporation water intake. The fields easiest to interpret are the crop coefficient and
405 the crop group number which are presented for forest in Figure 11 for Po River area in 1 arc min and 3 arc min
406 resolution, and in Figure 12 for Amazon River and Brahmaputra River areas at 3 arc min resolution. For example,
407 fields of crop group number for forest (i.e. different forest type) show transition of vegetation resilience towards
408 dry conditions in the Brahmaputra River area.
409



410

411 Figure 11. Crop coefficient for forest (upper row, plots a and b) and crop group number for forest (lower row, plots c
 412 and d) at 1 arc min (~1.9 km at the equator, left column, plots a and c) and 3 arc min (~5.6 km at the equator, right
 413 column, plots b and d) resolution for Po River area in Italy.



414 Figure 12. Crop coefficient for forest (upper row, plots a and b) and crop group number for forest (lower row, plots c
 415 and d) at 3 arc min (~5.6 km at the equator) resolution for Amazon River area (left column, plots a and c) and
 416 Brahmaputra River area (right column, plots b and d).
 417

418 6 Soil properties

419 6.1 General information

420 In land surface and distributed hydrological models, the water movement, storage and plants' water-uptake from
 421 the soil are often described by the soil-/water retention curve (SWRC). The SWRC is derived empirically by
 422 measuring how water is retained and released by different soil types. Throughout time different SWRC have been
 423 developed and integrated into models, the most widely applied are Van Brooks and Corey (Brooks and Corey,
 424 1964), Fredlund and Xing (Fredlund and Xing, 1994), van Genuchten (van Genuchten, 1980), and Gardner
 425 (Gardner, 1956) SWRCs. Different SWRC equations require different parameters, some shared between different
 426 SWRC concepts, e.g. referring physical soil characteristics such as water saturated and unsaturated content,
 427 hydraulic conductivity and pore size, others uniquely describing the SWRC function shape, not directly related to
 428 soil properties. Often, for computational reasons, the soil profile from ground level to bedrock depth is sliced into
 429 layers, at the modeller's choice, and the SWRC function is applied to each soil layer. Alternative use of soil
 430 properties is for soil moisture calculations.

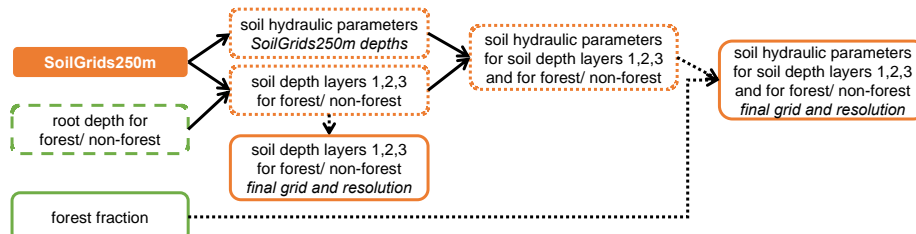
431 The dataset includes variables required to apply the Van Genuchten SWRC equations (van Genuchten, 1980) to
 432 describe the water dynamics through a vertical soil profile composed of three layers (1, 2, 3), each variable is
 433 required for each soil layer and for forest (_f) or non-forest (_o) land use, with different soil depth in forest (_f)
 434 and non-forest (_o) areas following root depth values from Allen et al. (1998), further referred as FAO56, (total
 435 of 29 variables; name in brackets in italics correspond to the field's name in the data repository):

- 436 • Soil profile: surface layer depth (*soildepth1_f*, *soildepth1_o*, mm), middle layer depth (*soildepth2_f*,
 437 *soildepth2_o*, mm), subsoil depth (*soildepth3_f*, *soildepth3_o*, mm);
- 438 • Soil hydraulic properties: saturated (*thetas1_f*, *thetas1_o*, *thetas2_f*, *thetas2_o*, *thetas3*, m³/m³) and
 439 residual (*thetar1*, *thetar2*, *thetar3*, m³/m³) volumetric soil moisture content, pore size index (*lambda1_f*,
 440 *lambda1_o*, *lambda2_f*, *lambda2_o*, *lambda3*, dimensionless), Van Genuchten equation parameter
 441 (*genua1_f*, *genua1_o*, *genua2_f*, *genua2_o*, *genua3*, cm⁻¹), saturated soil conductivity (*ksat1_f*, *ksat1_o*,
 442 *ksat2_f*, *ksat2_o*, *ksat3*, mm/day).

443 6.2 Reference data and methodology

444 Soil properties are derived from **The International Soil Reference and Information Centre (ISRIC)**
 445 **SoilGrids250m global gridded soil information release 2017** (further referred as SoilGrids250m) – an output
 446 of special predictions produced by the SoilGrids system, as a set of global soil property and class maps on soil

447 characteristics at six standard depths, including soil textures (clay, silt, sand), depth to bedrock, bulk density,
 448 organic carbon, pH and cation exchange capacity at 250 meters resolution covering land area with no permanent
 449 ice and representative for the year 2010 (for reference data details see Appendix 1); and are computed for both
 450 forested and non-forested (also known in literature as ‘others’) areas, expressed as fractions (main source is forest
 451 fraction based on CGLS-LC100, see Section **Error! Reference source not found.**), where non-forested area is
 452 the complementary fraction of forest. Soil depth layers are derived first and used as input to the soil hydraulic
 453 equations used to derive the properties, following a sequential workflow (see Figure 13 and Table 4). Equations
 454 used are from Toth et al. (2015).
 455



456
 457 **Figure 13. Workflow to generate the soil related fields; solid arrows indicate a function transformation, dotted –**
 458 **upscaling; dashed boxes indicate the intermediate fields used for other field generation, dotted – the fields only used**
 459 **for the soil-related fields; ‘SoilGrids250m depths’ – fields at the SoilGrids250m native grid and resolution with six**
 460 **default depths, ‘final grid and resolution’ – fields at the dataset’s final grid and resolution, boxes with no explicit**
 461 **indication – fields at SoilGrids250m native grid and resolution only.**

462 **Table 4. Soil property fields, their description, and applied transformations; name in brackets in italics next to each**
 463 **field correspond to the name in the data repository.**

<i>Field type</i>	<i>Description</i>	<i>Data Source</i>	<i>Transformation (in order)</i>
Soil depth layers 1, 2, 3 for forest and non-forest (<i>soildepth1_f, soildepth1_o, soildepth2_f, soildepth2_o, soildepth3_f, soildepth3_o</i>)	Root depths assumed to divide the total soil depth between topsoil (surface [layer 1] and middle [layer 2]) and subsoil (bottom [layer 3])	SoilGrids250m (<i>absolute_depth_to_bedrock; root_depth_f; root_depth_o</i>)	Transforming at SoilGrids250m native grid and resolution as described in Appendix 3 ‘Soil Depth’ (in total 3 forest and 3 non-forest soil depth layer fields); Reprojecting and upscaling to final grid and resolution with unweighted mean; NoData filling DEEP (upsampling to 1, 3, 15 arc min, 1, 3, 15, 60 degrees spatial resolution with unweighted mean; replacing NoData at final resolution with first available precomputed less coarser resolution, if not – with zero)
Saturated volumetric soil moisture content for soil depth layers 1, 2, 3, and for forest and non-forest (<i>thetas1_f, thetas1_o, thetas2_f, thetas2_o, thetas3</i>)	Saturated water content soil hydraulic property representing the maximum water content in the soil	SoilGrids250m (clay_content, silt_content, bulk_density); <i>soildepth1_f; soildepth1_o; soildepth2_f; soildepth2_o; soildepth3_f; soildepth3_o; fracforest</i>	Transforming at SoilGrids250m native grid and resolution as described in Appendix 3 ‘Soil hydraulic parameters’ (in total 5 fields per soil hydraulic parameter, except <i>thetar</i> – only 3 as no forest/ non-forest separation);
Residual volumetric soil moisture content for soil depth layers 1, 2, 3 (<i>thetar1, thetar2, thetar3</i>)	Residual water content soil hydraulic property representing the minimum water content in the soil	SoilGrids250m (clay_content, silt_content); <i>soildepth1_f; soildepth1_o; soildepth2_f; soildepth2_o; soildepth3_f; soildepth3_o; fracforest</i>	Limiting values and weighting by forest/ non-forest fraction (limits <i>thetas</i> < 1.0, <i>thetar</i> < <i>thetas</i> , <i>lambda</i> ≤ 0.42, <i>genua</i> ≤ 0.055, <i>ksat</i> > 0.0);
Pore size index for soil depth layers 1, 2, 3, and for forest and non-forest (<i>lambda1_f, lambda1_o, lambda2_f, lambda2_o, lambda3</i>)	Van Genuchten parameter λ (also referred as ‘n-1’ in literature) soil hydraulic property representing the pore size index of the soil	SoilGrids250m (clay_content, silt_content, bulk_density, organic_carbon_content); <i>soildepth1_f; soildepth1_o; soildepth2_f; soildepth2_o; soildepth3_f; soildepth3_o; fracforest</i>	Upscaling to final grid and resolution with unweighted mean; NoData filling DEEP (upsampling to 1, 3, 15 arc min spatial resolution with unweighted mean; replacing NoData at final resolution with first available

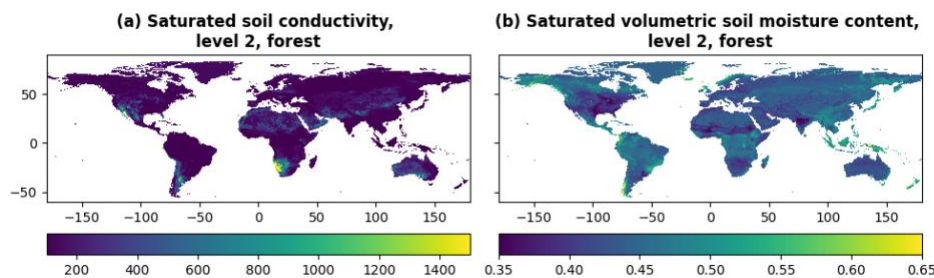
Van Genuchten equation parameter for soil depth layers 1, 2, 3, and for forest and non-forest (<i>genua1_f</i> , <i>genua1_o</i> , <i>genua2_f</i> , <i>genua2_o</i> , <i>genua3</i>)	Van Genuchten parameter α soil hydraulic property	SoilGrids250m (clay_content, silt_content, bulk_density, organic_carbon_content); <i>soildepth1_f</i> ; <i>soildepth1_o</i> ; <i>soildepth2_f</i> ; <i>soildepth2_o</i> ; <i>soildepth3_f</i> ; <i>soildepth3_o</i> ; <i>fracforest</i>	precomputed less coarser resolution, if not – with global unweighted mean)
Saturated soil conductivity for soil depth layers 1, 2, 3, and for forest and non-forest (<i>ksat1_f</i> , <i>ksat1_o</i> , <i>ksat2_f</i> , <i>ksat2_o</i> , <i>ksat3</i>)	Saturated hydraulic conductivity soil hydraulic property representing the ease with which water moves through pore spaces of the soil	SoilGrids250m (clay_content, silt_content, soil_pH, cation_exchange_capacity); <i>soildepth1_f</i> ; <i>soildepth1_o</i> ; <i>soildepth2_f</i> ; <i>soildepth2_o</i> ; <i>soildepth3_f</i> ; <i>soildepth3_o</i> ; <i>fracforest</i>	

464
465
466
467
468
469
470
471
472
473
474
475
476
477
478
479
480
481
482
483
484

Two of the most common soil parameters of land surface and hydrological models, saturated hydraulic conductivity *ksat* and saturated water content, are shown in Figure 14.

Saturated hydraulic conductivity *ksat* (see Figure 14a) ranges from 2 to 7445 mm/day. The highest *ksat* values are concentrated in desertic areas such as the Sahara, Arabian Peninsula, Gobi, Patagonian, Sonoran-Mojave and Kalahari and Namib deserts. Low *ksat* between, 2 and 18 mm/day, are found in the Amazon river basin, the lower Mississippi river basin and South East Asia. *ksat* was visually compared against 8 global datasets developed with different input data and/ or PTFs (Zhang and Schaap, 2019; Gupta et al., 2021); a general agreement is noticeable in areas that show low variability across all datasets. Northern Russia, Canada, South East Asia and Sonoran-Mojave Desert are the areas with high variability among datasets, with values ranging from very low to very high *ksat*. Source of uncertainties in *ksat* values are primarily due to little availability of soil samples and measurements carried out in those areas. Moreover, the climatic context plays a relevant role in clay mineralogy composition, organic composition and soil pores structure (Hodnett and Tomasella, 2002), which influence how water flows through the soil. Therefore, the PTF developed using soil samples collected in temperate areas (such as Europe) are expected to have a different hydraulic behaviour compared to those collected in tropical climates (Gupta et al., 2021), as also seen in Figure 14a.

Saturated water content (see Figure 14b) ranges between 0.27 to 0.79, with 80% of values between 0.40 and 0.46. A comparison with other global datasets was not carried out, however uncertainties are expected to be of the same order of magnitude than those of *ksat* given the fact the saturated water content is calculated using bulk density and clay content data.

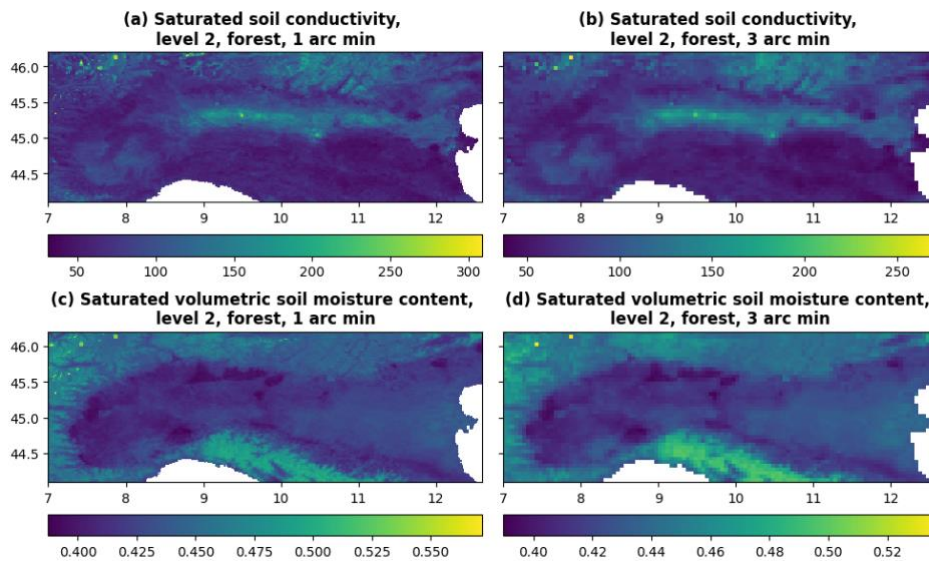


485
486
487
488

Figure 14. Saturated soil hydraulic conductivity for forested areas of soil depth layer 2 in mm per day (left column, plot a) and saturated volumetric soil moisture (i.e. water) content for forested areas of soil depth layer 2 (right column, plot b) at 3 arc min (~5.6 km at the equator) resolution for global region.

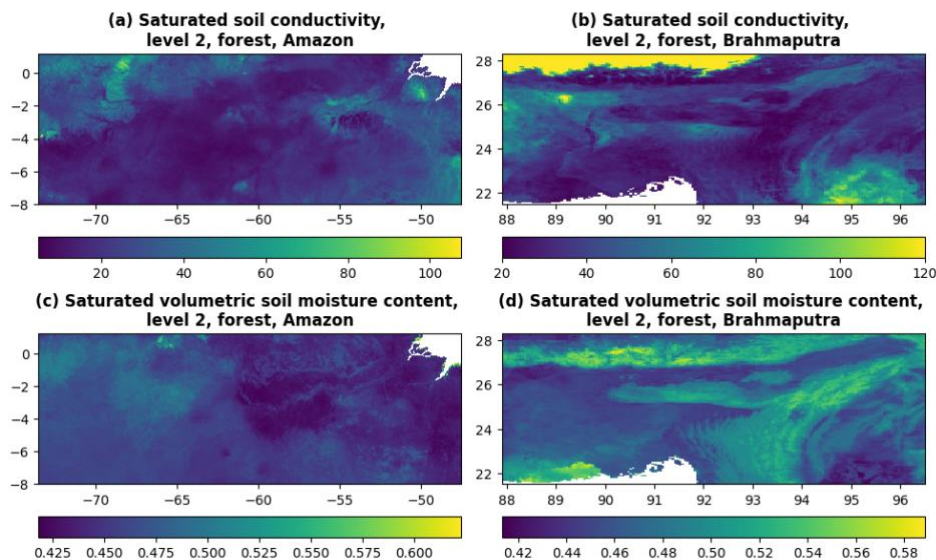
489 6.3 Regional examples

490 The majority of soil properties fields are easy to interpret. Saturated soil conductivity *ksat* and saturated volumetric
491 soil moisture content are presented for forested areas of soil depth layer 2 in Figure 15 for the Po River area in 1
492 arc min and 3 arc min resolution, and in Figure 16 for the Amazon River and the Brahmaputra River areas at 3
493 arc min resolution. The field of saturated soil conductivity for forest shows how easy it is for water to penetrate
494 soil depending on forest type, and the field of saturated volumetric soil moisture content shows what is the
495 maximum amount of water that the soil can absorb depending on forest type have interesting features over
496 Brahmaputra River area.
497



498
499
500
501
502

Figure 15. Saturated soil hydraulic conductivity for forested areas of soil depth layer 2 in mm per day (upper row, plots a and b) and saturated volumetric soil moisture (i.e. water) content for forested areas of soil depth layer 2 (lower row, plots c and d) at 1 arc min (~1.9 km at the equator, left column, plots a and c) and 3 arc min (~5.6 km at the equator, right column, plots b and d) resolution for Po River area in Italy.



503
504
505
506
507

Figure 16. Saturated soil hydraulic conductivity for forested areas of soil depth layer 2 in mm per day (upper row, plots a and b) and saturated volumetric soil moisture (i.e. water) content for forested areas of soil depth layer 2 (lower row, plots c and d) at 3 arc min (~5.6 km at the equator) resolution for Amazon River area (left column, plots a and c) and Brahmaputra River area (right column, plots b and d).

508 7 Lakes

509 7.1 General information

510 Lakes (and reservoirs) are important as they influence river discharge variability but also the atmosphere
511 regionally and globally. The area covered by lakes can be used for computing evaporation from open water,
512 freshwater storage, unregulated surface water extent, fresh water scarcity indexes, and biogenic green house gas
513 emission, as well as for reproducing different climate mitigation scenarios. The [CEMS_SurfaceFields_2022](#)
514 dataset only includes data on lake extent and not reservoirs (generally smaller), described as a lake mask where
515 the presence of lakes is consistent with fraction of inland water; the field's name in the data repository is *lakemask*,
516 dimensionless).

517 **7.2 Reference data and methodology**

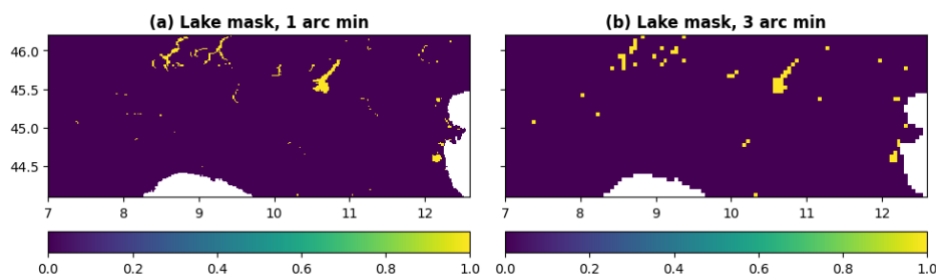
518 The lake mask field is derived from **The Global Lakes and Wetlands Database** (further referred as GLWD) – a
 519 global database of water bodies at spatial resolutions of up to 1:1 million – GLWD-1 with 3067 largest lake and
 520 654 largest reservoir polygons, and GLWD-2 with ~250000 smaller lake and reservoir polygons (see Table 7).

521
 522 **Table 5. Lake field, its description, data source and transformation; name in brackets in italics next to the lake field**
 523 **corresponds to the name in the data repository.**

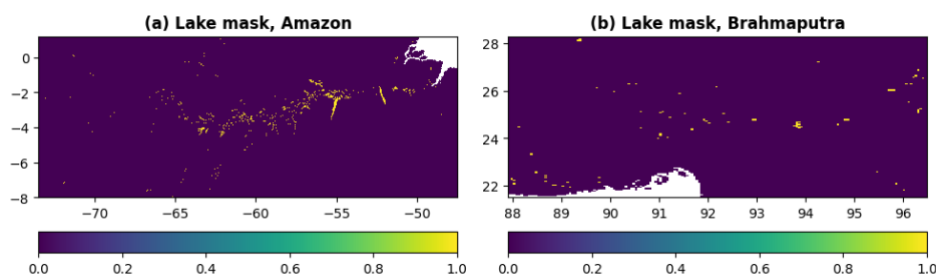
<i>Field type</i>	<i>Description</i>	<i>Data source</i>	<i>Transformation (in order)</i>
Lake mask (<i>lakemask</i>)	Area covered by lakes only (binary representation)	GLWD (GLWD-1, GLWD-2, lake type only); <i>fracwater</i>	Filtering non-lake spatial units; Shapefile gridding to final grid and resolution; If <i>fracwater</i> > 0 and GLWD is 'lake', then <i>lakemask</i> is 1, otherwise 0

524 **7.3 Regional examples**

525 The lake mask field is easy to interpret as it shows which grid cells from fraction of inland water field have lakes.
 526 The lake mask field is presented in Figure 17 for Po River area in 1 arc min and 3 arc min resolution, and in Figure
 527 18 for Amazon River and Brahmaputra River areas at 3 arc min resolution, where it shows the abundance of lakes
 528 over Amazon River area and detailed lake shapes over Po River area described by the 1 arc min resolution field.
 529



530
 531 **Figure 17. Lake mask at 1 arc min (~1.9 km at the equator, left column, plot a) and 3 arc min (~5.6 km at the equator,**
 532 **right column, plot b) resolution for Po River area in Italy.**



533
 534 **Figure 18. Lake mask at 3 arc min (~5.6 km at the equator) resolution for Amazon River area (left column, plot a) and**
 535 **Brahmaputra River area (right column, plot b).**

536 **8 Water demand**

537 **8.1 General information**

538 Some environmental models explicitly represent a number of the human interventions impacting on the water
 539 cycle. One of the most common is water demand, which represents the withdrawal of water from natural water
 540 sources (e.g. rivers, reservoirs, groundwater) to satisfy the water demand for anthropogenic use. The segregation
 541 of the total water demand for anthropogenic use into four main sectors, namely domestic, energy, industrial, and
 542 livestock water withdrawal, enables a more accurate representation of the processes, and follows the Food and
 543 Agriculture Organisation of the United Nations (FAO) terminology (Kohli et al., 2012). Domestic water
 544 withdrawal represents indoor and outdoor household water use as well as other uses (e.g. industrial and urban
 545 agriculture) connected to the municipal system (e.g., water use by shops, schools, and public buildings). Electricity
 546 (energy) water withdrawal is the water use for the cooling of thermoelectric and nuclear power plants. Water
 547 withdrawal for industry is the water used for fabricating, processing, washing, cooling or transporting products,

548 also includes water within the final products and water used for sanitation within the manufacturing facility.
549 Livestock withdrawal is the demand for drinking and cleaning purposes of livestock.
550 Higher accuracy in environmental modelling is achieved by differentiating water demand sources and by
551 allocating different levels of priority to different usages. Within LISFLOOD, for instance, water demand for the
552 energy sector and flooded irrigation (rice crops) is supplied by surface water bodies only, while non-flooded
553 irrigation, domestic, industrial, livestock water demand can be supplied by both groundwater and surface water
554 bodies. Moreover, domestic water demand has the highest priority in case of water scarcity conditions.
555 It must be noted that the fields of water demand for agriculture are not included in this dataset because LISFLOOD
556 computes crops water demand internally by accounting for climatic conditions, information on land cover (see
557 Section 4.2), crops properties (see Section 5.2), and soil properties (see Section 6.2). Conversely, fields
558 representing the volume of water to satisfy the domestic, energy, industrial, and livestock demand must be
559 provided as input. Domestic, industrial, energy, and livestock water demand volumes have seasonal (e.g. due to
560 temperature differences) and inter-annual variations (e.g. due to population changes and different economic
561 conditions). In order to account for this variability, in LISFLOOD the four sectoral water demand fields provide
562 daily water demand data with monthly or annual variability from 01.01.1979 to 31.12.2019: the water demand
563 values are provided in mm/day, one field per month (the first day of each month is used as representative
564 timestamp for the entire month) for domestic and energy demand, one value per year (the monthly fields are
565 repeated twelve times per each year) for industrial and livestock demand.
566 Water availability, ecosystem long term ecological status, and anthropogenic needs must be accounted for to
567 evaluate the long term sustainability of water withdrawals. However, the spatial scales of water use data and
568 available water resources data often do not match due to different ways of data surveying and/or modelling
569 (McManamay et al., 2021; Zhang et al., 2023) and this creates a technical hurdle. Alternative use of the gridded
570 sectoral water demand information is e.g. for (i) the statistical analysis of long term spatiotemporal patterns and
571 trends of water demand; (ii) the evaluation of the long term sustainability and impacts of water withdrawals (e.g.
572 in connection to remote sensing-derived datasets of surface water extent or groundwater total storage); (iii) the
573 analysis of ecosystem–water–food–energy nexus (Karabulut et al., 2016); (iv) the evaluation of the impacts on
574 water resources of economical and price policies (Dolan et al., 2021); (v) the analysis of the responses in sectoral
575 water use during hydro climatic extremes (Belleza et al., 2023).
576 The CEMS_SurfaceFields_2022 dataset includes water demand for four main sectors (note that each sector
577 consists in total of 12 daily water demand fields per 41 (1979-2019) years, so 492 fields per sector) for (name in
578 brackets in italics correspond to the field's name in the data repository): livestock (*liv*, mm/day), industry (*ind*,
579 mm/day), energy production, (*ene*, mm/day) and domestic use (*dom*, mm/day). The temporal extension of the
580 water demand fields presented in this manuscript includes the most recent information of water demand at the
581 time of the dataset's preparation. Readers that are interested in using more recent water demand data are invited
582 to follow the protocol presented in Section 8.2 to further extend in time the provided fields.

583 8.2 Reference data and methodology

584 Global gridded water demand fields with monthly variability were generated for the four sectors using the data
585 sources listed here and following the transformations summarised in Table 8 (for additional information and extra
586 details see GitHub repository 'lisflood-utilities/src/lisfloodutilities/water-demand-historic at master · ec-
587 jrc/lisflood-utilities · GitHub', last accessed: 21.01.2024): (i) **AQUASTAT** – the FAO's global information
588 system with yearly country data on water resources and agricultural water management for "Gross Domestic
589 Product (GDP)", "Industry, value added to GDP", "Agricultural water withdrawal", "Industrial water withdrawal",
590 "Municipal water withdrawal", "Total water withdrawal", and "Irrigation water withdrawal"; (ii) **United States
591 Geological Survey National Water Information System** (further referred as USGS NWIS) – a United States
592 (US) database on water use data for the annual state statistics for "Domestic total self-supplied withdrawals, fresh,
593 in Mgal/d", "Public Supply total self-supplied withdrawals, fresh, in Mgal/d", "Industrial total self-supplied
594 withdrawals, fresh, in Mgal/d", "Total Thermoelectric Power total self-supplied withdrawals, fresh, in Mgal/d",
595 "Total Thermoelectric Power power generated, in gigawatt-hours", and "Livestock total self-supplied
596 withdrawals, fresh, in Mgal/d"; (iii) **Global Change Analysis Model** (further referred as GCAM) – an integrated,
597 multi-sector model's output that provides estimates on water withdrawals for energy, agriculture, and municipal
598 uses as lumped values of 235 hydrologic basins; (iv) **Global-scale gridded estimates of thermoelectric power
599 and manufacturing water use** (further referred as Vassolo and Doll, 2005) – a global-scale gridded on 0.5° by
600 0.5° grid estimate of water withdrawal for cooling of thermal power stations and for manufacturing, representative
601 for the year 1995; (v) **The Gridded Livestock of the World (GLW) version3** (further referred as GLW3) – a
602 global-scale gridded on 0.083333° by 0.083333° (~10 km at the equator) grid of eight livestock species
603 distribution, representative for the year 2010; (vi) **World Bank manufacturing value added and gross domestic
604 product** (further referred as World Bank) – data provide "Manufacturing, value added (constant 2015 US\$)"
605 values (further referred as MVA) and "Gross Domestic Product GDP (constant 2015 US\$)" values; (vii) **The**

606 **Global Human Settlement Population Grid multitemporal version R2019A** (further referred as GHS-POP) –
607 a global-scale gridded on 9 arc sec (~300 m at the equator) grid distribution of population, expressed as the number
608 of people per grid cell, representative for the years 1975, 1990, 2000 and 2015; (viii) **Thematic Mapping**
609 **Country Borders** shapefile (further referred as TM ‘country borders’) – world country borders dataset; (ix) **The**
610 **United States Census Bureau** Cartographic Boundary Files – Shapefile (further referred as US CB) – the State
611 boundaries for the USA, representative for the year 2018; (x) **Multi-Source Weather** (further referred as MSWX)
612 – a global-scale gridded high-resolution (3-hourly, 0.1°), bias-corrected meteorological product with 2-meter daily
613 and monthly maximum and minimum air temperature; (xi) **Huang et al. (2018)** – a publication presenting 0.5°
614 resolution global monthly gridded sectoral water withdrawal dataset for the period 1971–2010 with calibrated R
615 coefficient values and technique for temporal downscaling of domestic and energy water demands.
616 The water demand values are provided in mm/day, one field per month from 01.01.1979 to 31.12.2019 (the first
617 day of each month is used as the representative timestamp for the entire month). The methodology applied largely
618 follows Huang et al. (2018), with the key differences being the use of freely available datasets and the higher
619 resolution of the resulting fields. Spatial downscaling was achieved following the approach of Hejazi et al. (2014);
620 temporal downscaling was performed following the approaches of Wada et al. (2011), Voisin et al. (2013) and
621 Huang et al. (2018). It should be noted that country-scale estimates (from AQUASTAT) were integrated with
622 state-level water withdrawal estimates (from USGS NWIS). The protocol for the integration of local information
623 with global data sources was developed for further use in the future, to enable the integration of other regional or
624 national datasets as soon as they become available.

625 **Table 6. Water demand fields, their description, data source and applied transformations; cells with bold italics show**
626 **required intermediate fields; name in brackets in italics next to each field correspond to the name in the data repository.**
627

<i>Field type</i>	<i>Description</i>	<i>Data source</i>	<i>Transformations (in order)</i>
<i>Population density (pop)</i>	Number of people per grid cell	GHS-POP R2019A (1975, 1990, 2000, 2015)	Reprojecting and upscaling from native (9 arc sec) to the final grid and intermediate resolution of 0.01°x0.01° with sum (in total four fields); Transforming from population number to density per grid cell (i.e. dividing by grid cell area) and upscaling from intermediate to final resolution with mean (in total four fields); NoData filling (year) with linear interpolation till 2015, and with years 2000 and 2015 trend extrapolation 2016 onwards (pop_{year}^{grid} ; in total 41 fields)
		TM ‘country borders’, US CB ‘state borders’	Shapefile (country, US State) gridding to final grid and intermediate resolution of 0.01°x0.01°, then to final resolution; Transforming from population density per grid cell to population per country (i.e. multiplying by grid cell area and summing grid cells according to the country mask from step above; $pop_{year}^{country}$; in total one table)
Water demand for domestic use (<i>dom</i>)	Daily supply of water volume for indoor and outdoor household purposes and for all the uses that are connected to the municipal system (e.g., water used by shops, schools, and public buildings)	AQUASTAT (per country), USGS NWIS (per US State), <i>pop</i>	Unit conversion from native to km ³ /year; NoData filling (year): for countries – with linear interpolation and forward/ backward extrapolation based on $pop_{year}^{country}$, for US states – with linear interpolation and nearest neighbour extrapolation ($demand_{year}^{country}$, in total one table)
		<i>pop</i> , TM ‘country borders’, US CB ‘state borders’	Transforming water demand ($demand_{year}^{country}$) to water demand per capita per country/ US State per year (in total one table): $perCapitaDemand_{year}^{country} = \frac{demand_{year}^{country}}{pop_{year}^{country}}$; NoData filling (country) with nearest neighbour; Transforming from water demand per capita to water demand per grid cell (i.e. weighting by pop_{year}^{grid} , in total one field per year): $demand_{year}^{grid} = perCapitaDemand_{year}^{country} \cdot pop_{year}^{grid}$
		MSWX, Huang et al. (2018) [Table 3, Eq. (2)].	Temporal downscaling (month) to account for the withdrawal fluctuations between the warmest and coldest months based on Huang et al. (2018) Eq. (2) (in total 12 fields per year): $demand_{month,year}^{grid} = \frac{demand_{year}^{grid}}{month_{number}} \cdot \left(\frac{\bar{T}_{month,year}^{grid} - avg\bar{T}_{year}^{grid}}{max\bar{T}_{year}^{grid} - min\bar{T}_{year}^{grid}} \cdot R + 1 \right)$, where $avg\bar{T}_{year}^{grid}$, $max\bar{T}_{year}^{grid}$, $min\bar{T}_{year}^{grid}$ are the average, maximum, minimum monthly temperatures in a year; $\bar{T}_{month,year}^{grid}$ is the average temperature in a month of the year; R is the amplitude of the monthly fluctuations from Huang et al.

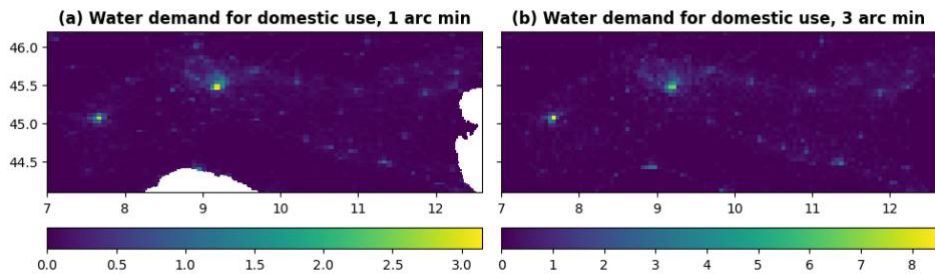
			(2018) [Table 3]; $month_{year}^{number}$ is number of months in a year, i.e. 12; Temporal downscaling (day; in total 12 fields per year): $demand_{day,month,year}^{grid} = \frac{demand_{month,year}^{grid}}{day_{month}^{number}}$, where day_{month}^{number} is number of days in a month of a certain year
Water demand for industrial use (<i>ind</i>)	Daily supply of water volume for fabricating, processing, washing and sanitation, cooling or transporting a product, incorporating water into a product	AQUASTAT (per country), USGS NWIS (per US State), GCAM (per region), Vassolo and Doll (2005), World Bank (MVA), <i>pop</i> , TM ‘country borders’	Unit conversion from native to km ³ /year; NoData filling (year; in total one table): <ul style="list-style-type: none"> regional data – downscaling (spatial) to country values (i.e. weighting by $pop_{year}^{country}$), then linear interpolation (between years) and nearest neighbour extrapolation in time, finally rescaling values according to Vassolo and Doll (2005); country data – with linear interpolation (between years) and forward/ backward extrapolation based on <i>MVA</i> or $pop_{year}^{country}$, value disaggregation from industrial water demand to manufacturing and thermoelectric water demands according to regional data results; for US States data – with linear interpolation (between years) and nearest neighbour extrapolation; mosaicking results from US States and country data, from regional data, if not – with zero
		<i>pop</i> , TM ‘country borders’, US CB ‘state borders’	Transforming from water demand per country/ US State to per grid cell (i.e. weighting by $pop_{year}^{grid}/pop_{year}^{country}$; in total one field per year): $demand_{year}^{grid} = \frac{demand_{year}^{country}}{pop_{year}^{country}} \cdot pop_{year}^{grid}$, Temporal downscaling (day; in total one field per year): $demand_{day,year}^{grid} = \frac{demand_{year}^{grid}}{day_{year}^{number}}$, where day_{year}^{number} is number of days in a year
Water demand for thermoelectric use (<i>ene</i>)	Daily supply of water volume for the cooling of thermoelectric and nuclear power plants	AQUASTAT (per country), USGS NWIS (per US State), GCAM (per region), Vassolo and Doll (2005), World Bank (MVA), <i>pop</i> , TM ‘country borders’	Same steps as for water demand for industrial use, but using the energy withdrawals as input data (in total one table)
		<i>pop</i> , TM ‘country borders’, US CB ‘state borders’	Same steps as for water demand for industrial use (in total one field per year)
		GCAM (per region), MSWX, Huang et al. (2018) [Eq. (3)-(10)].	Temporal downscaling (month) to account for the withdrawal fluctuations between the warmest and coldest months based on Huang et al. (2018) Eq. (3)-(10) (in total 12 fields per year)
Water demand for livestock use (<i>liv</i>)	Daily supply of water volume for domestic animal needs	AQUASTAT (per country), USGS NWIS (per US State), GCAM (per region), GLW3, TM ‘country borders’	Unit conversion from native to km ³ /year; NoData filling (year; in total one table): <ul style="list-style-type: none"> regional data – spatial downscaling from regional withdrawals to country values (i.e. weighting by total livestock mass estimates per country from GLW3, $livestock_{year}^{country}$): $demand_{year}^{country} = \frac{withdrawal_{year}^{region}}{livestock_{year}^{region}} \cdot livestock_{year}^{country}$, then value linear interpolation (between years) and nearest neighbour extrapolation, finally rescaled with country data (if available) for US States data – with linear interpolation (between years) and nearest neighbour extrapolation; mosaicking results from US States and regional data, if not – with zero
		GLW3, TM ‘country borders’, US CB ‘state borders’	Transforming from water demand per country/ US State to per grid cell (i.e. weighting by $\frac{livestockDensity_{year}^{grid}}{livestockDensity_{year}^{country}}$; in total one field per year):

			$demand_{year}^{grid} = \frac{demand_{year}^{country}}{livestockDensity_{year}^{country}} \cdot livestockDensity_{year}^{grid};$ Temporal downscaling (day; in total one field per year): $demand_{day,year}^{grid} = \frac{demand_{year}^{grid}}{day_{year}^{number}},$ where day_{year}^{number} is number of days in a year
--	--	--	---

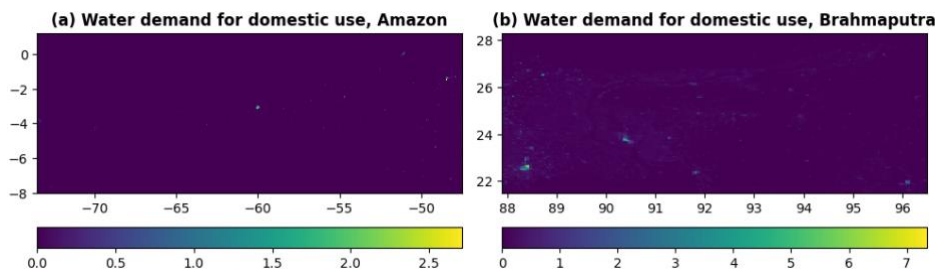
628 To the best of the authors' knowledge, no other publicly accessible temporally varying global water demand field
 629 set exists (only static datasets). A rigorous validation of the temporally varying water demand fields is not
 630 straightforward at the global scale, as the only comprehensive global data source, FAO AQUASTAT, was used
 631 to create the fields.

632 8.3 Regional examples

633 In general fields in water demand category are easy to interpret as they show how much water per day is needed
 634 to satisfy certain type of human induced needs. In reality water demand fields are mainly covering urbanised areas
 635 and are scattered around (i.e. not continuously looking field), with relatively small variations in field values from
 636 month to month. Example for domestic water use is presented for August 2018 in Figure 19 for Po River area in Italy
 637 at 1 arc min and 3 arc min resolution, and in Figure 20 for Amazon River and Brahmaputra River areas at 3 arc min
 638 resolution.
 639



640
 641 **Figure 19.** Water demand for domestic use in mm per day at 1 arc min (~1.9 km at the equator, left column, plot a) and
 642 3 arc min (~5.6 km at the equator, right column, plot b) resolution for Po River area in Italy.



643
 644 **Figure 20.** Water demand for domestic use in mm per day at 3 arc min (~5.6 km at the equator) resolution for Amazon
 645 River area (left column, plot a) and Brahmaputra River area (right column, plot b).

646 9 Data, access, licensing, documentation

647 The new CEMS_SurfaceFields_2022 is an open-source dataset of the Copernicus Emergency Management
 648 Service describing key components of the Earth surface generally required in environmental and hydrological
 649 modelling, including Earth system modelling and numerical weather prediction. The dataset includes static fields
 650 (e.g. forest fraction), yearly cycle fields (e.g. 10-day average LAI, in total 36 fields), and yearly varying fields
 651 (e.g. water demand). The surface fields are based on 25 different sources, including global and regional high
 652 resolution (up to 100 m) gridded and vector datasets. They were processed into two set of fields (i) at 1 arc min
 653 resolution (~1.86 km at the equator) over Europe (72.25 N/ 22.75 N, 25.25 W/ 50.25 E; 4530x2970 grid cells),
 654 and (ii) at 3 arc min resolution (~5.57 km at the equator) over the Globe (90.00 N/ 90.00 S, 180.00 W/ 180.00 E;
 655 7200x3600 grid cells), to provide an up-to-date surface state for six main field groups: (1) catchment morphology
 656 and river network, (2) land use fields, (3) vegetation properties, (4) soil properties, (5) lakes, (6) water demand.
 657 The CEMS_SurfaceFields_2022 dataset consist in total of 140 gridded fields at EPSG:4326 – WGS84: World
 658 Geodetic System projection in NetCDF format with information on Earth's surface state (see Table 9 for the full
 659 list of fields), which are grouped thematically in sub-folders. The 1 arc min European fields have a total volume

660 of 9.3 GB and the 3 arc min global fields have a total volume of 22.7 GB. The CEMS_SurfaceFields_2022 dataset
661 is freely available for download from the JRC Data Catalogue (<https://data.jrc.ec.europa.eu/>). The set of global
662 surface fields at 3 arc min resolution can be found here (JRC Data Catalogue – LISFLOOD static and parameter
663 maps for GloFAS – European Commission (europa.eu), <https://data.jrc.ec.europa.eu/dataset/68050d73-9c06-499c-a441-dc5053cb0c86>) and the set of surface fields for the European domain at 1 arc min resolution can be
664 found here (JRC Data Catalogue – LISFLOOD static and parameter maps for Europe – European Commission
665 (europa.eu), <https://data.jrc.ec.europa.eu/dataset/f572c443-7466-4adf-87aa-c0847a169f23>). The README.txt
666 file that can be found there contains the basic description of each surface fields including general information,
667 data description, file overview, methodological information and data access and sharing information (for detailed
668 technical description of how the surface fields were generated refer to the LISFLOOD User Guide, available
669 online: https://ec-jrc.github.io/lisflood-code/4_Static-Maps-introduction/). The changelog.txt file – provides users
670 with information on updates to the datasets. The copyright.txt file – information about the data license (CC BY
671 4.0).

672
673 **Table 9. Full list of surface fields with short description and units included in CEMS_SurfaceFields_2022 dataset; name**
674 **in italics correspond to the field’s file name in the data repository.**
675

<i>Field group</i>	<i>Description</i>	<i>Name</i>	<i>Units</i>
Main	model’s field (i.e. in technical for model operation/ running sense)	<i>mask</i>	dimensionless
Catchment morphology and river network	local drainage direction (i.e. flow direction from one cell to another)	<i>LDD</i>	dimensionless
	grid cell area	<i>pixarea</i>	m ²
	grid cell length	<i>pixlength</i>	m
	upstream drainage area	<i>upArea</i>	m ²
	standard deviation of elevation	<i>elvstd</i>	m
	gradient	<i>gradient</i>	m/m
	channel bottom width	<i>chanbw</i>	m
	channel length	<i>chanlength</i>	m
	channel gradient	<i>changrad</i>	m/m
	Manning’s roughness coefficient for channels	<i>chanman</i>	s/m ^{1/3}
	channel mask (i.e. presence of river channel)	<i>chan</i>	dimensionless
	channel side slope (i.e. channel’s horizontal distance divided by vertical distance)	<i>chans</i>	m/m
	bankfull channel depth	<i>chanbnkf</i>	m
channel floodplain (i.e. width of the area where the surplus of water is distributed when the water level in the channel exceed the channel depth)	<i>chanflpn</i>	m	
Land use fields	fraction of forest	<i>fracforest</i>	dimensionless
	fraction of sealed surface	<i>fracsealed</i>	dimensionless
	fraction of inland water	<i>fracwater</i>	dimensionless
	fraction of irrigated crops	<i>fracirrigated</i>	dimensionless
	fraction of rice	<i>fracrice</i>	dimensionless
fraction of other cover types	<i>fracother</i>	dimensionless	
Vegetation properties (for forest [f], irrigated crops [i], other land cover types [o])	crop coefficient	<i>cropcoef_f, cropcoef_i, cropcoef_o</i>	dimensionless
	crop group number	<i>cropgrp_f, cropgrp_i, cropgrp_o</i>	dimensionless
	Manning’s surface roughness coefficient	<i>mannings_f, mannings_o,</i>	s/m ^{1/3}
	rice planting days (3 seasons)	<i>riceplantingday1, riceplantingday2, riceplantingday3</i>	calendar day number
	rice harvesting days (3 seasons)	<i>riceharvestday1, riceharvestday2, riceharvestday3</i>	calendar day number
leaf area index	<i>laif, laii, laio</i>	m ² /m ²	
Soil properties (for [1, 2, 3] layers; for forest [f], non-forest [o])	surface layer depth	<i>soildepth1_f, soildepth1_o</i>	mm
	middle layer depth	<i>soildepth2_f, soildepth2_o,</i>	mm
	subsoil depth	<i>soildepth3_f, soildepth3_o</i>	mm
	saturated volumetric soil moisture content	<i>thetas1_f, thetas1_o, thetas2_f, thetas2_o, thetas3</i>	m ³ /m ³
	residual volumetric soil moisture content	<i>thetar1, thetar2, thetar3</i>	m ³ /m ³
	pore size index	<i>lambda1_f, lambda1_o, lambda2_f, lambda2_o, lambda3</i>	dimensionless
	Van Genuchten equation parameter	<i>genua1_f, genua1_o, genua2_f, genua2_o, genua3</i>	cm ⁻¹

	saturated soil conductivity	<i>ksat1_f, ksat1_o, ksat2_f, ksat2_o, ksat3</i>	mm/day
Lakes	lake mask (i.e. presence of lakes)	<i>lakemask</i>	dimensionless
Water demand	livestock	<i>liv</i>	mm/day
	industry	<i>ind</i>	mm/day
	thermoelectric production	<i>ene</i>	mm/day
	domestic use	<i>dom</i>	mm/day

676
677
678
679
680
681
682

Whilst the CEMS_SurfaceFields_2022 dataset followed strict requirements of the LISFLOOD-OS model (e.g. format, treatment of missing values, number of soil layers, etc...) it definitely can be used outside the LISFLOOD context, using the full dataset or its parts, for applications such as modelling risk assessment. The workflow and methodology used to generate the dataset and published in this manuscript can be used as reference and be easily modified if further adaptation to the dataset is needed (e.g. using different set of equations to describe the soil properties, or sourcing new/ more relevant local datasets).

683 10 Conclusion

684 The Earth's surface has a strong impact on the surface energy and water balance that drives lower atmosphere
685 weather conditions and river discharge fluctuations. Depending on the surface type (e.g. land use, terrain or soil),
686 weather in the region can be colder/ warmer, more/ less humid, drier/ rainier, and/ or calmer/ windier than its
687 surroundings, and the terrestrial water cycle can differ, with water infiltrating more/ less in the soil, leaving as
688 evaporation in a larger/ smaller rate, and reaching rivers faster/ slower. Surface information is provided by land
689 use and ecosystem type (e.g., forest, rice paddy, bare ground, urban), river geometry (e.g., channel width, channel
690 length), soil properties (e.g., depth, porosity, hydraulic properties), amongst others.

691 Information of underlying surface fields can be accounted for in Earth system and environmental models (e.g.
692 atmospheric, hydrological, etc.) to simulate the evolution in space and time of water, energy and carbon cycles. If
693 artificial influences and human intervention are included within the modelled processes (e.g. irrigation or water
694 management through reservoirs), the information required to describe the processes must also be integrated within
695 the modelling framework. Generally, this is achieved through a set of independent files used as input to the models.
696 Because of the temporal non-stationarity of some surface fields, typically associated with human intervention such
697 as land use and water use, but also due to climatic variation such as lake extent (new lakes forming or lakes
698 shrinking), input surface fields must be as representative as possible to the simulated period of interest. For
699 medium-range forecasting systems, this should be as close from present as possible, for example. When simulating
700 long periods, especially looking at past or future decades, caution must be given to results especially if some
701 surface fields which have substantially changed during the simulation period do not explicitly incorporate time
702 and instead are based on the most recent period, as they may not be representative to the full study period and can
703 introduce substantial biases that grow with time. Same is applicable if surface fields are used for collecting
704 statistical data in general, as stats based on stationary fields represent only the period used to generate stationary
705 field in question.

706 In addition, in recent years the horizontal resolution of global Earth system and environmental models has been
707 constantly increasing reaching the kilometre scale milestone, supported by the technological developments in the
708 field of High Performance Computers and the wealth of high resolution datasets freely available. This imposes
709 another condition to the input surface fields – it has to be of rather high horizontal resolution (i.e. ~2 and 6 km at
710 the equator).

711 Thanks to the availability of a wide range of high resolution environmental data derived from the use of ground,
712 unconventional and satellite measurement sensors, new high resolution datasets describing the Earth's surface are
713 nowadays released regularly. Even though each dataset may have a very low absolute and root mean square errors
714 compared against available independent data, merging different datasets for modelling purposes (e.g. to model
715 hydrological surface parameters) might lead to questionable results and even model crash, due to possible
716 discontinuity or inconsistency in the combined datasets. In the specific case of hydrological modelling where river
717 flow is also represented, high horizontal resolution does not guarantee better modelling per se. Sources of
718 potentially large errors can be easily hidden in high resolution datasets. This is the case for instance of errors in
719 the Digital Elevation Models when they are used to obtain the rivers drainage network. Small errors in the
720 elevation of a grid cell can lead to a totally inaccurate representation of the location and the direction in which the
721 river is flowing in the model compared to reality. Mislocating a river or having a slightly inaccurate catchment
722 area can represent a trivial inaccuracy for most applications, but it can also lead to missed flood warning for
723 thousands of people within a flood awareness system. To benefit from different recent high resolution datasets
724 based on satellite and ground measurements, it is essential that a well-defined, thorough workflow is designed and

725 implemented so that the final products are consistent and compatible with each other, and can be used in
726 combination.

727 The work presented in this manuscript is focused not only on the final surface field set generation (i.e.
728 CEMS_SurfaceFields_2022), but also on deriving robust reproducible methodology that could be re-applied once
729 new versions of 25 or less input sources are released. Understanding of the methodology applied helps to interpret
730 values in the final surface fields and possibly even numerical model results that use these surface fields. The
731 collection of input sources and their preparation for actual use is a very important step as it includes going through
732 all technical documentation, comparison and verification of papers, and investigation of the actual data, as well
733 as data gridding, interpolation, and scaling. All input sources for CEMS_SurfaceFields_2022 are ranked according
734 to their quality and up-to-date in order to favour one value in ambiguous situations when several datasets provide
735 different information for the same location. Consistency check between all surface type fractions is carried out to
736 address that ambiguity during the merge of information of different origin (i.e. adjust fractions to sum to one in
737 each grid cell). Some fields, like forest fraction, were rather straightforward to create from available source, yet it
738 was noted that prior correction of the source was needed to delete erroneous forest grid cells from the Fox Basin
739 in Canada (the mismatch was only spotted during the investigation of the actual data, as it was absent from the
740 documentation). Other fields, like soil hydraulic properties, are created not only from the source information but
741 also from the forest fraction that had to be generated prior; the soil hydraulic property methodology also includes
742 several steps that have to be performed at the data native resolution (i.e. 250 m) using information from several
743 global fields simultaneously which becomes technically and computationally challenging. Surface fields with
744 clear multi-annual changes, like water demand maps, are created using temporal interpolation and extrapolation
745 from multiple data sources to create time series fields. A final and non-trivial task is to have all resulting fields on
746 the identical required grid without deterioration of the actual value precision, even after several file type
747 translations (e.g. local drainage direction field can be automatically checked and corrected if needed for required
748 boundaries only in PCRaster format, not NetCDF). Due to the number of data sources and surface fields required
749 to represent the main variables (i.e. 70) used in Earth system and environmental models, the overall effort to
750 generate the CEMS_SurfaceFields_2022 dataset (both human and computing resources) was substantial.

751 The CEMS_SurfaceFields_2022 dataset is a new data source open to all offering a kilometre-scale resolution of
752 high-quality data describing the Earth's surface (openly available online from the data catalogue of the JRC for
753 Europe at ~1.9 km at the equator or 1 arc min resolution: <https://data.jrc.ec.europa.eu/dataset/f572c443-7466-4adf-87aa-c0847a169f23>,
754 and for Globe at ~5.6 km at the equator or 3 arc min resolution:
755 <https://data.jrc.ec.europa.eu/dataset/68050d73-9c06-499c-a441-dc5053cb0c86>, last accessed: 21.01.2024),
756 providing exceptional opportunity for the research and scientific community to extend and multiply European and
757 global applications in wide ranging fields of the water-energy-food nexus. The CEMS_SurfaceFields_2022
758 surface fields use can be vast, e.g. standard deviation of elevation and other orographic sub-grid parameters are
759 critical for radiation parametrization, especially for shadowing effect; channel geometry fields are vital to describe
760 overbank inundation and infer inundated areas in wetland methane and soil carbon modelling; land use fractions
761 are needed for skin temperature calculations, biogenic flux calculations, urban planning, and climate mitigation
762 plan preparation; LAI use include biomass allocation, which can be used for fire danger forecasting, and carbon
763 stock monitoring, whilst rice planting/ harvesting days are important for yearly cycle of methane modelling; soil
764 properties are used for soil moisture calculations; and the area covered by lakes can be used for computing
765 evaporation from open water, freshwater storage, unregulated surface water extent, fresh water scarcity indexes,
766 and biogenic green house gas emission, as well as for reproducing different climate mitigation scenarios. All of
767 the above state that CEMS_SurfaceFields_2022 surface fields can be used for weather prediction, Earth system
768 modelling, hydrological and environmental modelling, or statistical analysis in general, with a spatial scale
769 allowing for global, regional and even national applications.

770
771 *Data availability.* The CEMS_SurfaceFields_2022 datasets are freely available for download from the JRC Data
772 Catalogue – global at ~5.6 km at the equator or 3 arc min resolution:
773 <https://data.jrc.ec.europa.eu/dataset/68050d73-9c06-499c-a441-dc5053cb0c86>, over Europe at ~1.9 km at the
774 equator or 1 arc min resolution: <https://data.jrc.ec.europa.eu/dataset/f572c443-7466-4adf-87aa-c0847a169f23>,
775 and are documented in this paper.

776
777 *Author contributions.* CP and PS shaped initial plan of the research; MC and FM executed initial plan; CM, SG
778 and JD reviewed initial results and provided guidance in further research. MC, FM and CP prepared a first draft
779 of the paper, which was adapted to its present state by contributions from CM, SG, JD, PS and HB.

780
781 *Competing interests.* The authors declare that they have no conflict of interest.

782
783 *Acknowledgements.* CEMS_SurfaceFields_2022 is a product and service of the Copernicus Emergency
784 Management Service. Financial support for MC, FM, CM and CP was provided by contract 941462-IPR-2021.

785 Authors thank two anonymous reviewers for their valuable comments and suggestions that helped to shape the
786 manuscript to its current state.

787

788 *Financial support.* This research has been supported by contract 941462-IPR-2021.

789 **References**

- 790 Alfieri, L., Lorini, V., Hirpa, F. A., Harrigan, S., Zsoter, E., Prudhomme, C., and Salamon, P.: A global streamflow
791 reanalysis for 1980–2018. *Journal of Hydrology X*, 6, 100049, ISSN 2589-9155,
792 <https://doi.org/10.1016/j.hydroa.2019.100049>, 2020. (Available online
793 <https://www.sciencedirect.com/science/article/pii/S2589915519300331>, last accessed: 21.01.2024).
- 794 Allen, R. G., Pereira, L. S., Raes, D., and Smith, M.: FAO Irrigation and Drainage Paper No. 56: Crop
795 Evapotranspiration (guidelines for computing crop water requirements), 1998. (Available online:
796 https://www.researchgate.net/publication/284300773_FAO_Irrigation_and_drainage_paper_No_56, last
797 accessed: 21.01.2024).
- 798 Balsamo, G.: Interactive lakes in the Integrated Forecasting System. ECMWF Newsletter No. 137 – Autumn 2013,
799 pp. 30–34, <https://doi.org/10.21957/rffv1gir>, 2013. (Available online: <https://www.ecmwf.int/en/elibrary/80145-interactive-lakes-integrated-forecasting-system>, last accessed: 21.01.2024).
- 800
801 Bates, P. D. and De Roo, A. P. J.: A simple raster-based model for flood inundation simulation. *Journal of*
802 *hydrology*, vol. 236, 1-2, pp. 54–77, ISSN 0022-1694, [https://doi.org/10.1016/S0022-1694\(00\)00278-X](https://doi.org/10.1016/S0022-1694(00)00278-X), 2000.
803 (Available online: <https://www.sciencedirect.com/science/article/abs/pii/S002216940000278X>, last accessed:
804 21.01.2024).
- 805 Beck, H. E., van Dijk, A. I. J. M., Larraondo, P. R., McVicar, T. R., Pan, M., Dutra, E., and Miralles, D. G.:
806 MSWX: Global 3-Hourly 0.1° Bias-Corrected Meteorological Data Including Near-Real-Time Updates and
807 Forecast Ensembles. *Bulletin of the American Meteorological Society*, 103(3), pp. E710-E732,
808 <https://doi.org/10.1175/BAMS-D-21-0145.1>, 2022. (Available online:
809 <https://journals.ametsoc.org/view/journals/bams/103/3/BAMS-D-21-0145.1.xml>, last accessed: 21.01.2024).
- 810 Belleza, G. A. C., Bierkens, M. F. P., and van Vliet M. T. H.: Sectoral water use responses to droughts and
811 heatwaves: analyses from local to global scales for 1990–2019. *Environ. Res. Lett.*, 18 (10), 104008,
812 <https://doi.org/10.1088/1748-9326/acf82e>, 2023.
- 813 Best, M. J., Pryor, M., Clark, D. B., Rooney, G. G., Essery, R. L. H., Menard, C. B., Edwards, J. M., Hendry, M.
814 A., Porson, A., Gedney, N., Mercado, L. M., Sitch, S., Blyth, E., Boucher, O., Cox, P. M., Grimmond, C. S. B.,
815 and Harding, R. J.: The Joint UK Land Environment Simulator (JULES), model description – Part 1: Energy and
816 water fluxes. *Geosci. Model Dev.*, 4, 677–699, <https://doi.org/10.5194/gmd-4-677-2011>, 2011. (Available online:
817 www.geosci-model-dev.net/4/677/2011/, last accessed: 21.01.2024).
- 818 Bhardwaj, A.: Evaluation of Openly Accessible MERIT DEM for Vertical Accuracy in Different Topographic
819 Regions of India. 39th INCA International Congress, Dehradun (India), vol. 39, pp. 239–245, 2021. (Available
820 online:
821 [https://www.researchgate.net/publication/356726804_Evaluation_of_openly_Accessible_MERIT_DEM_for_ve](https://www.researchgate.net/publication/356726804_Evaluation_of_openly_Accessible_MERIT_DEM_for_vertical_accuracy_in_different_topographic_regions_of_India)
822 [rtical_accuracy_in_different_topographic_regions_of_India](https://www.researchgate.net/publication/356726804_Evaluation_of_openly_Accessible_MERIT_DEM_for_vertical_accuracy_in_different_topographic_regions_of_India), last accessed: 21.01.2024).
- 823 Bonan, G., Levis, S., Sitch, S., Vertenstein, M., and Oleson, K.: A dynamic global vegetation model for use with
824 climate models: Concepts and description of simulated vegetation dynamics. *Global Change Biology*, 9, pp. 1543–
825 1566, <https://doi.org/10.1046/j.1365-2486.2003.00681.x>, 2003.
- 826 Brooks, R. H. and Corey, A. T.: Hydraulic properties of porous media. *Hydrology paper No. 3*, Colorado State
827 Univ., Fort Collins, 1964.
- 828 Buchhorn, M., Smets, B., Bertels, L., De Roo, B., Lesiv, M., Tsendbazar, N.-E., Herold, M., and Fritz, S.:
829 Copernicus Global Land Service: Land Cover 100m: collection 3: epoch 2015: Globe (V3.0.1) [Data set]. Zenodo,
830 <https://doi.org/10.5281/zenodo.3939038>, 2020.
- 831 Buchhorn, M., Smets, B., Bertels, L., De Roo, B., Lesiv, M., Tsendbazar, N.-E., Li, L., and Tarko, A.: Copernicus
832 Global Land Service: Land Cover 100m: version 3 Globe 2015-2019: Product User Manual (Dataset v3.0, doc
833 issue 3.4). Zenodo, <https://doi.org/10.5281/zenodo.4723921>, 2021.
- 834 Burek, P., Van Der Knijff, J., and De Roo, A.: LISFLOOD – Distributed Water Balance and Flood Simulation
835 Model – Revised User Manual. Luxembourg: Publications Office of the European Union, JRC78917, 2013.
836 (Available online: <https://publications.jrc.ec.europa.eu/repository/handle/JRC78917>, last accessed: 21.01.2024).
- 837 Burek, P., Bianchi, A., and Gentile, A.: JRC Technical Report: A Pan-European Data Set for hydrological
838 modelling. Luxembourg: Publications Office of the European Union, 2014.
- 839 Büttner, G. and Kosztra, B.: CLC2018 Technical Guidelines, Environment Agency, Austria, 2017. (Available
840 online: <https://land.copernicus.eu/en/technical-library/clc-2018-technical-guidelines/@@download/file>, last
841 accessed: 21.01.2024).

842 Calvin, K., Patel, P., Clarke, L., Asrar, G., Bond-Lamberty, B., Cui, R. Y., Di Vittorio, A., Dorheim, K., Edmonds,
843 J., Hartin, C., Hejazi, M., Horowitz, R., Iyer, G., Kyle, P., Kim, S., Link, R., McJeon, H., Smith, S. J., Snyder, A.,
844 Waldhoff, S., and Wise, M.: GCAM v5.1: representing the linkages between energy, water, land, climate, and
845 economic systems. *Geosci. Model Dev.*, 12, 677–698, <https://doi.org/10.5194/gmd-12-677-2019>, 2019.

846 Carver, G.: Ten years of OpenIFS at ECMWF. ECMWF Newsletter No. 170 – Winter 2021/22, pp. 6-7, 2022.
847 (Available online: <https://www.ecmwf.int/en/newsletter/170/news/ten-years-openifs-ecmwf>, last accessed:
848 21.01.2024).

849 Chai, L. T., Wong, C. J., James, D., Loh, H. Y., Liew, J. J. F., Wong, W. V. C., and Phua, M. H.: Vertical accuracy
850 comparison of multi-source Digital Elevation Model (DEM) with Airborne Light Detection and Ranging
851 (LiDAR). *IOP Conf. Ser.: Earth Environ. Sci.*, 1053, 012025, 2022. (Available online:
852 <https://iopscience.iop.org/article/10.1088/1755-1315/1053/1/012025/pdf>, last accessed: 21.01.2024).

853 Clark, D. B., Mercado, L. M., Sitch, S., Jones, C. D., Gedney, N., Best, M. J., Pryor, M., Rooney, G. G., Essery,
854 R. L. H., Blyth, E., Boucher, O., Harding, R. J., Huntingford, C., and Cox, P. M.: The Joint UK Land Environment
855 Simulator (JULES), model description – Part 2: Carbon fluxes and vegetation dynamics. *Geosci. Model Dev.*, 4,
856 701–722, <https://doi.org/10.5194/gmd-4-701-2011>, 2011. (Available online: [www.geosci-model-](http://www.geosci-model-dev.net/4/701/2011/)
857 [dev.net/4/701/2011/](http://www.geosci-model-dev.net/4/701/2011/), last accessed: 21.01.2024).

858 De Roo, A. P. J., Van Der Knijff, J., Schmuck, G., and Bates, P.: A simple floodplain inundation model to assist
859 in floodplain management. *New trends in water and environmental engineering for safety and life: Eco-compatible*
860 *solutions for aquatic environments*, 1–10, Balkema, Rotterdam, The Netherlands, 2000.

861 De Roo, A., Odijk, M., Schmuck, G., Koster, E., and Lucieer, A.: Assessing the effects of land use changes on
862 floods in the Meuse and Oder catchment. *Physics and Chemistry of the Earth, Part B: Hydrology, Oceans and*
863 *Atmosphere*, vol. 26, 7-8, 593–599, Pergamon, 2001.

864 Defourny, P., Lamarche, C., Bontemps, S., De Maet, T., Van Bogaert, E., Moreau, I., Brockmann, C., Boettcher,
865 M., Kirches, G., Wevers, J., and Santoro, M.: Land Cover CCI PRODUCT USER GUIDE VERSION 2.0 Tech.
866 Rep. ESA, 2017. (Available online: [https://maps.elie.ucl.ac.be/CCI/viewer/download/ESACCI-LC-Ph2-](https://maps.elie.ucl.ac.be/CCI/viewer/download/ESACCI-LC-Ph2-PUGv2_2.0.pdf)
867 [PUGv2_2.0.pdf](https://maps.elie.ucl.ac.be/CCI/viewer/download/ESACCI-LC-Ph2-PUGv2_2.0.pdf), last accessed: 21.01.2024).

868 Dolan, F., Lamontagne, J., Link, R., Hejazi, M., Reed, P., and Edmonds, J.: Evaluating the economic impact of
869 water scarcity in a changing world. *Nat Commun* 12, 1915, <https://doi.org/10.1038/s41467-021-22194-0>, 2021.

870 Eerola, K., Rontu, L., Kourzeneva, E., Kheyrollah Pour, H., and Duguay, C.: Impact of partly ice-free Lake
871 Ladoga on temperature and cloudiness in an anticyclonic winter situation – a case study using a limited area
872 model. *Tellus A*, 66, 23929, <https://doi.org/10.3402/tellusa.v66.23929>, 2014.

873 Florczyk, A. J., Corbane, C., Ehrlich, D., Freire, S., Kemper, T., Maffenini, L., Melchiorri, M., Pesaresi, M.,
874 Politis, P., Schiavina, M., Sabo, F., Zanchetta, L., European Commission, Joint Research Centre: GHSL Data
875 Package 2019 – Public release GHS P2019, EUR 29788 EN, Publications Office of the European Union,
876 Luxembourg, ISBN 978-92-76-13186-1, JRC 117104, <https://data.europa.eu/doi/10.2760/290498>, 2019.

877 Fredlund, D.G. and Xing, A.: Equations for the Soil-Water Characteristic Curve. *Canadian Geotechnical Journal*,
878 31, 521–532, <http://dx.doi.org/10.1139/t94-061>, 1994.

879 Freire, S., MacManus, K., Pesaresi, M., Doxsey-Whitfield, E., and Mills, J.: Development of new open and free
880 multi-temporal global population grids at 250 m resolution. *Geospatial Data in a Changing World*; Association of
881 Geographic Information Laboratories in Europe (AGILE), 2016.

882 Gardner, W. R.: Calculation of capillary conductivity from pressure plate outflow data. *Soil Science Society*
883 *Proceeding*, 20(3), pp. 317–320, <https://doi.org/10.2136/sssaj1956.03615995002000030006x>, 1956.

884 Google Earth Engine: Frequently Asked Questions (GEE: FAQ), 2023. (Available online:
885 <https://earthengine.google.com/faq/>, last accessed: 21.01.2024).

886 Gilbert, M., Nicolas, G., Cinardi, G., Van Boeckel, T. P., Vanwambeke, S. O., Wint, G. R. W., and Robinson, T.
887 P.: Global distribution data for cattle, buffaloes, horses, sheep, goats, pigs, chickens and ducks in 2010. *Sci Data*
888 5, 180227, <https://doi.org/10.1038/sdata.2018.227>, 2018.

889 Gorelick, N., Hancher, M., Dixon, M., Ilyushchenko, S., Thau, D., and Moore, R.: Google Earth Engine:
890 Planetary-scale geospatial analysis for everyone. *Remote Sensing of Environment*, vol. 202, pp. 18–27,
891 <https://doi.org/10.1016/j.rse.2017.06.031>, 2017. (Available online:
892 <https://www.sciencedirect.com/science/article/pii/S0034425717302900>, last accessed: 21.01.2024).

893 Grimaldi, S., Salamon, P., Disperati, J., Zsoter, E., Russo, C., Ramos, A., Carton De Wiart, C., Barnard, C.,
894 Hansford, E., Gomes, G., and Prudhomme, C.: River discharge and related historical data from the Global Flood
895 Awareness System. v4.0. Copernicus Climate Change Service (C3S) Climate Data Store (CDS) [Data set],
896 <https://doi.org/10.24381/cds.a4fdd6b9>, 2022. (Available online:
897 <https://cds.climate.copernicus.eu/cdsapp#!/dataset/10.24381/cds.a4fdd6b9?tab=form>, last accessed: 21.01.2024).

898 Gupta, S., Lehmann, P., Bonetti, S., Papritz, A., and Or, D.: Global prediction of soil saturated hydraulic
899 conductivity using random forest in a Covariate-based GeoTransfer Function (CoGTF) framework. *Journal of*
900 *Advances in Modeling Earth Systems*, 13(4), e2020MS002242, <https://doi.org/10.1029/2020MS002242>, 2021.

901 Harrigan, S., Zsoter, E., Cloke, H., Salamon, P., and Prudhomme, C.: Daily ensemble river discharge reforecasts
902 and real-time forecasts from the operational Global Flood Awareness System. *Hydrol. Earth Syst. Sci.*, 27, 1–19,
903 <https://doi.org/10.5194/hess-27-1-2023>, 2023. (Available online: <https://hess.copernicus.org/articles/27/1/2023/>,
904 last accessed: 21.01.2024).

905 Hejazi, M., Edmonds, J., Clarke, L., Kyle, P., Davies, E., Chaturvedi, V., Wise, M., Patel, P., Eom, J., Calvin, K.,
906 Moss, R., and Kim, S.: Long-term global water projections using six socioeconomic scenarios in an integrated
907 assessment modeling framework. *Technol. Forecast. Social Change*, 81, pp. 205–226,
908 <https://doi.org/10.1016/j.techfore.2013.05.006>, 2014. (Available online:
909 <https://www.sciencedirect.com/science/article/abs/pii/S0040162513001169>, last accessed: 21.01.2024).

910 Hengl, T., de Jesus, J. M., MacMillan, R. A., Batjes, N. H., Heuvelink, G. B. M., Ribeiro, E., Samuel-Rosa, A.,
911 Kempen, B., Leenaars, J. G. B., Walsh, M. G., and Ruiperez Gonzalez, M.: SoilGrids1km – Global Soil
912 Information Based on Automated Mapping. *PLOS ONE* 9(8): e105992,
913 <https://doi.org/10.1371/journal.pone.0105992>, 2014.

914 Hengl, T., de Jesus, J. M., Heuvelink, G. B. M., Ruiperez Gonzalez, M., Kilibarda, M., Blagotić, A., Shangguan,
915 W., Wright, M. N., Geng, X., Bauer-Marschallinger, B., Guevara, M. A., Vargas, R., MacMillan, R. A., Batjes,
916 N. H., Leenaars, J. G. B., Ribeiro, E., Wheeler, I., Mantel, S., and Kempen, B.: SoilGrids250m: Global gridded
917 soil information based on machine learning. *PLOS ONE* 12(2): 1–40,
918 <https://doi.org/10.1371/journal.pone.0169748>, 2017.

919 Hirpa, F. A., Salamon, P., Beck, H. E., Lorini, V., Alfieri, L., Zsoter, E., and Dadson, S. J.: Calibration of the
920 Global Flood Awareness System (GloFAS) using daily streamflow data. *Journal of Hydrology*, vol. 566, 595–
921 606, <https://doi.org/10.1016/j.jhydrol.2018.09.052>, 2018.

922 Hodnett, M. G. and Tomasella, J.: Marked differences between van Genuchten soil water-retention parameters for
923 temperate and tropical soils: a new water-retention pedo-transfer functions developed for tropical soils. *Geoderma*,
924 vol. 108 (3-4), pp. 155–180, ISSN 0016-7061, [https://doi.org/10.1016/S0016-7061\(02\)00105-2](https://doi.org/10.1016/S0016-7061(02)00105-2), 2002.

925 Huang, Z., Hejazi, M., Li, X., Tang, Q., Vernon, C., Leng, G., Liu, Y., Döll, P., Eisner, S., Gerten, D., Hanasaki,
926 N., and Wada, Y.: Reconstruction of global gridded monthly sectoral water withdrawals for 1971–2010 and
927 analysis of their spatiotemporal patterns. *Hydrol. Earth Syst. Sci.*, 22, 2117–2133, [https://doi.org/10.5194/hess-](https://doi.org/10.5194/hess-22-2117-2018)
928 [22-2117-2018](https://doi.org/10.5194/hess-22-2117-2018), 2018.

929 Huijnen, V., Le Sager, P., Köhler, M. O., Carver, G., Rémy, S., Flemming, J., Chabrillat, S., Errera, Q., and van
930 Noije, T.: OpenIFS/AC: atmospheric chemistry and aerosol in OpenIFS 43r3. *Geosci. Model Dev.*, 15, 6221–
931 6241, <https://doi.org/10.5194/gmd-15-6221-2022>, 2022.

932 International Food Policy Research Institute (IFPRI): Global Spatially-Disaggregated Crop Production Statistics
933 Data for 2010 Version 2.0 [Data set]. Harvard Dataverse, <https://doi.org/10.7910/DVN/PRFF8V>, 2019.
934 (Available online: <https://dataverse.harvard.edu/dataset.xhtml?persistentId=doi:10.7910/DVN/PRFF8V>, last
935 accessed: 21.01.2024).

936 Intara, Y. I., Nusantara, A. D., Supanjani, Caniago, Z., and Ekawita, R.: Oil Palm Roots Architecture in Response
937 to Soil Humidity. *International Journal of Oil Palm Vol. 1, Nr. 2*, ISSN: 2614-2376, 2018. (Available online:
938 <https://ijop.id/index.php/ijop/article/view/11/10>, last accessed: 21.01.2024).

939 Karabulut, A., Egho, B. N., Lanzanova, D., Grizzetti, B., Bidoglio, G., Pagliero, L., Bouraoui, F., Aloe, A.,
940 Reynaud, A., Maes, J., Vandecasteele, I., and Mubareka, S.: Mapping water provisioning services to support the
941 ecosystem–water–food–energy nexus in the Danube river basin. *Ecosystem Services*, 17, 278–292,
942 <https://doi.org/10.1016/j.ecoser.2015.08.002>, 2016. (Available online:
943 <https://www.sciencedirect.com/science/article/pii/S221204161530019X>, last accessed: 21.01.2024).

944 Karssenbergh, D., Schmitz, O., Salamon, P., de Jong, K., and Bierkens, M. F. P.: A software framework for
945 construction of process-based stochastic spatio-temporal models and data assimilation. *Environmental Modelling*
946 *& Software*, 25(4), pp. 489–502, <https://doi.org/10.1016/j.envsoft.2009.10.004>, 2010.

947 Kimpson, T., Choulga, M., Chantry, M., Balsamo, G., Boussetta, S., Dueben, P., and Palmer, T.: Deep learning
948 for quality control of surface physiographic fields using satellite Earth observations. *Hydrol. Earth Syst. Sci.*,
949 27(24), 4661–4685, <https://doi.org/10.5194/hess-27-4661-2023>, 2023.

950 Köhler, M. O., Hill, A. A., Huijnen, V., and Le Sager, P.: Enhancing OpenIFS by adding atmospheric composition
951 capabilities. *ECMWF Newsletter No. 175 – Spring 2023*, pp. 27–31, <http://doi.org/10.21957/np36mk1s9d>, 2023.
952 (Available online: [https://www.ecmwf.int/en/newsletter/175/earth-system-science/enhancing-openifs-adding-](https://www.ecmwf.int/en/newsletter/175/earth-system-science/enhancing-openifs-adding-atmospheric-composition)
953 [atmospheric-composition](https://www.ecmwf.int/en/newsletter/175/earth-system-science/enhancing-openifs-adding-atmospheric-composition), last accessed: 21.01.2024).

954 Kohli, A., Frenken, K., and Spottorno, C.: Disambiguation of water statistics. *FAO AQUASTAT Report*,
955 *AQUASTAT Programme*, FAO, pp. 1–6, 2012. (Available online: <https://www.fao.org/3/bc816e/bc816e.pdf>, last
956 accessed: 21.01.2024).

957 Laborte, A. G., Gutierrez, M. A., Balanza, J. G., Saito, K., Zwart, S. J., Boschetti, M., Murty, M. V. R., Villano,
958 L., Aunario, J. K., Reinke, R., Koo, J., Hijmans, R. J., and Nelson, A.: *RiceAtlas*, a spatial database of global rice
959 calendars and production [Data set]. Harvard Dataverse, V3, <https://doi.org/10.7910/DVN/JE6R2R>, 2017a.

960 Laborte, A. G., Gutierrez, M. A., Balanza, J. G., Saito, K., Zwart, S. J., Boschetti, M., Murty, M. V. R., Villano,
961 L., Aunario, J. K., Reinke, R., Koo, J., Hijmans, R. J., and Nelson, A.: RiceAtlas, a spatial database of global rice
962 calendars and production. *Sci Data.*, 4:170074, PMID: 28556827, PMCID: PMC5448352,
963 <https://doi.org/10.1038/sdata.2017.74>, 2017b. (Available online:
964 <https://www.ncbi.nlm.nih.gov/pmc/articles/PMC5448352/>, last accessed: 21.01.2024).

965 Lawrence, D. M., Fisher, R. A., Koven, C. D., Oleson, K. W., Swenson, S. C., Bonan, G., Collier, N., Ghimire,
966 B., van Kampenhout, L., Kennedy, D., Kluzek, E., Lawrence, P. J., Li, F., Li, H., Lombardozzi, D., Riley, W. J.,
967 Sacks, W. J., Shi, M., Vertenstein, M., Wieder, W. R., Xu, C., Ali, A. A., Badger, A. M., Bisht, G., van den
968 Broeke, M., Brunke, M. A., Burns, S. P., Buzan, J., Clark, M., Craig, A., Dahlin, K., Drewniak, B., Fisher, J. B.,
969 Flanner, M., Fox, A. M., Gentine, P., Hoffman, F., Keppel-Aleks, G., Knox, R., Kumar, S., Lenaerts, J., Leung,
970 L. R., Lipscomb, W. H., Lu, Y., Pandey, A., Pelletier, J. D., Perket, J., Randerson, J. T., Ricciuto, D. M.,
971 Sanderson, B. M., Slater, A., Subin, Z. M., Tang, J., Thomas, R. Q., Val Martin, M., and Zeng, X.: The Community
972 Land Model version 5: Description of new features, benchmarking, and impact of forcing uncertainty. *Journal of*
973 *Advances in Modeling Earth Systems*, 11(12), pp. 4245–4287, <https://doi.org/10.1029/2018MS001583>, 2019.

974 Lehner, B. and Döll, P.: Development and validation of a global database of lakes, reservoirs and wetlands. *Journal*
975 *of Hydrology*, vol. 296(1-4), pp. 1–22, <https://doi.org/10.1016/j.jhydrol.2004.03.028>, 2004. (Available online:
976 <http://dx.doi.org/10.1016/j.jhydrol.2004.03.028>, last accessed: 21.01.2024).

977 Lv, S., Zeng, Y., Wen, J., Zhao, H., and Su, Z.: Estimation of Penetration Depth from Soil Effective Temperature
978 in Microwave Radiometry. *Remote Sens.*, vol. 10(4), 519. <https://doi.org/10.3390/rs10040519>, 2018.

979 Marthews, T. R., Dadson, S. J., Clark, D. B., Blyth, E. M., Hayman, G. D., Yamazaki, D., Becher, O. R. E.,
980 Martinez-de la Torre, A., Prigent, C., and Jimenez, C.: Inundation prediction in tropical wetlands from JULES-
981 CaMa-Flood global land surface simulations. *Hydrology and Earth System Sciences*, vol. 26(12), 3151–3175,
982 <https://doi.org/10.5194/hess-26-3151-2022>, 2022. (Available online:
983 <https://hess.copernicus.org/articles/26/3151/2022/>, last accessed: 21.01.2024).

984 Martínez-Sánchez, E.: Scientific Quality Evaluation of LAI/FAPAR/FCOVER Collection 1km Version 1 and
985 Version 2 Issue I1.00, 2020. (Available online:
986 [https://land.copernicus.eu/global/sites/cgls.vito.be/files/products/CGLOPS1_SQE2019_LAI1km-](https://land.copernicus.eu/global/sites/cgls.vito.be/files/products/CGLOPS1_SQE2019_LAI1km-V1%26V2_I1.00.pdf)
987 [V1%26V2_I1.00.pdf](https://land.copernicus.eu/global/sites/cgls.vito.be/files/products/CGLOPS1_SQE2019_LAI1km-V1%26V2_I1.00.pdf), last accessed: 21.01.2024).

988 McManamay, R. A., KC, B., Allen-Dumas, M. R., Kao, S. C., Brelsford, C. M., Ruddell, B. L., Sanyal, J., Stewart,
989 R. N., and Bhaduri, B. L.: Reanalysis of water withdrawal for irrigation, electric power, and public supply sectors
990 in the conterminous United States, 1950–2016. *Water Resources Research*, 57(2), e2020WR027751,
991 <https://doi.org/10.1029/2020WR027751>, 2021.

992 Moiret-Guigand, A.: Copernicus Land monitoring services – CLC2018 / CLCC1218 VALIDATION REPORT,
993 Issue 1.3, 2021 (Available online: [https://land.copernicus.eu/en/technical-library/clc-2018-and-clc-change-2012-](https://land.copernicus.eu/en/technical-library/clc-2018-and-clc-change-2012-2018-validation-report/@@download/file)
994 [2018-validation-report/@@download/file](https://land.copernicus.eu/en/technical-library/clc-2018-and-clc-change-2012-2018-validation-report/@@download/file), last accessed: 21.01.2024).

995 Notaro, M., Holman, K., Zarrin, A., Fluck, E., Vavrus, S., and Bennington, V.: Influence of the Laurentian Great
996 Lakes on Regional Climate. *J. Climate*, 26(3), pp. 789–804, <https://doi.org/10.1175/JCLI-D-12-00140.1>, 2013.

997 O’Callaghan, J. F. and Mark, D. M.: The Extraction of Drainage Networks from Digital Elevation Data. *Computer*
998 *Vision, Graphics, and Image Processing*, 28(3), pp. 323–344, [https://doi.org/10.1016/S0734-189X\(84\)80011-0](https://doi.org/10.1016/S0734-189X(84)80011-0),
999 1984.

1000 Pesaresi, M. and Politis, P.: GHS-BUILT-S R2022A - GHS built-up surface grid, derived from Sentinel2
1001 composite and Landsat, multitemporal (1975-2030) [Data set]. European Commission, Joint Research Centre
1002 (JRC), <https://doi.org/10.2905/D07D81B4-7680-4D28-B896-583745C27085>, 2022. (Available online:
1003 <http://data.europa.eu/89h/d07d81b4-7680-4d28-b896-583745c27085>, last accessed: 21.01.2024).

1004 Rosbjerg, D. and Madsen, H.: Concepts of hydrologic modeling. In *Encyclopedia of Hydrological Sciences* (eds
1005 M.G. Anderson and J.J. McDonnell), 10, 1–9, <https://doi.org/10.1002/0470848944.hsa009>, 2006.

1006 Samuelsson, P., Kourzeneva, E., and Mironov, D.: The impact of lakes on the European climate as simulated by
1007 a regional climate model. *Boreal Environ. Res.*, 15(2), pp. 113–129, <http://hdl.handle.net/10138/233079>, 2010.
1008 (Available online: [https://helda.helsinki.fi/server/api/core/bitstreams/feb9f8de-e831-4e9e-9ee6-](https://helda.helsinki.fi/server/api/core/bitstreams/feb9f8de-e831-4e9e-9ee6-07ac7df898eb/content)
1009 [07ac7df898eb/content](https://helda.helsinki.fi/server/api/core/bitstreams/feb9f8de-e831-4e9e-9ee6-07ac7df898eb/content), last accessed: 21.01.2024).

1010 Schiavina, M., Freire, S., and MacManus, K.: GHS-POP R2019A - GHS population grid multitemporal (1975,
1011 1990, 2000, 2015). European Commission, Joint Research Centre (JRC) [Data set],
1012 <https://doi.org/10.2905/0C6B9751-A71F-4062-830B-43C9F432370F>, 2019. (Available online:
1013 <https://data.jrc.ec.europa.eu/dataset/0c6b9751-a71f-4062-830b-43c9f432370f>, last accessed: 21.01.2024).

1014 Schiavina, M., Melchiorri, M., Pesaresi, M., Politis, P., Freire, S., Maffeni, L., Florio, P., Ehrlich, D., Goch, K.,
1015 Tommasi, P., Kemper, T., European Commission, Joint Research Centre: GHSL Data Package 2022 – Public
1016 release GHS P2022, Publication Office of the European Union, JRC 129516, ISBN 978-92-76-53071-8,
1017 <https://doi.org/10.2760/19817>, 2022.

1018 Smets, B.: Product User Manual of LAI/FAPAR/FCOVER Collection 1km Version 2 Issue 1.33, 2019. (Available
1019 online: https://land.copernicus.eu/global/sites/cgls.vito.be/files/products/CGLOPS1_PUM_LAI1km-
1020 [V2_I1.33.pdf](https://land.copernicus.eu/global/sites/cgls.vito.be/files/products/CGLOPS1_PUM_LAI1km-V2_I1.33.pdf), last accessed: 21.01.2024).

1021 Smith, P. J., Pappenberger, F., Wetterhall, F., Del Pozo, J. T., Krzeminski, B., Salamon, P., Muraro, D., Kalas,
1022 M., and Baugh, C.: On the operational implementation of the European Flood Awareness System (EFAS). *Flood*
1023 *forecasting: A Global Perspective*, Academic Press, pp. 313–348, [https://doi.org/10.1016/B978-0-12-801884-](https://doi.org/10.1016/B978-0-12-801884-2.00011-6)
1024 [2.00011-6](https://doi.org/10.1016/B978-0-12-801884-2.00011-6), 2016.

1025 Sparrow, S., Bowery, A., Carver, G. D., Köhler, M. O., Ollinaho, P., Pappenberger, F., Wallom, D., and
1026 Weisheimer, A.: OpenIFS@home version 1: a citizen science project for ensemble weather and climate
1027 forecasting. *Geosci. Model Dev.*, 14(6), 3473–3486, <https://doi.org/10.5194/gmd-14-3473-2021>, 2021.

1028 Supit, I., Hoojer, A. A., and Van Diepen, C. A.: System description of the Wofost 6.0 crop simulation model
1029 implemented in CGMS. Volume 1: Theory and Algorithms, 1994. (Available online:
1030 [https://www.researchgate.net/publication/282287246_System_description_of_the_Wofost_60_crop_simulation_](https://www.researchgate.net/publication/282287246_System_description_of_the_Wofost_60_crop_simulation_model_implemented_in_CGMS_Volume_1_Theory_and_Algorithms)
1031 [model_implemented_in_CGMS_Volume_1_Theory_and_Algorithms](https://www.researchgate.net/publication/282287246_System_description_of_the_Wofost_60_crop_simulation_model_implemented_in_CGMS_Volume_1_Theory_and_Algorithms), last accessed: 21.01.2024).

1032 Te Chow, V.: Open-channel Hydraulics. Civil engineering series (publisher McGraw-Hill Book Company Inc.),
1033 ISBN 07-010776-9, 1959. (Available online: [https://heidarpour.iut.ac.ir/sites/heidarpour.iut.ac.ir/files/u32/open-](https://heidarpour.iut.ac.ir/sites/heidarpour.iut.ac.ir/files/u32/open-chow.pdf)
1034 [chow.pdf](https://heidarpour.iut.ac.ir/sites/heidarpour.iut.ac.ir/files/u32/open-chow.pdf), last accessed: 21.01.2024).

1035 Tóth, B., Weynants, M., Nemes, A., Makó, A., Bilas, G., and Tóth, G.: New generation of hydraulic pedotransfer
1036 functions for Europe. *Eur J Soil Sci*, 66(1), pp. 226-238, <https://doi.org/10.1111/ejss.12192>, 2015.

1037 Van Der Knijff, J. and De Roo, A.: LISFLOOD – Distributed Water Balance and Flood Simulation Model,
1038 Revised User Manual. EUR 22166 EN/2, Office for Official Publications of the European Communities,
1039 Luxembourg, 109 pp, 2008.

1040 Van Der Knijff, J. M., Younis, J., and De Roo, A. P. J.: LISFLOOD: A GIS-based distributed model for river
1041 basin scale water balance and flood simulation. *Int. J. Geogr. Inf. Sci.*, 24(2), 189–212, 2010.

1042 van Genuchten, M. T.: A closed-form equation for predicting the hydraulic conductivity of unsaturated soils. *Soil*
1043 *Sci. Soc. Am. J.*, 44, 892–898, 1980.

1044 Vanham, D., Alfieri, L., Flörke, M., Grimaldi, S., Lorini, V., De Roo, A., and Feyen, L.: The number of people
1045 exposed to water stress in relation to how much water is reserved for the environment: a global modelling study.
1046 *The Lancet Planetary Health*, vol. 5(11), pp. e766–e774, [https://doi.org/10.1016/S2542-5196\(21\)00234-5](https://doi.org/10.1016/S2542-5196(21)00234-5), 2021.
1047 (Available online: <https://www.sciencedirect.com/science/article/pii/S2542519621002345>, last accessed:
1048 21.01.2024).

1049 Vassolo, S. and Döll, P.: Global-scale gridded estimates of thermoelectric power and manufacturing water use.
1050 *Water Resour. Res.* 41(4), <https://doi.org/10.1029/2004WR003360>, 2005.

1051 Vavrus, S., Notaro, M., and Zarrin, A.: The role of ice cover in heavy lake-effect snowstorms over the Great Lakes
1052 Basin as simulated by RegCM4. *Mon. Weather Rev.*, 141, 148–165, 2013.

1053 Voisin, N., Liu, L., Hejazi, M., Tesfa, T., Li, H., Huang, M., Liu, Y., and Leung, L. R.: One-way coupling of an
1054 integrated assessment model and a water resources model: evaluation and implications of future changes over the
1055 US Midwest. *Hydrol. Earth Syst. Sci.*, 17(11), 4555–4575, <https://doi.org/10.5194/hess-17-4555-2013>, 2013.

1056 Wada, Y., van Beek, L. P. H., Viviroli, D., Dürr, H. H., Weingartner, R., and Bierkens, M. F. P.: Global monthly
1057 water stress: 2. Water demand and severity of water stress. *Water Resour. Res.*, 47(7), W07518,
1058 <https://doi.org/10.1029/2010WR009792>, 2011.

1059 Yamazaki, D., Oki, T., and Kanae, S.: Deriving a global river network map and its sub-grid topographic
1060 characteristics from a fine-resolution flow direction map. *Hydrol. Earth Syst. Sci.*, 13(11), 2241–2251,
1061 <https://doi.org/10.5194/hess-13-2241-2009>, 2009.

1062 Yamazaki, D., Kanae, S., Kim, H., and Oki, T.: A physically based description of floodplain inundation dynamics
1063 in a global river routing model. *Water Resour. Res.*, 47(4), W04501, <https://doi.org/10.1029/2010WR009726>,
1064 2011.

1065 Yamazaki, D., Ikeshima, D., Tawatari, R., Yamaguchi, T., O'Loughlin, F., Neal, J. C., Sampson, C. C., Kanae, S.,
1066 and Bates, P. D.: A high-accuracy map of global terrain elevations. *Geophys. Res. Lett.*, 44(11), pp. 5844–5853,
1067 <https://doi.org/10.1002/2017GL072874>, 2017.

1068 Yamazaki, D., Ikeshima, D., Sosa, J., Bates, P. D., Allen, G. H., and Pavelsky, T. M.: MERIT Hydro: A high-
1069 resolution global hydrography map based on latest topography datasets. *Water Resources Research*, vol. 55(6),
1070 pp. 5053–5073, <https://doi.org/10.1029/2019WR024873>, 2019.

1071 Yu, Q., You, L., Wood-Sichra, U., Ru, Y., Joglekar, A. K. B., Fritz, S., Xiong, W., Lu, M., Wu, W., and Yang,
1072 P.: A cultivated planet in 2010 – Part 2: The global gridded agricultural-production maps. *Earth Syst. Sci. Data*,
1073 12(4), 3545–3572, <https://doi.org/10.5194/essd-12-3545-2020>, 2020.

1074 Zhang, Y. and Schaap, M. G.: Estimation of saturated hydraulic conductivity with pedotransfer functions: A
1075 review. *Journal of Hydrology*, vol. 575, pp. 1011–1030, ISSN 0022-1694,
1076 <https://doi.org/10.1016/j.jhydrol.2019.05.058>, 2019.

1077 Zhang, J., Liu, D., Guo, S., Xiong, L., Liu, P., Chen, J., and Yin, J.: High resolution annual irrigation water use
1078 maps in China based-on input variables selection and convolutional neural networks. *Journal of Cleaner*
1079 *Production*, 405, 136974, <https://doi.org/10.1016/j.jclepro.2023.136974>, 2023. (Available online:
1080 <https://www.sciencedirect.com/science/article/pii/S0959652623011320>, last accessed: 21.01.2024).

1081 **Appendix**

1082 **Appendix 1**

1083 All data sources used to produce dataset's surface fields, mentioned in Sections 3 to 9, are described here. All data
1084 considered were open source, freely available, updated as recently as possible, with recognised reference on their
1085 quality.

1086 **1.1 Catchment morphology and river network**

1087 **The MERIT DEM: Multi-Error-Removed Improved-Terrain Digital Elevation Model v.1.0.3** [15 October,
1088 2018] (further referred as MERIT DEM) is a high accuracy global DEM at 3 arc second resolution (~90 m at the
1089 equator) covering land area from 90 N to 60 S, selected for its ability to clearly represent landscapes such as river
1090 networks and hill-valley structures even in flat areas where height errors could be larger than topography
1091 variability (Yamazaki et al., 2017; Bhardwaj, 2021; Chai et al., 2022). It is derived from seven different open-
1092 source datasets, delivered as 57 GeoTiff files 30° by 30° region each, at ~90 m resolution (in total 90.0 GB),
1093 representative of the year 2018. More detail on method, data content and access can be found in Yamazaki et al.
1094 (2017) and MERIT DEM web-page http://hydro.iis.u-tokyo.ac.jp/~yamadai/MERIT_DEM.
1095 The MERIT DEM was used to compute standard deviation of elevation, gradient and channel geometry fields.

1096
1097 **The Catchment-based Macro-scale Floodplain (CaMa-Flood) Global River Hydrodynamics Model v4.0**
1098 **maps** (further referred as CaMa-Flood) are used for the basic maps describing all physical properties of the river
1099 network. It is derived from MERIT Hydro (MERIT Hydro is a global hydrography dataset, created by using
1100 elevation (i.e. MERIT DEM) and several inland water maps; more detail can be found in Yamazaki et al. (2019)
1101 and MERIT Hydro web-page http://hydro.iis.u-tokyo.ac.jp/~yamadai/MERIT_Hydro) for high resolution river
1102 routing applications using the FLOW algorithm (Yamazaki et al., 2009; Yamazaki et al., 2011). The maps include
1103 information on channel length, river topography parameters, floodplain elevation profile, channel width and
1104 channel depth. The maps exist at 15, 6, 5, 3 and 1 arc min resolutions covering land area from 90 N to 60 S,
1105 representative of the year 2017, and for each resolution, they are available as one single file with all variables in
1106 NetCDF format (for 1 arc min 737.0 MB). More detail on method, data content and access can be found in
1107 Yamazaki et al. (2011) and CaMa-Flood web-page [http://hydro.iis.u-tokyo.ac.jp/~yamadai/cama-](http://hydro.iis.u-tokyo.ac.jp/~yamadai/cama-flood/index.html)
1108 [flood/index.html](http://hydro.iis.u-tokyo.ac.jp/~yamadai/cama-flood/index.html). Note that whilst the CaMaFlood maps were originally generated for the specific use of the
1109 CaMa-Flood model, they can also serve as basic to derive alternative maps for other environmental models, as
1110 done here.

1111 The CaMa-Flood maps were used to create the local drainage direction (LDD), upstream drainage area, channel
1112 geometry and land masks fields.

1113 **1.2 Land use fields**

1114 **The Copernicus Global Land Service (CGLS) Land Cover (LC) 100m map** (further referred as CGLS-LC100)
1115 is a global land cover map of the year 2015 (Buchhorn et al., 2020). It is derived from the PROBA-V 100 m
1116 satellite image collection, a database of high quality land cover training sites and ancillary datasets, reaching an
1117 accuracy of 80 % at Level1 (Buchhorn et al., 2021). It contains 23 classes for discrete classification and 10 classes
1118 for continuous cover fractions; and it is delivered as 15 files in GeoTiff format (in total 39.3 GB) at 100 m
1119 resolution covering land area from 90 N to 60 S and representative of the year 2015. More detail on method, data
1120 content and access can be found in Buchhorn et al. (2021) and Copernicus web-site
1121 <https://land.copernicus.eu/global/products/lc>.

1122 The CGLS-LC100 was used to generate crop parameters and Manning's surface roughness coefficient for forest
1123 and other land cover types, to generate forest, inland water, and sealed surface fraction fields, following a basic
1124 quality check on large water bodies (i.e. correcting Fox Basin and Caspian Sea).

1125
1126 **The Coordination of Information on the Environment (CORINE) Land Cover (CLC) inventory for 2018**
1127 (further referred as CLC2018) is a set of maps describing the land cover/ land use status of 2018 covering

1128 39 countries in Europe with a total area of over 5.8 Mkm². The dataset is derived from satellite imagery (mainly
1129 Sentinel-2, based on a constellation of two satellites orbiting Earth at altitude of 786 km 180° apart revisiting
1130 equator every 5 days, and for gap filling Landsat-8, making a constellation together with Landsat-9 satellite
1131 orbiting Earth at altitude of 705 km each revisiting equator every 16 days) and in-situ data and contains 44 classes,
1132 delivered as one GeoTiff raster file (125.0 MB) at 100m resolution covering land area over Europe, representative
1133 of the time period 2017-2018. The overall accuracy for CLC2018 is 92 % for the blind analysis (i.e. validation
1134 team had no knowledge of the CLC2018 thematic classes) but there are regional variations: the Black Sea
1135 geographical region has the lowest accuracy of 84 %; country-wise overall accuracy vary from 86 % for Portugal
1136 to 99 % for Iceland, lowest accuracy being linked to the landscape complexity (Moiret-Guigand, 2021). More
1137 detail on method, data content and access can be found in Büttner and Kosztra (2017) and Moiret-Guigand (2021),
1138 and Copernicus web-site <https://land.copernicus.eu/pan-european/corine-land-cover/clc2018>.
1139 The CLC2018 was used to generate the irrigated crop fraction and rice fraction fields.

1141 **The Spatial Production Allocation Model (SPAM) – Global Spatially-Disaggregated Crop Production**
1142 **Statistics Data for 2010 v2.0** (further referred as SPAM2010) is a global dataset generated in 2020, which
1143 redistributes crop production information from country and sub-national provinces level to a finer grid cell level
1144 (IFPRI, 2019). It is derived from numerous data sources, including crop production statistics, cropland data,
1145 biophysical crop “suitability” assessments, spatial distribution of specific crops or crop systems, and population
1146 density. SPAM2010 contains estimates of crop distributions within disaggregated units (based on a cross-entropy
1147 approach) for 42 crops and two production systems (irrigated and rainfed), and is delivered as 84 files in shapefile
1148 format at 10 km (5 arc min) resolution covering land area from 90 N to 60 S and representative of the year 2010
1149 (in total 2.2 GB). Based on crop expert judgement from international (i.e. International Rice Research Institute,
1150 International Maize and Wheat Improvement Center) and national organisations (i.e. The Chinese Academy of
1151 Agricultural Sciences) SPAM2010 over Europe and America is more accurate than over Africa and South East
1152 Asia, with best performance in allocating rice; grid-by-grid comparison of crop areas with independent Cropland
1153 Data Layer (produced by using satellite images and vast amount of ground truth) over continental United States
1154 shows coefficient of determination (R^2) 0.7-0.9 and root mean square error (RMSE) 231-307 ha indicating a
1155 relatively high reliability, with highest R^2 and lowest RMSE values are for maize and soybean (Yu et al., 2020).
1156 More detail on method, data content and access can be found in Yu et al. (2020) and MapSPAM web-site
1157 <https://mapspam.info>.
1158 SPAM2010 was used to compute the irrigated crop and rice fractions, crop parameters and Manning’s surface
1159 roughness coefficient for irrigated crop fields.

1160 1.3 Vegetation properties

1161 **The Food and Agriculture Organisation (FAO) of the United Nations Irrigation and Drainage Paper No.**
1162 **56** (further referred as FAO56) is a publication covering geographically referenced statistics for crop development
1163 stages, crop coefficients, crop height, rooting depth, and soil water depletion fraction for common crops found
1164 across the world; it also covers procedures for information aggregation, e.g. on the grid. It is delivered as an article
1165 with a set of tables and equations and can be considered as the most complete source of information on crop
1166 properties. More detail on method and data content can be found in Allen et al. (1998) and FAO online crop
1167 information web-page <http://www.fao.org/land-water/databases-and-software/crop-information/tobacco/en/>.
1168 FAO56 was used to compute the crop coefficients for forest, irrigated crops and other land cover types (online
1169 crop information was specifically used for tobacco); and for intermediate computations such as depletion fraction
1170 for different crop and surface types (table), crop height and root depth fields.

1171
1172 **Intara** et al. (2018) is a publication covering oil palm roots architecture.
1173 Intara et al. (2018) was used for oil palm root depth information in addition to FAO56.

1174
1175 **Burek** et al. (2014) is a publication covering summarised information for crop coefficients, rooting depth, crop
1176 group number and Manning’s surface roughness coefficient for different surface types.
1177 Burek et al. (2014) was used for built-up, bare/ sparse vegetation, snow & ice, permanent inland water, ocean &
1178 seas, herbaceous wetland, moss & lichen surface types crop coefficients, rooting depth, crop group number and
1179 Manning’s surface roughness coefficient information in addition to FAO56 and other sources.

1180
1181 **The Wofost 6.0 crop simulation model description** (further referred as SUPIT) is a publication on developing,
1182 validating, and testing new or already existing agrometeorological models (Supit et al., 1994). It contains crop
1183 group information for several crops as examples, and relation of a crop group from water depletion fraction. The
1184 publication is delivered as a book with a set of tables and equations. Information on crop group is still considered
1185 up-to-date. More detail on method and data content can be found in Supit et al. (1994).

1186 SUPIT was used to compute the crop group fields for forest, irrigated crops and other land cover types.

1187

1188 **The Open-Channel Hydraulics manual** (further referred as CHOW) is a publication on open-channel
1189 hydraulics, including basic principles and different types of flows, i.e. uniform, gradually varied, rapidly varied,
1190 and unsteady (Te Chow, 1959). It contains information on roughness coefficient over different surfaces. The
1191 publication is delivered as a book with a set of tables and equations. More detail on method and data content can
1192 be found in Te Chow (1959).

1193 CHOW was used to compute the Manning's surface roughness coefficient fields for forest, irrigated crops and
1194 other land cover types.

1195

1196 **The Copernicus Global Land Service (CGLS) Leaf Area Index (LAI) 1km Version 2 collection** (further
1197 referred as CGLS-LAI) is a set of global maps without missing data describing vegetation dynamics – the annual
1198 evolution of LAI at 10-day intervals over the period of 1999-2020. The dataset is derived from
1199 SPOT/VEGETATION and PROBA-V data. The dataset's root mean square deviations over 20 GBOV sites over
1200 the period 2014-2018 is 0.92, compared to 1.19 for MODIS C6 LAI product (Martinez-Sanchez, 2020). The
1201 dataset is delivered as one multi-band file per year in NetCDF (netCDF4 CF-1.6) format (14.7 GB per year) at 1
1202 km resolution covering land area from 90 N to 60 S and representative of the 10-year period of 2010-2019. More
1203 detail on method, data content and access can be found in Smets (2019) and Martinez-Sanchez (2020), and
1204 Copernicus web-site <https://land.copernicus.eu/global/products/lai>.

1205 CGLS-LAI was used to compute the LAI fields for forest, irrigated crops and other land cover types.

1206

1207 **The RiceAtlas v3** (further referred as RiceAtlas) is a spatial database of global rice calendars and production. It
1208 contains information on start, peak and end dates of sowing, transporting and harvesting rice, derived from global
1209 and regional databases, national publications, online reports, and expert knowledge. It is delivered as 7 files in
1210 shapefile format (in total 195.8 MB) for administrative units (in total 2725 spatial units) at 1 km resolution for the
1211 national production totals to match the years 2010-2012 (Laborte et al., 2017a). RiceAtlas is ~10 times more
1212 spatially detailed, and has ~7 times more special units comparing with other global datasets (Laborte et al., 2017b).
1213 More detail on method, data content and access can be found in Laborte et al. (2017a) and Laborte et al. (2017b).
1214 RiceAtlas was used to compute rice planting and rice harvesting days for three different seasons.

1215 1.4 Soil properties

1216 **The International Soil Reference and Information Centre (ISRIC) SoilGrids250m global gridded soil**
1217 **information release 2017** (further referred as SoilGrids250m) is an output of special predictions produced by the
1218 SoilGrids system, as a set of global soil property and class maps at 250 m resolution. It is derived from soil profile
1219 data (from ~150,000 sites globally) with the use of machine learning, and contains information on soil
1220 characteristics at six standard depths, including soil textures (clay, silt, sand), depth to bedrock, bulk density,
1221 organic carbon, pH and cation exchange capacity. It is delivered as 43 files in GeoTiff format (in total 111.8 GB)
1222 at 250 meters resolution covering land area with no permanent ice and representative for the year 2010 (according
1223 to land cover) (Hengl et al., 2017). SoilGrids250m pH comparison with SSURGO data over California (depth 0-
1224 200 cm) and Soil and Landscape Grid of Australia data over Tasmania (depth 0-5 cm) show high correlation, 0.79
1225 and 0.71 respectively (Hengl et al., 2017). Despite its limited accuracy (i.e. between 30 and 70 %, according to
1226 the SoilGrids web-site) due to the scarcity of soil profile observations (especially in Central Asia, Arctic regions
1227 coastal area and desert), low resolution of covariates data and algorithms, it was selected as the most recent source
1228 of information. More detail on method, data content and access can be found in Hengl et al. (2017) and
1229 SoilGrids250m web-site <https://www.isric.org/explore/soilgrids/faq-soilgrids-2017>.

1230 SoilGrids250m was used to compute the soil depth and soil hydraulic properties for forest and non-forest.

1231 1.5 Lakes

1232 **The Global Lakes and Wetlands Database** (further referred as GLWD) is a global database of water bodies. It
1233 is derived from a combination of global and regional lake data sets, registers and inventories (i.e. point information
1234 with descriptive attributes), and digital maps (i.e. polygons, rasterised global land cover and land use maps). The
1235 database consists of two global files in shapefile format at spatial resolutions of up to 1:1 million – GLWD-1 with
1236 3067 largest lake and 654 largest reservoir polygons (6.4 MB), and GLWD-2 with ~250000 smaller lake and
1237 reservoir polygons (32.0 MB); and of one global file in ADF raster format at 30 arc sec resolution – GLWD-3
1238 combines GLWD-1, GLWD-2 and additional information (8.9 MB). Validation against documented data shows
1239 that GLWD represents good wetland maximum extent, and describes comprehensively lakes with surface area
1240 greater or equal 1 km² (Lehner and Döll, 2004). More detail on method, data content and access can be found in

1241 Lehner and Döll (2004) and GLWD web-site [https://www.worldwildlife.org/pages/global-lakes-and-wetlands-](https://www.worldwildlife.org/pages/global-lakes-and-wetlands-database)
1242 [database](https://www.worldwildlife.org/pages/global-lakes-and-wetlands-database).
1243 GLWD (i.e. only GLWD-1 and GLWD-2) was used to compute the discrete lake mask field.

1244 1.6 Water demand

1245 **AQUASTAT** is the FAO's global information system on water resources and agricultural water management.
1246 AQUASTAT collects information on water use via the network of AQUASTAT National Correspondents who
1247 are required to fill the annual questionnaire and collaborate with AQUASTAT team in the data validation process.
1248 Five types of manual checks are followed by automatic implementation of almost 200 validation rules. The dataset
1249 includes data for 180 countries worldwide, yearly data from 1979 to 2019 were used to produce the maps presented
1250 by this manuscript. Float, lumped values for each country for the variables "Gross Domestic Product (GDP)",
1251 "Industry, value added to GDP", "Agricultural water withdrawal", "Industrial water withdrawal", "Municipal
1252 water withdrawal", "Total water withdrawal", and "Irrigation water withdrawal" were obtained in CSV format (2
1253 files, in total 2.0 MB) from the AQUASTAT data acquisition dashboard
1254 (https://tableau.apps.fao.org/views/ReviewDashboard-v1/country_dashboard). More detail on method, data
1255 content and access can be found in AQUASTAT web-site
1256 <https://www.fao.org/aquastat/en/overview/methodology/>.

1257 AQUASTAT variables were used accordingly to compute water demand fields for domestic, industrial, energy,
1258 livestock use.

1259
1260 **United States Geological Survey National Water Information System** (further referred as USGS NWIS) is a
1261 national database on water use data for the United States (US) with annual statistics provided every 5 years since
1262 1950. The water use data are best estimates produced by the USGS in cooperation with local, state, and federal
1263 agencies as well as academic and private organisations. The water use data are lumped values (float numbers) for
1264 each state, delivered in plain text format (52 files, in total 56.0 MB). Following variables were used: "Domestic
1265 total self-supplied withdrawals, fresh, in Mgal/d", "Public Supply total self-supplied withdrawals, fresh, in
1266 Mgal/d", "Industrial total self-supplied withdrawals, fresh, in Mgal/d", "Total Thermoelectric Power total self-
1267 supplied withdrawals, fresh, in Mgal/d", "Total Thermoelectric Power power generated, in gigawatt-hours", and
1268 "Livestock total self-supplied withdrawals, fresh, in Mgal/d". More detail on method, data content and access can
1269 be found in USGS NWIS web-site <https://waterdata.usgs.gov/nv/nwis/wu>. For this study, data from 1985 to 2015
1270 were used.

1271 USGS NWIS variables were used accordingly to refine the global water demand fields for the domestic, industrial,
1272 energy, livestock use sectors for the US.

1273
1274 **Global Change Analysis Model** (further referred as GCAM) is an integrated, multi-sector model developed by
1275 the Joint Global Change Research Institute (JGCRI) to explore the overall behaviour of human and physical
1276 systems dynamics and interactions. GCAM includes five main systems. One of these systems, the water module,
1277 provides information about water withdrawals for energy, agriculture, and municipal uses as lumped values of
1278 235 hydrologic basins; a detailed explanation can be found in Calvin et al. (2019). Estimates of industrial,
1279 thermoelectric water withdrawals (energy sector) and electricity consumption were computed by running the
1280 GCAM model, the output used are two files in CSV format (in total 4.0 MB). Data from the following sectors was
1281 used: "biomass", "electricity", "nuclearFuelGenII", "nuclearFuelGenIII", "regional coal", "regional natural gas",
1282 "regional oil", "SheepGoat", "Beef", "Dairy", "Pork", and "Poultry". More detail on method, data content and
1283 access can be found in the documentation of the open source package [https://github.com/JGCRI/gcam-](https://github.com/JGCRI/gcam-core/tree/gcam-v6.0)
1284 [core/tree/gcam-v6.0](https://github.com/JGCRI/gcam-core/tree/gcam-v6.0).

1285 GCAM variables were used accordingly to estimate water withdrawals for industrial, energy, livestock use.

1286
1287 **Global-scale gridded estimates of thermoelectric power and manufacturing water use** (further referred as
1288 Vassolo and Doll, 2005) is a global-scale gridded estimate of water withdrawal for cooling of thermal power
1289 stations and for manufacturing. Estimates of values for the year 1995 are provided with a spatial resolution of 0.5°
1290 by 0.5°. Thermoelectric power water use is based on the geographical location of 63590 thermal power stations.
1291 Manufacturing water use is computed by estimating country-specific water withdrawal values, and spatial
1292 downscaling using city night-time lights. Dataset verification of Vassolo and Doll (2005) showed satisfactory
1293 representation of thermoelectric power water use but high uncertainty in the representation of manufacturing water
1294 use. The data are delivered as one shapefile (2.5 MB). More details on method, data content and validation, and
1295 data access can be found in Vassolo and Doll (2005).

1296 Vassolo and Doll (2005) dataset was used for the computation of energy demand fields.

1297

1298 **The Gridded Livestock of the World (GLW) version3** (further referred as GLW3) is a spatial gridded dataset
1299 of the global distribution of eight livestock species for 2010. It is delivered as 8 GeoTiff files at 0.083333° (~10
1300 km at the equator) resolution (in total 208.0 MB). The species abundance was converted to total livestock mass.
1301 More detail on method, data content and access can be found in Gilbert et al. (2018).
1302 GLW3 was used to spatially disaggregate the water demand for livestock use.
1303

1304 **World Bank manufacturing value added and gross domestic product** (further referred as World Bank) data
1305 provide "Manufacturing, value added (constant 2015 US\$)" values (further referred as MVA) and "Gross
1306 Domestic Product GDP (constant 2015 US\$)" values. The data provided as a table, downloaded in CSV format
1307 (6 files, in total 6.0 MB) from <https://data.worldbank.org>.

1308 World Bank dataset was used to temporally downscale the values of water demand fields for the industrial and
1309 energy sectors.
1310

1311 **The Global Human Settlement Population Grid multitemporal version R2019A** (further referred as GHS-
1312 POP) is a spatial raster dataset that depicts the distribution of population, expressed as the number of people per
1313 grid cell (Freire et al., 2016; Florczyk et al., 2019; Schiavina et al., 2019). GHS-POP residential population
1314 estimates for target years provided by CIESIN GPWv4.10 were disaggregated from census or administrative units
1315 to grid cells, informed by the distribution and density of built-up as mapped in the Global Human Settlement
1316 Layer. The dataset has a spatial resolution of 9 arc sec (~300 m at the equator) resolution and is delivered as
1317 individual files in GeoTiff format for 1975, 1990, 2000 and 2015 (4 files, in total 6.5 GB; available online:
1318 https://ghsl.jrc.ec.europa.eu/ghs_pop2019.php, last accessed: 21.01.2024).

1319 GHS-POP was used to spatially disaggregate the country, state, basin-level information of domestic, industrial,
1320 energy water withdrawal.
1321

1322 **Thematic Mapping Country Borders** shapefile (further referred as TM 'country borders') was derived from
1323 Thematic Mapping™, which is a tool enabling web browsers to create thematic maps and associated world
1324 datasets. For this work, the TM World Borders Dataset was downloaded as one shapefile (10.0 MB). **The United**
1325 **States Census Bureau** Cartographic Boundary Files – Shapefile (further referred as US CB) provides the State
1326 boundaries for the USA. For this work, the 2018 version was retrieved as one shapefile (3.2 MB; available online:
1327 <https://www.census.gov/geographies/mapping-files/time-series/geo/carto-boundary-file.html>, last accessed:
1328 21.01.2024). More detail on method, data content and access can be found in
1329 <http://thematicmapping.org/downloads/>.

1330 TM 'country borders' and US CB were used to spatially disaggregate the information of water withdrawal for
1331 domestic, industrial, energy use.
1332

1333 **Multi-Source Weather** (further referred as MSWX) is a high-resolution (3-hourly, 0.1°), bias-corrected
1334 meteorological product with global coverage from 1979 to 7 months into the future. The data for 42 years
1335 (~316700 files in NetCDF format, in total 128.0 GB) were retrieved via www.gloh2o.org/mswx/. For more
1336 detailed information, see Beck et al. (2022).

1337 MSWX 2-meter daily and monthly maximum and minimum air temperature were used to account for the climate-
1338 induced intra- and inter- annual fluctuations of domestic, livestock, and energetic water demand.
1339

1340 **Huang et al. (2018)** is a publication presenting 0.5° resolution global monthly gridded sectoral water withdrawal
1341 dataset for the period 1971–2010.

1342 Huang et al. (2018) Table 3 (calibrated R coefficient values) and Eq. (2) to (6) for temporal downscaling of
1343 domestic and energy water demands were used in this study, respectively.

1344 **Appendix 2**

1345 Unit conversion to fraction

1346 Hectare (ha): $fraction = ha \cdot 10^4 / GridCellArea_{m^2}$;

1347 Percentage (%): $fraction = \% / 100$;

1348 Class (landcover type): $fraction = 1$, i.e. assumes full 100 % coverage of the grid cell.

1349 **Appendix 3**

1350 Soil depth

1351 Soil depth layers are derived following Burek et al. (2014) in which the total soil depth is horizontally divided in
1352 three layers. The total soil depth is the 'absolute_depth_to_bedrock' from SoilGrids250m, whereas root depths of

1353 forest and non-forest are derived from FAO56 and CGLS-LC100 dataset at SoilGrids250m native (~250 m)
1354 resolution (see Section 6.2 for more details). The methodology implemented for the creation of three soil layers
1355 is the following:

1356 Soil depth layer 1 (surface) SD_1 is assumed constant, equal to 50 mm all over the world for consistency with
1357 satellite-derived datasets (satellite signal penetration depth of 50 mm is a good approximation to take into account
1358 different meteorological conditions at different hour of the day globally based on Lv et al. (2018)), and follow Eq.
1359 (A1):

$$1360 \quad SD_1 = 50mm \quad (A1)$$

1361
1362 Soil depth layer 2 (middle) SD_2 depends on the absolute depth to bedrock adb – if it is equal or less than 300 mm
1363 computation follow Eq. (A2), otherwise it is conditional of the root depths as per Eq. (A3), and must meet
1364 requirement from Eq. (A4):

$$1365 \quad SD_2 = (adb - SD_1)/2, \quad adb \leq 300mm \quad (A2)$$

$$1366 \quad SD_2 = \min(\text{root_depth}, (adb - 300mm - SD_1)), \quad adb > 300m \quad (A3)$$

$$1367 \quad SD_2 = 50mm, \quad SD_2 < 50mm \quad (A4)$$

1368
1369 Soil depth layer 3 (bottom) SD_3 , is computed following Eq. (A5):

$$1370 \quad SD_3 = adb - (SD_1 + SD_2) \quad (A5)$$

1371
1372 This set of equations is used twice, once with the root depth of forest area and a second time with the root depth
1373 of non-forested areas, resulting in a total of six soil depth layers computed at SoilGrids250m native resolution.

1374 Soil hydraulic parameters

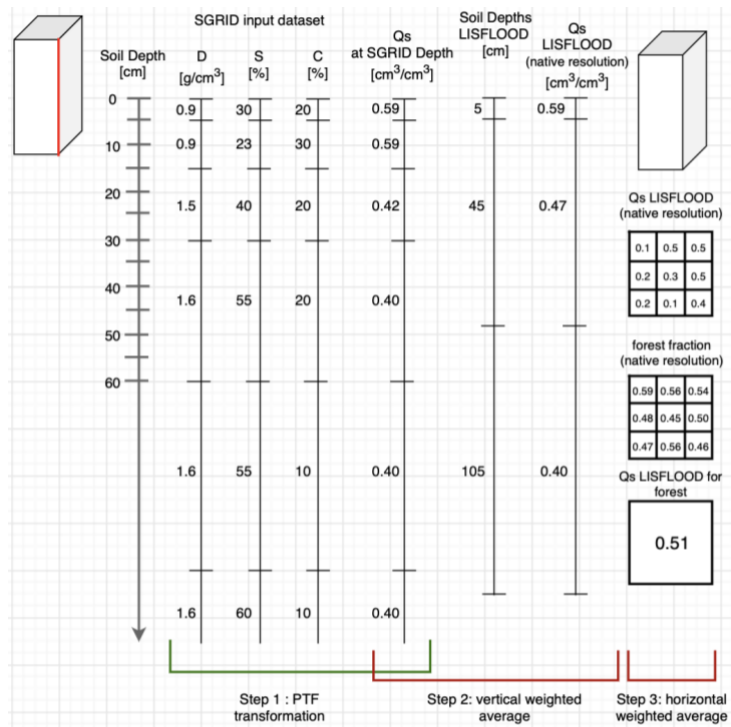
1375 Soil hydraulic parameters are derived by following three main steps (see Figure A1).

1376
1377 First, soil hydraulic properties are derived at native resolution by applying pedotransfer functions (PTFs) to each
1378 SoilGrids250m soil characteristics layer at each available depth. Pedotransfer functions translate field measured
1379 soil information (such as soil texture, pH and structure) into proprieties and parameters needed to describe soil
1380 processes. The PTFs implemented here are the ones proposed by Toth et al. (2015). Users can decide to derive
1381 soil proprieties from different PTFs, but the general principle presented here remains valid.

1382
1383 Second, the soil hydraulic parameters calculated at SoilGrids250m depths are vertically downscaled to the model
1384 soil depth (previously computed) by weighted average (Figure A1, Step 2 with theta saturated as an example) at
1385 the native SoilGrids250m resolution (~250 m).

1386
1387 Third, the soil hydraulic parameters at the final soil depths are upscaled from native to final resolution by average
1388 using forest and non-forest fraction layers as weights (Figure A1, Step 3).

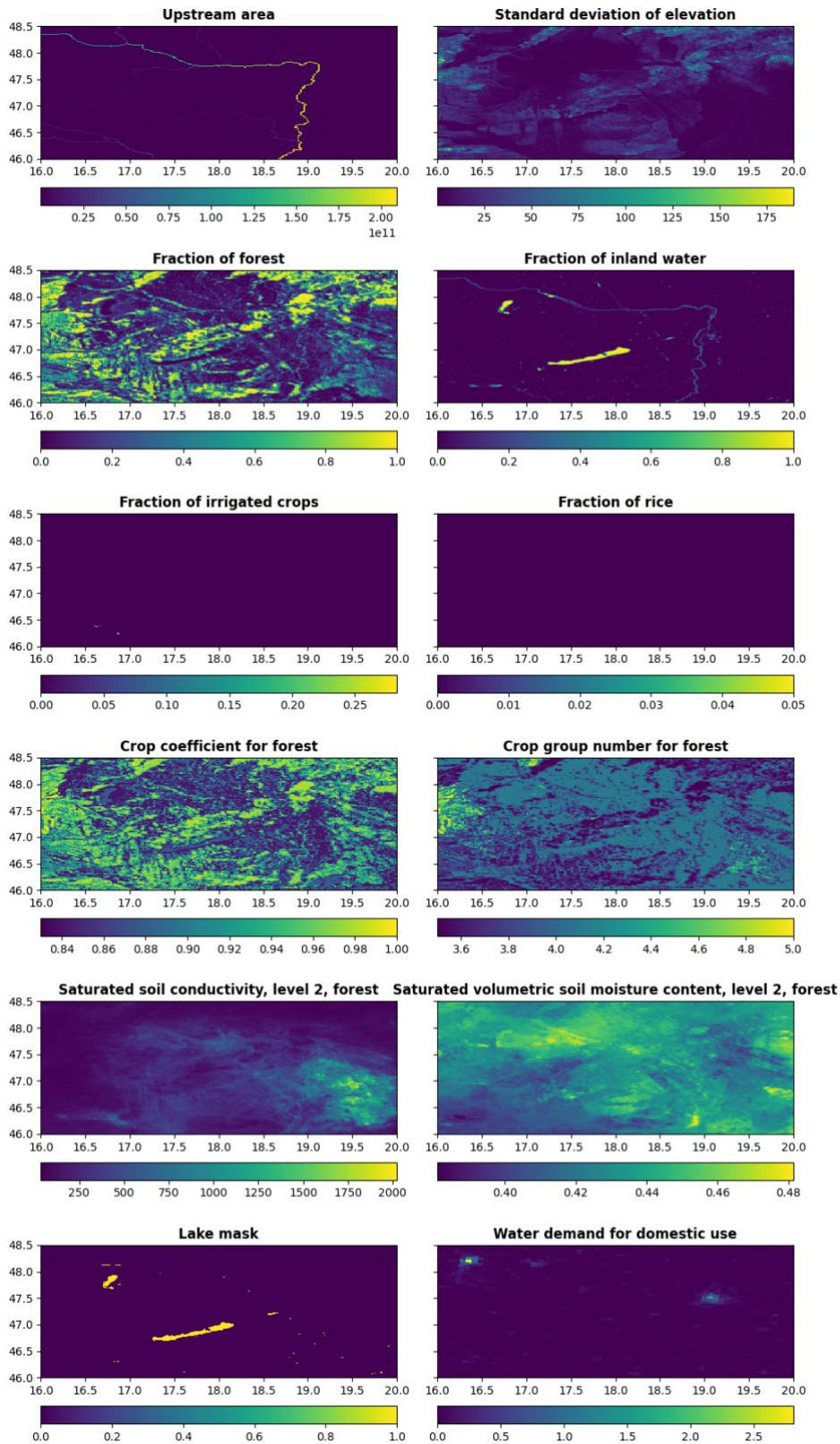
1389
1390
1391
1392



1393
1394 **Figure A1. Creation of theta saturated parameter 'Qs' using SoilGrids250m dataset 'SoilGRID' and forest**
1395 **fraction.**

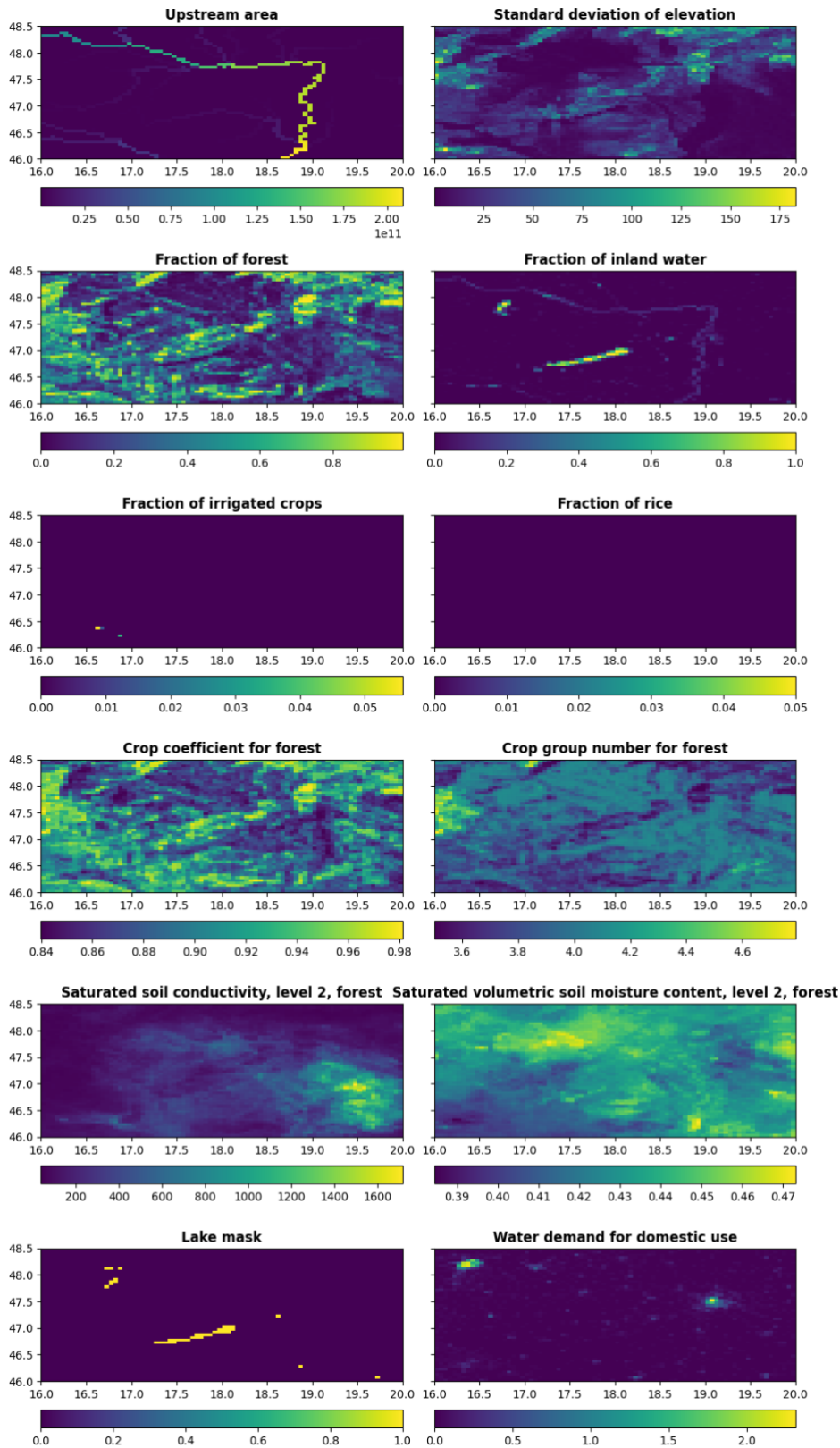
1396 **Appendix 4**

1397 Here more regional examples of the most interesting surface fields of CEMS_SurfaceFields_2022 are provided to
1398 show what level of details is available at each resolution and field, and to emphasise consistency through all the
1399 fields that is the most valuable requirement when running any type of surface model.
1400



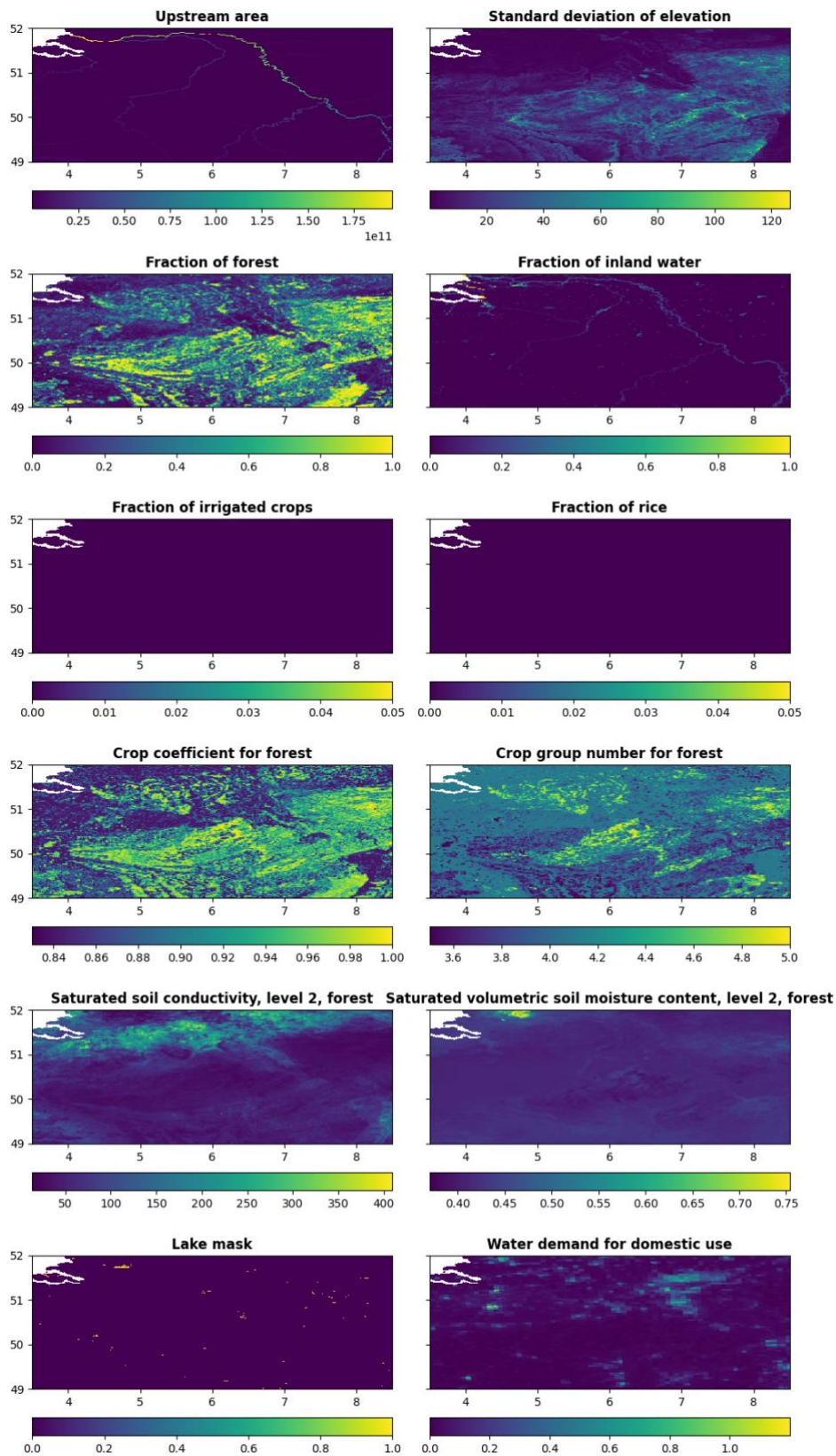
1401
 1402
 1403
 1404
 1405
 1406

Figure A2. Upstream drainage area in square meters, standard deviation of elevation in meters, fraction of forest, fraction of inland water, fraction of irrigated crops, fraction of rice, crop coefficient for forest, crop group number for forest, saturated soil hydraulic conductivity for forested areas of soil depth layer 2 in mm per day, saturated volumetric soil moisture (i.e. water) content for forested areas of soil depth layer 2, lake mask, and water demand for domestic use at 1 arc min (~1.9 km at the equator) resolution for Danube River area in Europe.



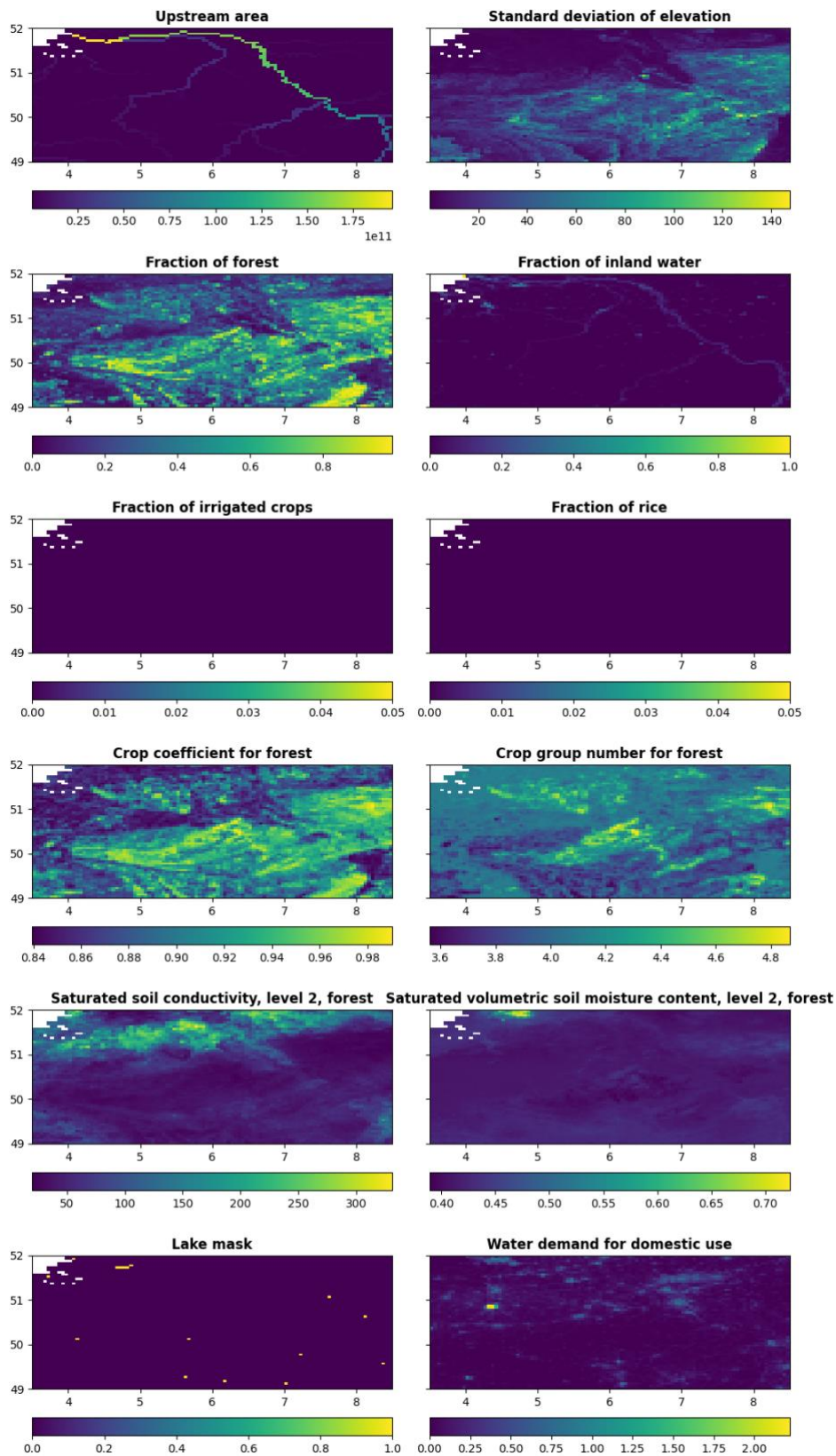
1407
1408

Figure A3. Same as Figure A2, but at 3 arc min (~5.6 km at the equator) resolution for Danube River area in Europe.



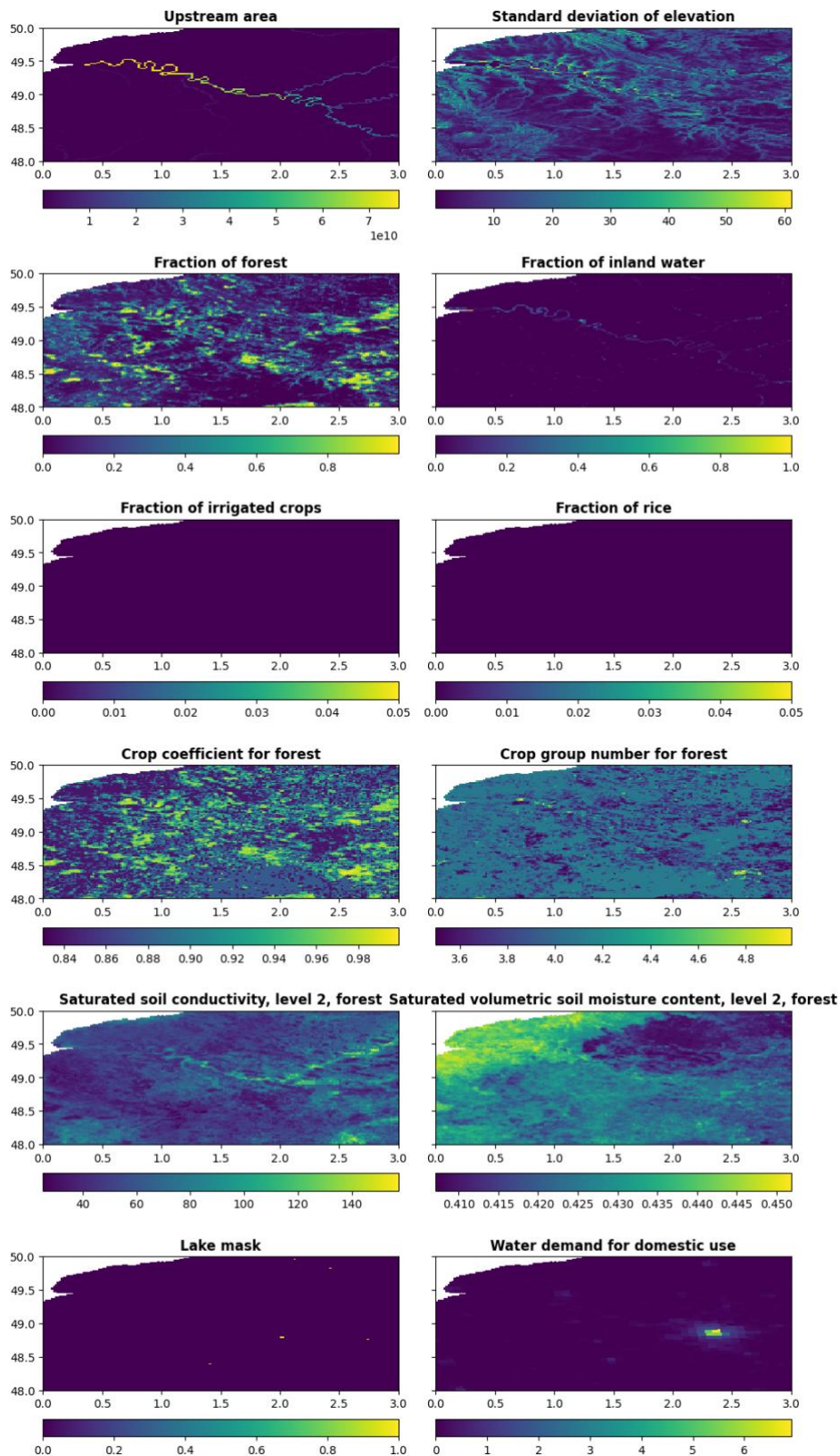
1409
1410

Figure A4. Same as Figure A2, but at 1 arc min (~1.9 km at the equator) resolution for Rhine River area in Germany.



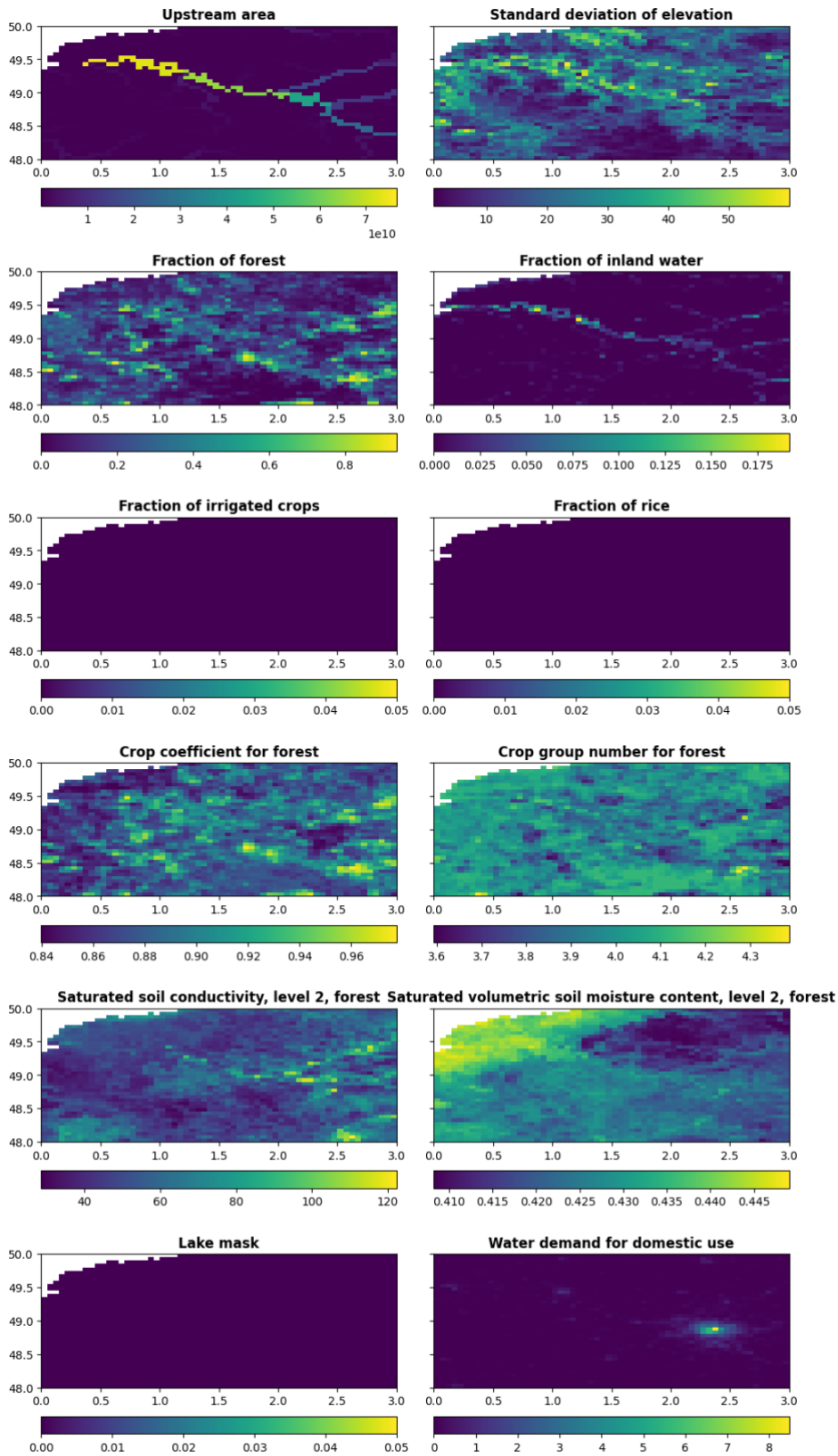
1411
1412

Figure A5. Same as Figure A2, but at 3 arc min (~5.6 km at the equator) resolution for Rhine River area in Germany.



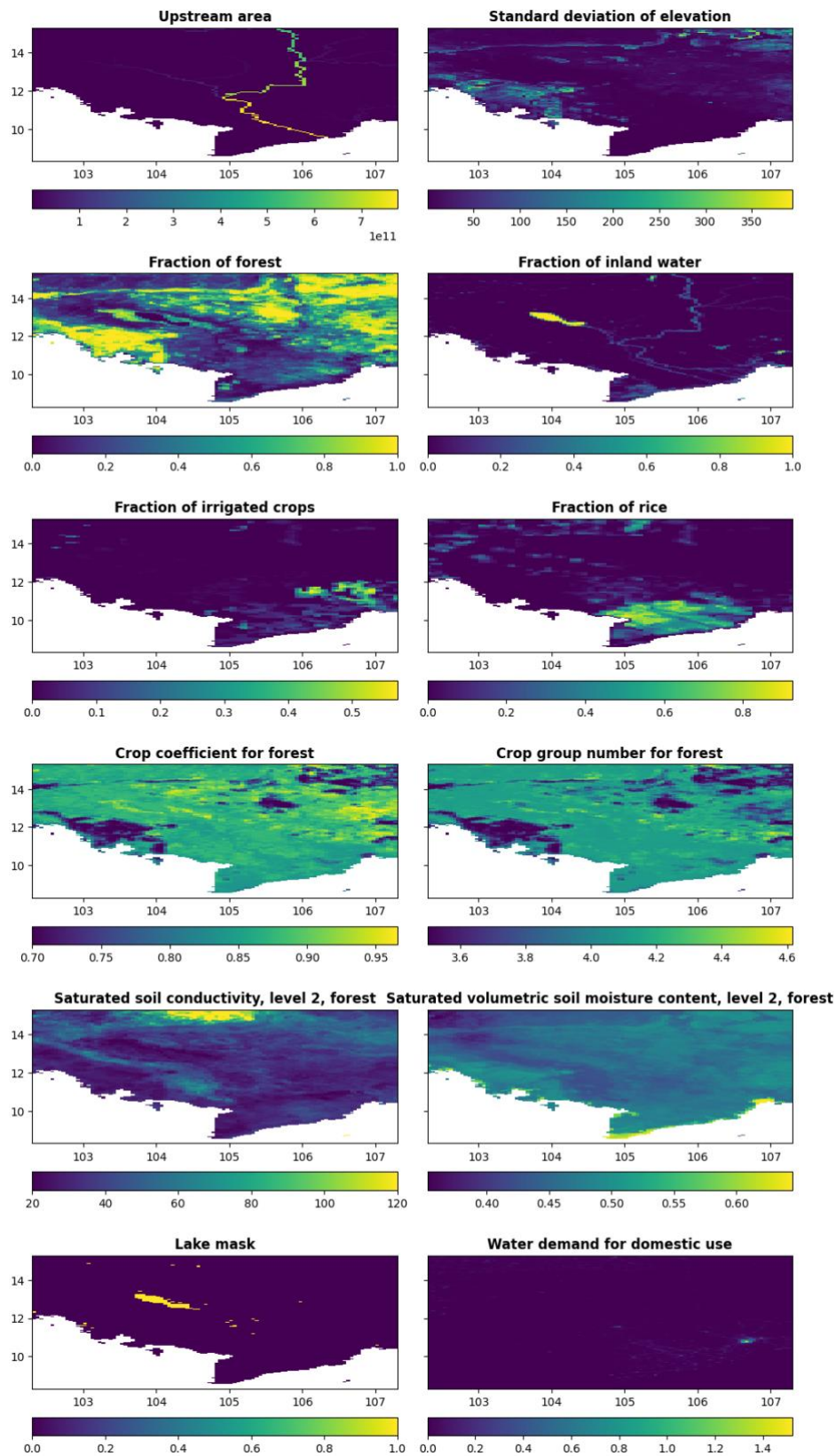
1413
1414

Figure A6. Same as Figure A2, but at 1 arc min (~1.9 km at the equator) resolution for Seine River area in France.



1415
1416

Figure A7. Same as Figure A2, but at 3 arc min (~5.6 km at the equator) resolution for Seine River area in France.



1417
1418

Figure A8. Same as Figure A2, but at 3 arc min (~5.6 km at the equator) resolution for Seine Mekong area in Cambodia.

1419
1420